A Doctoral Dissertation

A Numerical Analysis of Flow Structures around Extremely Blunt Ships

（超肥大船まわりの流場構造の数値解析）

Graduate School of Engineering
Yokohama National University

Nang Tin Tin Htwe

September, 2013

Acknowledgement

The author would like to express her sincere appreciation and gratitude to her supervisor Professor Takanori Hino (Department of Systems Design for Ocean - Space, Yokohama National University) for his infinite patient, valuable guidance, useful suggestion and encouragement throughout this research. He has given her valuable advices on her thesis work, and always kindly helps her to overcome difficulties. The author also would like to owe grateful to Professor Kazuo Suzuki for helping her during her research with valuable ideas and thoughts.

The author would like to express her sincere gratitude to the professors in Department of System Design for Ocean - Space Engineering (Prof. Takanori Hino, Prof. Kazuo Suzuki, Prof. Makoto Arai, Prof. Koji Miyaji, Prof. Yoshiaki Hirakawa, etc.) for their useful supports and suggestions in her study and research.

The author is grateful to Matsunaga Kouhei, Hashimoto Goushi and Yoda Kento for their experimental works. The author would like to thank to all her fellow research students at Hydrodynamics Laboratory for their patience, support and encouragement not only in her research and academics but also in her stay in Japan to be convenient and enjoyable. She thanks all her friends for understanding her and providing the necessary help.

The author's gratitude is also extended to the Ministry of Education, Culture and Science of Japan (Monbukagakushu) for generous financial support for her research and her stay in Japan. The author thanks the Department of Ocean and Space Engineering, Yokohama National University for their education support.

The author extends her special thanks and love to her parents, brother and sisters for inspiring within her the values of diligence and integrity. They are sources of her strength and power to complete her research.

Abstract

A novel ship concept which is called ULBS (Ultra Large Block coefficient ship) to reduce CO2 emission form sea transportation is under investigation at Yokohama National University. Since ULBS is supposed to have a very blunt hull, flow field analysis around a ship is crucial for a design of hull forms with better hydrodynamic performance. Computational Fluid Dynamics (CFD) is expected to be an efficient design tool for unconventional hull forms such as ULBS. However, it is desirable to examine applicability of the CFD method to analysis of similar flows before the actual design application. Thus, free surface flow computations of two box-shaped ships which can be considered as the extreme cases of ULBS are carried out. Grid convergence study is performed with respect to resistance for the verification of the results. Total resistance coefficients are compared with each other and also with available experimental data. The pressure and velocity distributions of the two ships are compared with each other. The flow structures with large separations are observed and the influences of the box geometry to the flow fields are discussed. This knowledge is used in the computation of ULBS.

After that to investigate the flow characteristics of ULBS (C_b>0.95), free surface viscous flows around the ship with and without a stern tunnel are computed by the solver. Total resistance coefficients are compared with each other and with experimental data. The pressure and velocity distributions of the two ships are compared with each other. Also, grid convergence study is performed with respect to resistance for the verification of the results. The velocity distributions behind the stern of the two ships are compared with each other. The three dimensional vortical structures in the stern of the two hulls are analyzed and compared with each other. Massive flow separations behind the stern due to the bluntness of a hull and effects of a stern tunnel to flow fields are discussed and this knowledge will be used on the future design of ULBS.

Table of contents

List of figures

Lists of tables

Chapter 1

Introduction

Demands for efficient sea transportation have been increasing due to globalization of world economy. At the same time, global environment protection becomes more important than ever. Therefore it is of vital importance to improve the transportation efficiency from both economic and environmental point of view. The applied ship hydrodynamics group of Yokohama National University proposes a new concept of a cargo ship called ULBS (Ultra Large Block coefficient ship) as a measure for environment-conscious sea transportation. Considering the fact that the Panama Canal will be expanded to 49 meters wide in 2014, the breadth of the ship can be expanded to increase capacity. Furthermore, the reduction of a ship speed is an effective way to decrease resistance. The ULBS concept is based on these circumstances. ULBS is a very blunt ship with wider breadth and its (L/B) length-to-breadth ratio is smaller than or equal to 5 for larger cargo capacity. The block coefficient C_b is supposed to be larger than 0.95, with a large breadth-to-length ratio ($B/L > 0.2$), which enables larger cargo capacity. On the other hand, it sails at low speed from 10 to 15 knot to recover resistance increase due to its bluntness.

Since ULBS is supposed to have a very blunt hull, flow field analysis around a ship is crucial for a hull form design with better hydrodynamic performance. However, because ordinary ship hull forms are usually designed as streamlined as possible, flow structures around extremely blunt ships have not been studied in detail. In other engineering fields such as automobile engineering, blunt bodies often attract attention. For example, the simplified car body called Armed body[1)] is widely used as a benchmark case for flows around a bluff body with massively separated wake. In case of ship flows, however, free surface interacts with turbulent separated flow around a blunt body and affects flow fields significantly. Computational Fluid Dynamics (CFD) tool is expected to be efficient in the analysis of such complicated flows. Azcueta et al.[2)] applied CFD method to free surface flow around a blunt ship and bow wave breaking was simulated. Hino[3)] also performed CFD simulations for the same blunt ship geometry. These investigations are primary focused on wave breaking at bow and side of a hull. However, flow fields around ULBS are much more complicated since the

bluntness of the hull is so extreme that flow separates in various locations. Although CFD method has become a powerful tool in ship hydrodynamics analysis, its capability for simulating flows around an unconventionally blunt body must be examined before a practical use. Therefore it is desirable to examine applicability of the CFD method to analysis of similar flows before the actual design application.

In this study, free surface flow computations on box-shaped ships which can be considered as the extreme cases of ULBS are carried out by using SURF[4], the Navier-Stokes solver developed at National Maritime Research Institute, Japan. In order to obtain insight on basic flow structure of ULBS, flows around two kinds of box shapes with different drafts are computed in the same Froude numbers. The verification of the computed resistance using three systematically refined grids is performed to assess the uncertainties of the solutions. The results of different box shapes are compared with each other and also with available experimental data.

For the practical goal of ULBS, various flow control devices such as bulbous bow (to reduce wave breaking resistance), tab type rudder (to keep course stability), stern tunnel (to reduce the flow separations behind the stern) etc. are attached to improve hydrodynamics performance.

Since ULBS has an extremely blunt hull form, it is expected that massive separations are dominant in a flow field around a hull. Therefore, understanding of flow properties is crucial for the better design of a hull form and flow control devices. Conventionally, ship hydrodynamics analysis has been carried out for a stream-lined body. Even with a blunt ship such as VLCC, a stern part is streamlined for better propulsive performance such as [2, 3] for CFD applications. However, due to the large C_b, the stern of ULBS has a shape similar to a box. In the present study, up-to-date CFD (Computational Fluid Dynamics) method is applied to the flow simulations around ULBS. Based on the experiences of the preliminary study[4] in which CFD analysis is applied to box-shaped ships, higher-order turbulence model is adopted in anticipation of accurately simulating flow separations.

As an example of flow control devices for better hydrodynamic performance, a stern tunnel is considered in the present study.

Thus, the objective of the present study is to assess up-to-date CFD with an advanced turbulence model for simulating massively separated flows around an extremely blunt ship. In addition, differences of flow structures between a bare hull and a hull with a stern tunnel are examined using numerical results together with available experimental data.

Free surface flow analyses of ULBS are carrying out by SURF, the Navier-Stokes solver developed at National Maritime Research Institute, Japan. The verification of the computed resistance using three systematically refined grids is performed in order to assess the uncertainties of the solutions. Total resistance coefficients are compared with each other and also with available experimental data. The pressure and velocity distributions of the two ships are compared with each other. Compared with the bare hull cases, the stern tunnel case can reduce the flow separations behind the stern. The flow structures with large separations are observed and this knowledge will be used to improve the future design of ULBS.

A turbulence model is essential for simulating high Reynolds number flows of practical interests. In Box-shaped Ships study, the Spalart-Allmaras model[17], one of the standard one-equation models, is adopted. It solves directly a transport equation for the eddy viscosity and it is thought to be a reasonable compromise between accuracy and complexity.

The unstructured grid based methods are one of the simplest ones and have proved very robust and reliable. In the present study, SURF v6.38 for EARSM model, is applied to demonstrate the code's performance in predicting the complex turbulent flow field with free-surface waves. The FVM method is implemented in the CFD code to handle the free-surface flow.

It is clear that in the case of Box-shaped Ship study, complex flows where separation plays a major role, a good performance of the turbulence model is essential to obtain accurate solutions. In ULBS blunt ship, an Explicit Algebraic Reynolds Stress Model has been implemented in the Reynolds-Averaged-Navier-Stokes equation solver SURF, linked with the k-omega turbulence model. After a description of the flow equations, turbulence modeling and the formulation of the EARSM, two test cases have been presented to validate the model.

The best prediction of streamwise velocity component is obtained with the EARSM model.[15]

Chapter 2

Numerical Procedure

2.1 Flow solver

The flow solver used in this study is SURF (Solution algorithm for Unstructured RaNS with FVM) which is under development at National Maritime Research institute[5), 6), 7)].The governing equations used are the three-dimensional Reynolds averaged Navier-Stokes equations for incompressible flows. In order to couple pressure with a velocity field, artificial compressibility is introduced into the continuity equation. In order to account for the unsteadiness, the dual time stepping is employed in which t is the physical time and t^* is the pseudo time for artificial compressibility and the sub-iteration with t^* is performed at each time step t.

The final form is written as follows:

$$\frac{\partial q^*}{\partial t}+\frac{\partial q}{\partial t^*}+\frac{\partial (e-e^v)}{\partial x}+\frac{\partial (f-f^v)}{\partial y}+\frac{\partial (g-g^v)}{\partial z}=0 \tag{2.1}$$

where,

$$q=\begin{bmatrix} p & u & v & w \end{bmatrix}^T \tag{2.2}$$

$$q^*=\begin{bmatrix} 0 & u & v & w \end{bmatrix}^T \tag{2.3}$$

In the above expressions all the variables are made dimensionless using the reference density ρ, velocity U and length L_{pp}. In case of free surface flows, pressure p is modified as

$$p=p^*+\frac{z}{Fr^2}$$

where p^* is the original pressure and F_r is the Froude number, $U/\sqrt{gL_{pp}}$,with z being the vertical coordinate. The velocity components in the (x, y, z) direction is expressed as (u, v, w).

The inviscid fluxes e, f and g are defined as

$$\boldsymbol{e} = \begin{bmatrix} \beta u \\ u^2 + p \\ uv \\ uw \end{bmatrix}, \boldsymbol{f} = \begin{bmatrix} \beta v \\ vu \\ v^2 + p \\ vw \end{bmatrix}, \boldsymbol{g} = \begin{bmatrix} \beta w \\ wu \\ wv \\ w^2 + p \end{bmatrix} \tag{2.4}$$

where β is a parameter for artificial compressibility. The viscous flux e^v, f^v, and $g^v$are written as:

$$\boldsymbol{e}^v = \begin{bmatrix} 0 \\ \tau_{xx} \\ \tau_{xy} \\ \tau_{zx} \end{bmatrix}, \boldsymbol{f}^v = \begin{bmatrix} 0 \\ \tau_{xy} \\ \tau_{yy} \\ \tau_{yz} \end{bmatrix}, \boldsymbol{g}^v = \begin{bmatrix} 0 \\ \tau_{zx} \\ \tau_{yz} \\ \tau_{zz} \end{bmatrix} \tag{2.5}$$

$$\tau_{ij} = (\frac{1}{Re} + \nu_t)(\frac{\partial u_i}{\partial x_j} + \frac{\partial u_j}{\partial x_i}) \tag{2.6}$$

Re is the Reynolds number, and defined as UL_{pp}/ν, where ν is the kinematic viscosity. ν_t is the non-dimensional kinematic eddy viscosity determined by an appropriate turbulence model which is determined by the Spalart-Allmaras one equation model[17)] .

$$\tau_{ij} = \frac{1}{Re}(\frac{\partial u_i}{\partial x_j} + \frac{\partial u_j}{\partial x_i}) + \tilde{\tau}_{ij} \tag{2.7}$$

Re is the Reynolds number, and defined as UL_{pp}/ν, where ν is the kinematic viscosity. $\breve{\tau}_{ij}$ is the Reynolds-stress anisotropy tensor determined by an appropriate turbulence model which is determined by the Explicit Algebraic Reynolds Stress Model (EARSM) model [9)].

For the inviscid fluxes (convection terms and pressure gradient terms), the second order upwind scheme based on the flux-differencing splitting of Roe [8)] with the MUSCL approach is employed. The viscous fluxes are evaluated by the second order central scheme. Thus, the overall accuracy in space is the second order.

2.2 Spatial Discretization

Spatial discretization is based on a cell centered finite volume method for an unstructured grid. The cell shapes are tetrahedral, prism, pyramid or hexahedral and face shapes are either triangular or quadrilateral as shown in Figure 2.1 [5), 16)]. It says these four types of cells give larger flexibility in handling complex geometries.

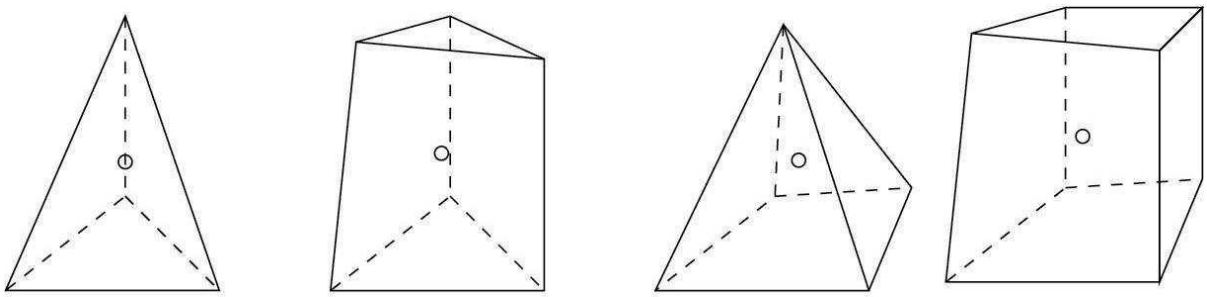

(a) Tetrahedral (b) Prism (c) Pyramid (d) Hexahedral

Figure 2.1 Cell shapes

In particular, it is suitable for a hybrid grid approach in which prisms and hexahedra are placed in the region close to a solid wall for the efficient resolution of boundary layers while tetrahedron and pyramids are used to tessellate the remaining region in a flexible manner. A cell centered layout is adopted which means flow variables q are defined at the centroid of each cell and a control volume is a cell by itself.

Volume integration of equation (2.8) over a cell yields [5)].

$$\iiint_{v_i} \left(\frac{\partial q}{\partial t} + \frac{\partial (e - e^v)}{\partial x} + \frac{\partial (f - f^v)}{\partial y} + \frac{\partial (g - g^v)}{\partial z} \right) dV = 0 \tag{2.8}$$

Since the grid in the application is stationary, the first term in the integral is the time derivative of the product of the cell volume V_i and the cell averaged value of flow variables q_i .The remaining terms are converted into surface integration over cell faces using the divergence theorem. This yields semi-discrete form of the governing equation as follows,

$$\frac{\delta(V_i q_i)}{\delta t} + \sum_j F_{i+j/2} - \sum_j R_{i+j/2} = 0 \tag{2.9}$$

where i is a cell index and j is the index of neighboring cells of the cell i. $(i+j)/2$ is the face between cells i and j as shown in Figure 2.2. Equation (2.8) is solved using 2nd order upwind scheme based on flux difference splitting in space and Euler implicit scheme in time[5].

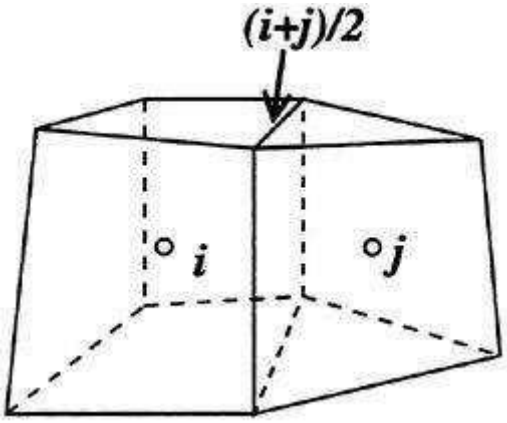

Figure 2.2 Definition sketch of cell and face indices.

$\boldsymbol{F}$ and $\boldsymbol{R}$ are the inviscid and viscous fluxes defined as

$$\boldsymbol{F} = \boldsymbol{e}S_x + \boldsymbol{f}S_y + \boldsymbol{g}S_z \ , \ \boldsymbol{R} = \boldsymbol{e}^v S_x + \boldsymbol{f}^v S_y + \boldsymbol{g}^v S_z$$

(S_x, S_y, S_z) are the (x, y, z)-components of the area vector of a cell face in the direction from the cell i to the cell j.

Components of the inviscid fluxes $\boldsymbol{F}$ are

$$\boldsymbol{F(q)} = \begin{bmatrix} \beta U \\ uU + pS_x \\ vU + pS_y \\ wU + pS_z \end{bmatrix} \tag{2.9}$$

where $U = uS_x + vS_y + wS_z$ .Based on the flux-difference splitting, the inviscid flux are evaluated by the upwind scheme.

$$\boldsymbol{F}_{(i+j)/2} = \frac{1}{2}[\boldsymbol{F}(\boldsymbol{q}^{\boldsymbol{R}}) + \boldsymbol{F}(\boldsymbol{q}^{\boldsymbol{L}}) - |\boldsymbol{A}|.(\boldsymbol{q}^{\boldsymbol{R}} - \boldsymbol{q}^{\boldsymbol{L}})] \tag{2.10}$$

Where $\boldsymbol{q}^{\boldsymbol{R}}$ and $\boldsymbol{q}^{\boldsymbol{L}}$ are the flow variables on the right side and the left side of a cell face, respectively. $|\boldsymbol{A}|$ is defined in the following way. Let $\boldsymbol{A}$ be the Jacobian of the inviscid flux $\boldsymbol{F}$ at a cell face:

$$\boldsymbol{A} = \frac{\partial \boldsymbol{F}((\boldsymbol{q}^R + \boldsymbol{q}^L)/2)}{\partial \boldsymbol{q}} \tag{2.11}$$

The eigenvalues of $\boldsymbol{A}$ are *U*, *U*, *U*+*c*, *U*-*c* where c is the pseudo-speed-of-sound defined as

$$c = \sqrt{U^2 + \beta(S_x^2 + S_y^2 + S_z^2)} \tag{2.12}$$

By using the right-eigenvector $\boldsymbol{R}$, $\boldsymbol{A}$ can be expressed as $\boldsymbol{A} = \boldsymbol{R}\boldsymbol{\Lambda}R^{-1}$,

$$\Lambda = diag(U, U, U + c, U - c).$$

$$|\boldsymbol{A}| = \boldsymbol{R}|\boldsymbol{\Lambda}|\boldsymbol{R}^{-1}, \text{ and } |\boldsymbol{\Lambda}| = diag(|U|, |U|, |U + c|, |U - c|).$$

To maintain the second order accuracy in space, $\boldsymbol{q}^R$ and $\boldsymbol{q}^L$ are extrapolated using the Taylor expansion as follows:

$$\boldsymbol{q}^L = \boldsymbol{q}_i + \nabla \boldsymbol{q}_i.(\boldsymbol{x}_{(i+j)/2} - \boldsymbol{x}_i)$$

$$\boldsymbol{q}^R = \boldsymbol{q}_j + \nabla \boldsymbol{q}_j.(\boldsymbol{x}_{i+j/2} - \boldsymbol{x}_j)$$

where $\boldsymbol{x}_{(i+j)/2}$ is the coordinate of the center of face $(i+j)/2$ and x_i and x_j are the coordinates of the centroid of cell i and j, respectively. ∇q_i is the gradient of q at the cell centroid *i* and this can be computed by applying the divergence theorem to the cell *i* with the values of *q* at the cell *i* and its neighbors *j*.

Viscous fluxes components are written as

$$\boldsymbol{R}(\boldsymbol{q}) = \begin{bmatrix} 0 \\ S_x\tau_{xx} + S_y\tau_{xy} + S_z\tau_{zx} \\ S_x\tau_{xy} + S_y\tau_{yy} + S_z\tau_{yz} \\ S_x\tau_{zx} + S_y\tau_{yz} + S_z\tau_{zz} \end{bmatrix} \tag{2.13}$$

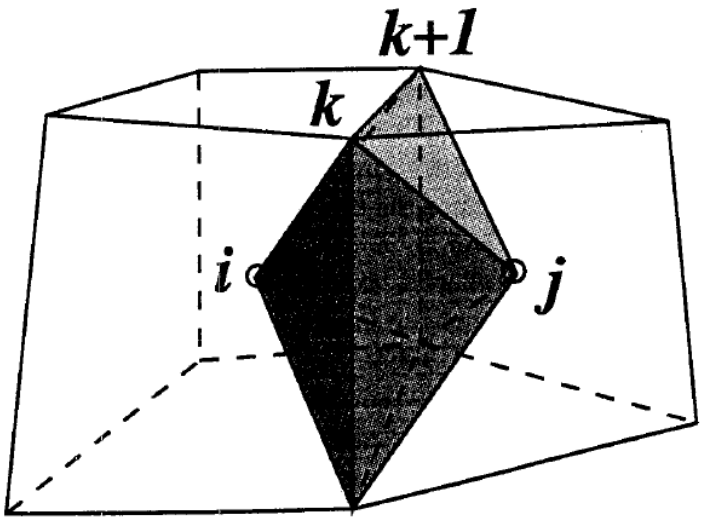

Figure 2.3 Control volume for the evaluation of velocity gradient.

The computation of $\boldsymbol{R}_{(i+j)/2}$ requires velocity gradient on a cell face. These are computed by applying the divergence theorem to another control volume surrounding a cell face as shown in Fig. 2. The values of q at the centroid i and j and at the nodes k, $k+1$… surrounding the face $(i+j)/2$ are used for the surface integration. $\partial u/\partial x$ is computed as

$$\frac{\partial u}{\partial x_{(i+j)/2}} = \frac{1}{V^*} \sum_{Faces} uS_x$$

$$= \frac{1}{V^*}\left(\frac{u_i + u_k + u_{k+1}}{3} S_{x,i,k,k+1} + \frac{u_j + u_k + u_{k+1}}{3} S_{x,j,k,k+1} + \ldots\right) \tag{2.14}$$

where V^* is the volume of the current control volume and $S_{x,\alpha,\beta,\gamma}$ is the x- component of the outward area vector of the face formed by the nodes α, β and γ.

The velocity values at the nodes *k*, *k*+1 etc. are computed from the values at the centroids by simple averaging.

2.3 Time integration

The backward Euler scheme is used for the time integration. The governing equation is

$$V_i \frac{\Delta \boldsymbol{q}_i}{\Delta t} + \sum_j \boldsymbol{F}_{(i+j)/2}^{n+1} - \sum_j \boldsymbol{R}_{(i+j)/2}^{n+1} = 0 \tag{2.15}$$

Where

$$\Delta \boldsymbol{q} = \boldsymbol{q}^{n+1} - \boldsymbol{q}^n$$

And the superscripts denote the time step. Δt is time increment for local time stepping in which Δt is determined cell by cell in such a way that the *CFL* number is globally constant. The linearization of the inviscid flux F^{n+1} with respect to time is

$$\boldsymbol{F}^{n+1} = \boldsymbol{F}^n + \frac{\partial \boldsymbol{F}}{\partial \boldsymbol{q}} . \Delta \boldsymbol{q} \tag{2.16}$$

When the Jacobian $\partial \boldsymbol{F} / \partial \boldsymbol{q}$ is evaluated, the flux *F* is computed with the first order accuracy by setting

$$\boldsymbol{q}^L = \boldsymbol{q}_i, \ \boldsymbol{q}^R = \boldsymbol{q}_j$$

Thus, the inviscid flux is written as

$$\boldsymbol{F}_{(i+j)/2}^{n+1} = \boldsymbol{F}_{(i+j)/2}^{n} + \frac{1}{2} \left\{ \boldsymbol{A}_j . \Delta \boldsymbol{q}_i + \boldsymbol{A}_i . \Delta \boldsymbol{q}_i - |\boldsymbol{A}| . (\Delta \boldsymbol{q}_j - \Delta \boldsymbol{q}_i) \right\}$$

where

$$\boldsymbol{A}_i = \frac{\partial \boldsymbol{F}(\boldsymbol{q}_i)}{\partial \boldsymbol{q}_i}$$

In the similar manner the viscous flux is linearized in time as

$$\boldsymbol{R}^{n+1} = \boldsymbol{R}^{n} + \frac{\partial \boldsymbol{R}}{\partial \boldsymbol{q}}.\Delta \boldsymbol{q} \tag{2.18}$$

For the evaluation of the Jacobian $\partial \boldsymbol{R}/\partial \boldsymbol{q}$, $\boldsymbol{R}$ is approximated by neglecting the contribution from the values at the nodes, i.e. $\boldsymbol{q}_k$, $\boldsymbol{q}_{k+1}$. Thus, $\boldsymbol{R}$ becomes dependent only on the values on the cell centroid, $\boldsymbol{q}_i$ and $\boldsymbol{q}_j$ and $\partial \boldsymbol{R} / \partial \boldsymbol{q}.\Delta \boldsymbol{q}$ becomes

$$\partial \boldsymbol{R} / \partial \boldsymbol{q}.\Delta \boldsymbol{q} \approx \boldsymbol{B}.(\Delta \boldsymbol{q}_j - \Delta \boldsymbol{q}_i).$$

$$\boldsymbol{B} = (\frac{1}{R} + \nu_t)\frac{1}{3V^*} \times \begin{bmatrix} 0 & 0 & 0 & 0 \\ 0 & |S|^2 + S_x^2 & S_x S_y & S_x S_z \\ 0 & S_x S_y & |S|^2 + S_y^2 & S_y S_z \\ 0 & S_x S_z & S_y S_z & |S|^2 + S_z^2 \end{bmatrix}$$

with

$$|S|^2 = S_x^2 + S_y^2 + S_z^2$$

Eq. (2.15) now becomes

$$\begin{aligned} &\boldsymbol{V}_i \frac{\Delta \boldsymbol{q}_i}{\Delta t} + \sum_j \boldsymbol{F}_{(i+j)/2}^{n+1} - \sum_j \boldsymbol{R}_{(i+j)/2}^{n+1} + \sum_j \frac{1}{2}\{\boldsymbol{A}_j.\Delta \boldsymbol{q}_j + \boldsymbol{A}_i.\Delta \boldsymbol{q}_i - |\boldsymbol{A}|.(\Delta \boldsymbol{q}_j - \Delta \boldsymbol{q}_i)\} - \\ &\sum_j \boldsymbol{B}.(\Delta \boldsymbol{q}_j - \Delta \boldsymbol{q}_i) = 0 \end{aligned} \tag{2.16}$$

The delta terms are rearranged into the form as follows.

$$\left\{\frac{V_i}{\Delta t}\boldsymbol{I} + \sum_j (\frac{\boldsymbol{A}_i + |\boldsymbol{A}|}{2} + \boldsymbol{B})\right\}.\Delta \boldsymbol{q}_i + \sum_j \left\{(\frac{\boldsymbol{A}_i + |\boldsymbol{A}|}{2} + \boldsymbol{B}).\Delta \boldsymbol{q}_i\right\} + \sum_j \boldsymbol{F}_{(i+j)/2}^{n} - \sum_j \boldsymbol{R}_{(i+j)/2}^{n} = 0 \tag{2.17}$$

Equation (2.17) is a linear equation with respect to Δq. The symmetric Gauss-Seidal (SGS) is adopted to solve this equation. To achieve fast convergence, the cells are ordered from upstream to downstream. The first Gauss-Seidal sweep is carried from the upstream cell to the downstream. Then the second sweep follows the reverse order. Typically 20 SGS sweeps are performed at each time step.

2.4 Free surface Treatment

Free surface in this study is an interface between air and water. Free surface conditions consist of dynamics and kinematics conditions and they are implemented in the interface capturing framework. The condition that fluid particles on a free surface remain on an interface is the kinematic condition. It is written in a mathematical form as follows [16]:

$$\frac{DH}{Dt} = \frac{\partial H}{\partial t} + u\frac{\partial H}{\partial x} + v\frac{\partial H}{\partial y} + w\frac{\partial H}{\partial z} = 0 \tag{2.18}$$

Where a free surface shape is defined as

$$H(x, y, z; t) = 0$$

The kinematic condition in the present scheme is formulated based on the level set method which improves the efficiency of the original level set approach [11] used in the previous version of the present code [10]. The level set function ϕ is defined as the signed distance from the interface, i.e..,

$$\phi \begin{cases} > 0 & \text{in} \quad \text{water} \\ = 0 & \text{on} \quad \text{the} \quad \text{interface} \\ < 0 & \text{in} \quad \text{air} \end{cases} \tag{2.19}$$

Since ϕ (x, y, z; t) = 0 defines the free surface shape, the kinematic condition can be satisfied if the following equation is used to update ϕ:

$$\frac{D\phi}{Dt} = \frac{\partial \phi}{\partial t} + u\frac{\partial \phi}{\partial x} + v\frac{\partial \phi}{\partial y} + w\frac{\partial \phi}{\partial z} = 0 \tag{2.20}$$

The numerical solution method for equation (2.20) is identical to the flow equations. The cell centered finite-volume discretization applied for the cell i yields

$$V_i \frac{\partial \phi_i}{\partial t} + \sum_j \left(\phi_{(i+j)/2} U_{(i+j)/2}\right) = 0 \tag{2.21}$$

where

$$U_{(i+j)/2} = u_i S_{x,(i+j)2} + v_i S_{y,(i+j)2} + w_i S_{z,(i+j)2}$$

V_i is the cell volume and j is the neighbor cells of the cell i. The subscript $(i+j)/2$ means the cell face between the cells i and j and (S_x, S_y, S_z) are the area of cell faces. $\phi_{(i+j)/2}$, the value of ϕ on the cell face, is extrapolated from the cell centered values in the second order upwind manner. The extrapolation is obtained by the least square method. The time integration is carried by the Euler backward scheme.

Suppose that the interface is undisturbed on z=0 and the flow field is uniform and $(u,v,w)=(1,0,0)$. The initial value of ϕ is $\phi = -z$. This is a steady state solution of the analytical equation (2.20). The discrete equation (2.21), does not give $\partial\phi/\partial t = 0$, unless

$$\sum_j \left(\phi_{(i+j)/2} S_{x,(i+j)/2}\right) = 0 \tag{2.22}$$

is satisfied. Since $\phi = -z$ is a linearly varying function, the extrapolation of the face value $\phi_{(i+j)/2}$ from the cell centered values can be performed by the second order scheme. However, the one point quadrature $\phi_{(i+j)/2}\ S_{x,(i+j)/2}$ have significant amount of error, the higher order quadrature will increase the computational cost considerably. To remedy this problem, a new variable $\tilde{\phi}$ is introduced,

$$\tilde{\phi} = \phi + z \tag{2.23}$$

To solve $\tilde{\phi}$ instead of ϕ, equation (2.20) is modified as

$$\frac{\partial\tilde{\phi}}{\partial t} + u\frac{\partial\tilde{\phi}}{\partial x} + v\frac{\partial\tilde{\phi}}{\partial y} + w\frac{\partial\tilde{\phi}}{\partial z} - w = 0 \tag{2.24}$$

and in the discrete form

$$V_i \frac{\partial\tilde{\phi}_i}{\partial t} + \sum_j \left(\tilde{\phi}_{(i+j)/2} U_{(i+j)/2}\right) - V_i w_i = 0 \tag{2.25}$$

For the initial field of $\tilde{\phi} = -z$ and $(u,v,w)=(1,0,0)$, $\partial\tilde{\phi}/\partial t = 0$ because $\tilde{\phi} = 0$ everywhere and the fluxes are evaluated as zero, regardless of the quadrature.

In order to avoid reflection of free surface waves in the outer boundaries of a computational domain, the wave damping method is applied to the level set method. The damping term which makes $\tilde{\phi}$ approach zero are added to the level set equation (2.25) as follows:

$$V_i \frac{\partial \tilde{\phi}_i}{\partial t} + \sum_j \left(\tilde{\phi}_{(i+j)/2} U_{(i+j)/2} \right) - V_i w_i + V_i W \tilde{\phi}_i = 0 \qquad (2.26)$$

$W(x,y,z)$ is weight function defined as

$$W(x,y,z) = A \times max\left(W_x(x), W_y(y)\right)$$

$$W_x(x) = \begin{cases} \left(\dfrac{x - x_d}{x_0 - x_d} \right)^2 & \text{if} \quad x_d \le x \le x_0 \\ o & \text{otherwise} \end{cases}$$

$$W_y(y) = \begin{cases} \left(\dfrac{y - y_d}{y_0 - y_d} \right)^2 & \text{if} \quad y_d \le y \le y_0 \\ o & \text{otherwise} \end{cases}$$

where x_d, y_d are the coordinate from which damping region starts and x_0, y_0 are the location of outflow and boundaries. The parameter *A* controls the amount of damping.

There is a singular behavior of the interface in the region close to a solid wall. The no-slip condition imposed on a wall prevents the interface movement there, while the interface in the outer region moves following the fluid motion. It causes the large deformation of ϕ near a solid wall. The value of ϕ for the cells close to the wall is extrapolated from the outer cell to remove this singularity.

It is easy to find the outer cell for the particular cell in the structured grid. But it is not a trivial task in the unstructured grid case. First, the closest wall d_i is computed and stored for each cell. To choose the outer cell, compare the quantity d_j / r_{ij} instead of d_j, where r_{ij} is the distance between the cell centers *i* and *j*. In Figure 2.4, since r_{AB} is smaller than r_{AC}, the cell *B* is chosen as an outer cell.

In the original level set approach, the re-initialization of the level set function is performed at every time stage to assure that the level set function is the signed distance function. The re-initialization is not required application because the free surface configurations are rather moderate in these applications.

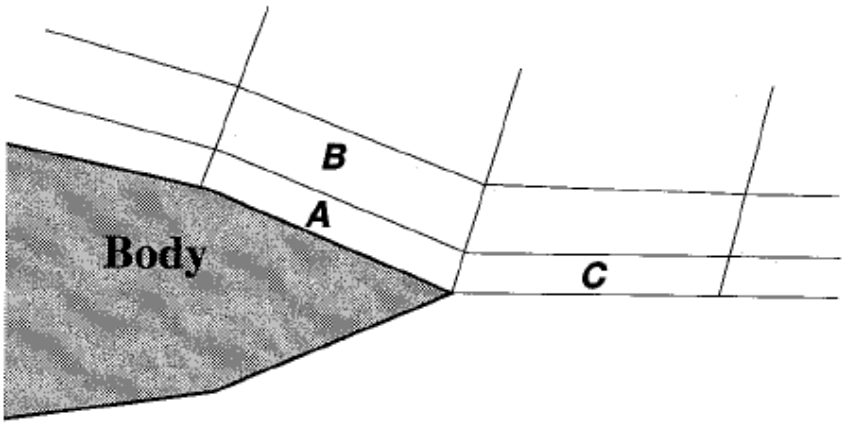

Figure 2. 4 Selection of an outer cell.

Since most of ship hydrodynamics applications require a flow field of water region only, the air region does not need to be solved.

The dynamic free surface conditions are approximated by the following two conditions. First, the velocity gradients normal to the free surface are zero. Second, the pressure on the free surface is equal to atmospheric pressure. For the first condition, the velocity components are extrapolated in the direction normal to the interface. Firstly air cells (the value of ϕ is negative), the search for the neighboring cells (the values of ϕ is positive) is carried out. If only one water cell is found, this water cell is selected a source cell. If several water cells are found, a source cell is defined in the following way. The current air cell whose velocity should be extrapolated is denoted as *i* and a candidate water cell is denoted as *j*. Let the vector e_{ji} be the unit vector from the cell center *j* to the cell center *i* and $\nabla\phi_j$ be the gradient of ϕ at the cell center *j*. $e_{ji}.\nabla\phi/|\nabla\phi|$ is unity when the vector e_{ji} and the interface normal are parallel and zero when the vector e_{ji} is perpendicular to the interface normal. Thus, the cell with the largest value of $e_{ji}.\nabla\phi/|\nabla\phi|$ selected as a source cell. In case of the air cells whose all neighbors are air cells, velocity is extrapolated from the air cells

whose velocity are already extrapolated. The selection of a source cell in this case can be performed in a similar way. After the extrapolation of network is established, velocity components of the air cell are set equal to those of the corresponding source cell.

The pressure boundary condition is written as

$p = \frac{h}{F^2}$ on the free surface

where atmospheric pressure is assumed to be zero and *h* is the *z*-coordinate of the interface. The pressure extrapolation formula can be constructed as follows. Suppose that the cell *i* is the air cell for which the pressure must be extrapolated and the cell *j* is the corresponding source.

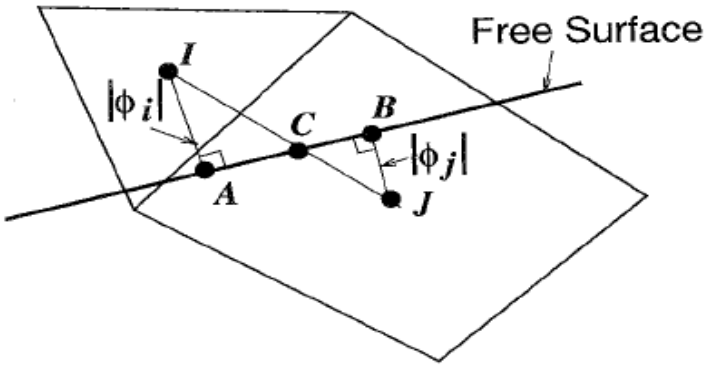

Figure 2.5 Pressure Extrapolation.

Since the level set function ϕ is the signed distance function, $|\phi|$ is the distance to the interface with $\phi_i < 0$ and $\phi_j > 0$. The interface is located between the cell centers i and j. As shown in Fig. 2, the interface is locally approximated by a flat plate and the closet point on the interface from the cell center *i* is denoted as *A* and the closet point on the interface from the cell center *i* is denoted as *B*. Also the intersection of the interface and the line connecting the cell centers *i* and *j* is denoted as C. Since the triangle *IAC* is similar to the triangle *JBC* and $IA = |\phi_i|$ and $IB = |\phi_j|$. The $Z_{c,z}$-coordinate of the point C, is given by

$$Z_c = \frac{|\phi_i| Z_j + |\phi_j| Z_i}{|\phi_i| + |\phi_j|}$$

Thus pressure is extrapolated as

$$p_i = \frac{\left(Z/F^2\right)\left(|\phi_i| + |\phi_j|\right) - p_j|\phi_i|}{|\phi_j|} \tag{2.27}$$

in such a way that

$$p_c = \frac{Z_c}{F^2}$$

This procedure uses only the value of ϕ and the actual free surface shape does not need to be constructed.

In case of the air cells whose all neighbors are air cells, pressure is set equal to that of a source cell.

Figure 2.6 shows an example of the extrapolation network taken from the actual computation. The dotted lines are cells and the thick solid line shows the interface, i.e., the line of $\phi = 0$. The arrows depict the direction of flow variable extrapolation. It is seen that the direction of flow extrapolation is close to the interface normal.

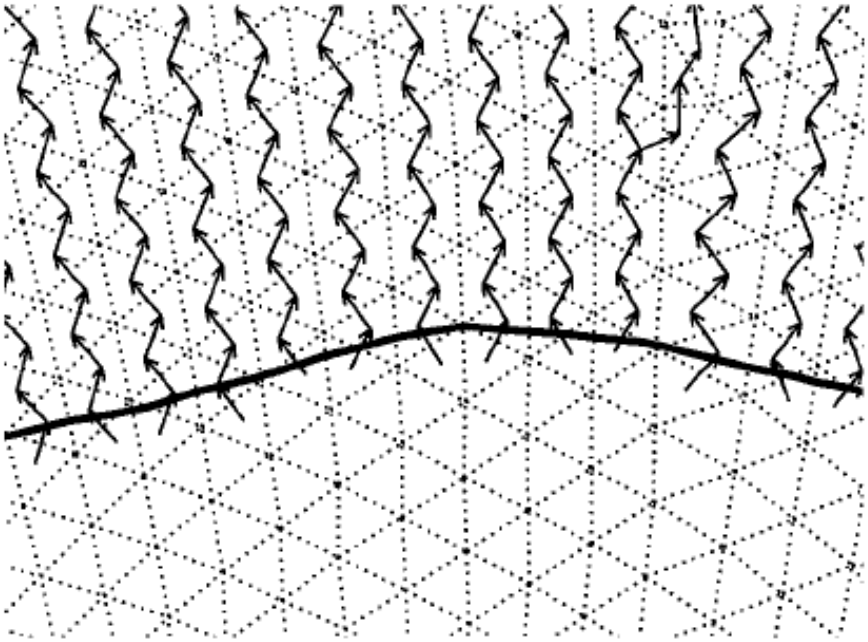

Figure 2.6 Extrapolation network.

2.5 Multigrid

A multigrid method is known as the extremely efficient way to get fast convergence. The concept of a multigrid time stepping applied to the solution of hyperbolic equations is to compute corrections to the solution on a fine grid by the time-stepping on a coarser grid. This is called a geometric multigrid and successively coarser grids should be generated geometrically from an original grid.

The procedure of the multigrid method is as follows. Equations to be solved is written as

$$\frac{dq}{dt} = -R(q) \tag{2.28}$$

and the subscript k denotes the grid index.

First, the solution q_k is obtained in the fine grid $(k)$by solving

$$\frac{dq_k}{dt} = -R_k(q_k) \tag{2.29}$$

by the numerical scheme described above, i.e., the Euler-backward scheme and the Gauss-Seidel iteration. The solution is transferred from the fine grid (k) to the next coarser grid $(k+1)$by

$$q_{k+1}^{(0)} = T_k^{k+1} q_k \tag{2.30}$$

where $T_k^{k+1}$is a transfer (restriction) operator for a solution defined as

$$T_k^{k+1} q_k = (\Sigma q_k V_k)/V_{k+1} \tag{2.31}$$

where the sum is over cells to be fused to a coarser grid cell and V is a cell volume. The solution in the coarse grid is updated by solving the equation

$$\frac{dq_{k+1}}{dt} = -R_{k+1}(q_{k+1}) - P_{k+1} \tag{2.32}$$

with the same manner except that the spatial operator R_{k+1} adopts the first order scheme and q_{k+1}^{+} is obtained. P in the above equation is called the forcing terms in the coarse grid $(k+1)$ defined as

$$P_{k+1} = Q_k^{k+1} R_k(q_k) - R_{k+1}\left(q_{k+1}^{(0)}\right) \tag{2.33}$$

where Q_k^{k+1} is another transfer operator for a residual and is the sum of the residuals of cells to be merged into a coarser grid cell, i.e.,

$$Q_k^{k+1} R_k(q_k) = \Sigma(R_k) \tag{2.34}$$

$q_{k+1}^{+} - q_{k+1}^{(0)}$ gives the correction of the solution at the grid $(k+1)$ which reduces the residual in the finer grid (k) due to the forcing terms added in the coarse grid equation above. Finally, the correction is transferred back from the coarse grid $(k+1)$ to the fine grid (k) by

$$q_k^{+} = q_k + I_{k+1}^{k}\left(q_{k+1}^{+} - q_{k+1}^{(0)}\right) \tag{2.35}$$

where I_{k+1}^{k} is an interpolation (prolongation) operator for a correction. Simple injection is used for I_{k+1}^{k} in the present scheme. A multigrid cycle employed here is V-cycle in which the equations are first solved at the finest grid and the solution moves down to the coarsest grid with an update of a solution at each grid and the interpolation is used in the transfer of correction from the coarsest grid to the finest one.

2.6. Turbulence models

A turbulence model is essential for simulating high Reynolds number flows of practical interests. There exist a number of turbulence models. They range from simple algebraic models or one - or two equations model for the eddy viscosity concept to Reynolds stress models for the second order closure. However, no model has been proved to be universally applicable to general fluid engineering problems. In practice, a turbulence model must be selected based on the characteristics of a flow field of each problem. Ship flows,

particularly stern flows, are extremely complicated because they are essentially three dimensional separated flows with strong longitudinal vortices and free surface effects cannot be neglected in some cases. These extremely complicated ship flows are beyond the capability of most of existing turbulence models[5, 19)].

Since the original Spallart - Allmaras turbulence model is known to be relatively simple and yet produce reasonable predictions for ship flows, especially flows at bow and stern. To cope with this difficulty, SURF code has adapted a newly proposed evaluation of the vorticity component in production term and has obtained Modified Spalart – Allmaras turbulence model which has proven better than original model in simulation flow field at bow and stern[20)]. Therefore, in the present study, the Modified Spalart – Allmaras turbulence model is used to simulate free surface flow and analyze effects of transom shape on stern waves. The original Spallart - Allmaras turbulence model is a one equation model which solves a transport equation for a viscosity - like variable $\tilde{\nu}$ and be described mathematically as follows[17)]:

The eddy viscosity ν_t is defined by:

$$\nu_t = \tilde{\nu} f_{\nu 1}, f_{\nu 1} \frac{\chi^3}{\chi^3 + C_{\nu 1}^3}, \chi := \frac{\tilde{\nu}}{\nu}$$

with ν is the molecular viscosity, $\tilde{\nu}$ is determined by solving the transport equation defined as following:

$$\frac{\partial \tilde{\nu}}{\partial t} + u_j \frac{\partial \tilde{\nu}}{\partial x_j} = C_{b1}[1 - f_{t2}]\tilde{S}\tilde{\nu} + \frac{1}{\sigma}\left\{\nabla.\left[\left(\frac{1}{Re} + \tilde{\nu}\right)\nabla\tilde{\nu}\right] + C_{b2}|\nabla\nu|^2\right\} - \left[C_{w1} fw - \frac{C_{b1}}{\kappa^2} f_{t2}\right]\left(\frac{\tilde{\nu}}{d}\right)^2 + f_{t1}\nabla U^2 \tag{2.36}$$

Here

$$\tilde{S} = |\omega| + \frac{\tilde{\nu}}{\kappa^2 d^2} f_{\nu 2}, f_{\nu 2} = 1 - \frac{\chi}{1 + \chi f_{\nu 1}}$$

where ω is the magnitude of the vorticity, and d is the distance to the closet wall. The function f_ω is:

$$f_\omega = g\left[\frac{1+c_{\omega 3}^6}{g^6+c_{\omega 3}^6}\right]^{1/6}, g = r + c_{\omega 2}\left(r^6 - r\right), r \equiv \frac{\tilde{\nu}}{\tilde{S}\kappa^2 d^2}$$

$$f_{t1} = c_{t1} g_t \, exp\left(-c_{t2}\frac{\omega_t^2}{\nabla U^2}\left[d^2 + g_t^2 d_t^2\right]\right), g_t \equiv min\left(0.1, \nabla U / \ \omega_t \nabla x_t\right)$$

The function f_{t2} is:

$$f_{t2} = c_{t3} \, exp\left(-c_{t4}\chi^2\right)$$

The constants are:

$$c_{b1} = 0.135, \sigma = 2/3, c_{b2} = 0.622, \kappa = 0.41, c_{\omega 1} = c_{b1}/\kappa^2 + \left(1 + c_{b2}\right)/\sigma,$$

$$c_{\omega 2} = 0.3, c_{\omega 3} = 2, c_{v1} = 7.1, c_{t1} = 1, \; c2 = 2, c3 = 1.2, c_{t4} = 0.5$$

The right hand terms of equation (2.36) represent the production, diffusion, destruction and trip.

The subscript *v* stands for "viscous".

The original Spalart - Allmaras turbulence model over-predicts the level of eddy viscosity in the core of a vortex and thus produce excessive diffusion. To reduce the eddy viscosity calculated from the original one, the vorticity component $|\omega|$ is modified as follows:

$$|\omega| \rightarrow |\omega| + C \, min\left(0, |S| - |\omega|\right)$$

where $|S|$ is the magnitude of the strain - rate tensor. The advantage of this formulation is that the eddy viscosity is reduced in the regions where the magnitude of the vorticity exceeds that of the strain rate, such as in the vortex core. On the other hands, the axial vortex correction is passive in thin shear layers where $|S|$ and $|\omega|$ are very close. C is an arbitrary constant and set to 20 in SURF code[19].

In ULBS study, the Explicit Algebraic Reynolds Stress Model (EARSM) model[9] which is based on the k –ω model[23] is used. Since separations are dominant in the flow fields

around an extremely blunt ship, it is considered that the higher-order models are better suited than the standard eddy viscosity models.

The Reynolds stress tensor $\tilde{\tau}_{ij}$ is given by the explicit algebraic relation of the average velocity fields as

$$\tilde{\tau}_{ij} = \frac{2}{3}K\delta_{ij} - 2v_t^*\left\{S_{ij} + \left[a_2 a_4\left(S_{ik}W_{kj} - W_{ik}S_{kj}\right) - 2a_3 a_4\left(S_{ik}S_{kj} - \frac{2}{3}S_{kl}S_{lk}\delta_{ij}\right)\right]\right\} \tag{2.37}$$

where $S_{ij} = \left[\left(\partial u_i/\partial x_j\right) + \left(\partial u_j/\partial x_i\right)\right]/2$ and $W_{ij} = \left[\left(\partial u_i/\partial x_j\right) - \left(\partial u_j/\partial x_i\right)\right]/2$. The nonlinear terms are within the brackets [] in equation (2.37). The component $\tilde{\tau}_{ij}$ terms are used to close the Reynolds averaged Navier-Stokes equations, as in reference [21] for details. The kinematic eddy viscosity v_t^* is given by

$$v_t^* \equiv C_\mu^* K\tau = -K\alpha_1 \tag{2.38}$$

with $\tau = 1/\omega$. Thus, α_1/τ is equivalent to $-C_\mu^*$. The value of α_1/τ is obtained from the solution to the following cubic equation at each point in the flow field:

$$\left(\alpha_1/\tau\right)^3 + p\left(\alpha_1/\tau\right)^2 + q\left(\alpha_1/\tau\right) + r = 0 \tag{2.39}$$

where

$$p = -\frac{\gamma_1^*}{\eta^2\tau^2\gamma_0^*} \tag{2.40}$$

$$q = \frac{1}{\left(2\eta^2\tau^2\gamma_0^*\right)^2}\left(\gamma_1^{*2} - 2\eta^2\tau^2\gamma_0^* a_1 - \frac{2}{3}\eta^2\tau^2 a_3^2 + 2R^2\eta^2\tau^2 a_2^2\right) \tag{2.41}$$

$$r = \frac{\gamma_1^* a_1}{\left(2\eta^2\tau^2\gamma_0^*\right)^2} \tag{2.42}$$

The correct root to choose from this equation is the root with the lowest real part. [21] Also, the degenerate case when $\eta^2 \to 0$ must be avoided. The current solution procedure used is as follows.

If $\eta^2\tau^2 < 1\times10^{-6}$, then

$$\left(\frac{\alpha_1}{\tau}\right) = -\frac{\gamma_1^* a_1}{\gamma_1^{*2} - 2\{W^2\}\tau^2 a_2^2} \tag{2.43}$$

Otherwise, define

$$a \equiv q - p^2/3 \tag{2.44}$$

$$b \equiv \frac{1}{27}\left(2p^{3-9pq+27r}\right) \tag{2.45}$$

$$d \equiv b^2/4 + a^3/27 \tag{2.46}$$

Then, if $d > 0$

$$t_1 = \left(-b/2 + \sqrt{d}\right)^{\frac{1}{3}} \tag{2.47}$$

$$t_2 = \left(-b/2 + \sqrt{d}\right)^{\frac{1}{3}} \tag{2.48}$$

$$(\alpha_1/\tau) = min\left(-p/3 + t_1 + t_2, -p/3 - t_1/2 - t_2/2\right)$$

If $d \le 0$, then

$$\theta = cos^{-1}\left(-b/2/\sqrt{-a^3/27}\right) \tag{2.49}$$

$$t_1 = -p/3 + 2\sqrt{-a/3}\,cos(\theta/3) \tag{2.50}$$

$$t_2 = -p/3 + 2\sqrt{-a/3}\,cos(2\pi/3 + \theta/3) \tag{2.51}$$

$$t_3 = -p/3 + 2\sqrt{-a/3}\,cos(4\pi/3 + \theta/3) \tag{2.52}$$

$$(\alpha_1/\tau) = min(t_1, t_2, t_3) \tag{2.53}$$

In the current implementation, the resulting $C_\mu^* = -(\alpha_1/\tau)$ is limited by $C_\mu^* = max(C_\mu^*, 0.0005)$. The nominal level for C_μ^* in a zero-pressure-gradient log layer is approximately 0.09.

Other parameters are given by

$$\eta^2 \equiv \{S^2\} = S_{ij}S_{ji} = S_{ij}S_{ij} \tag{2.54}$$

$$\{W^2\} = W_{ij}W_{ji} = -W_{ij}W_{ij} \tag{2.55}$$

$$R^2 = -\{W^2\}/\{S^2\} \tag{2.56}$$

$$a_1 = \frac{1}{2}\left(\frac{4}{3} - C_2\right) \tag{2.57}$$

$$a_2 = \frac{1}{2}(2 - C_4) \tag{2.58}$$

$$a_3 = \frac{1}{2}(2 - C_3) \tag{2.59}$$

$$a_4 = \left[\gamma_1^* - 2\gamma_0^*(\alpha_1/\tau)\eta^2\tau^2\right]^{-1}\tau \tag{2.60}$$

$$\gamma_0^* = \frac{C_1^1}{2} \tag{2.61}$$

$$\gamma_1^* = \frac{1}{2}C_1^0 + \left(\frac{C_{\varepsilon 2} - C_{\varepsilon 1}}{C_{\varepsilon 1} - 1}\right) \tag{2.62}$$

and $C_{\varepsilon 1}$=1.44, $C_{\varepsilon 2}$=1.83, C_1^0=3.4, C_1^1=1.8, C_2=0.36, C_3=1.25 and C_4=0.4.

For EARSM (*K*-ω), the explicit tensor representation for τ_{ij} is coupled with the following *K*-ω two-equation model:

$$\frac{DK}{Dt} = P - f_{\beta^*}K\omega + \frac{\partial}{\partial x_k}\left[\left(\nu + \frac{\nu_t^*}{\sigma_K}\right)\frac{\partial K}{\partial x_k}\right] \tag{2.63}$$

$$\frac{D\omega}{Dt} = \gamma\frac{\omega}{K}P - \beta\omega^2 + \frac{\partial}{\partial x_k}\left[\left(\nu + \frac{\nu_t^*}{\sigma_\omega}\right)\frac{\partial K}{\partial x_k}\right] \tag{2.64}$$

where

$$P = -\tau_{ij}\frac{\partial u_i}{\partial x_j} \approx 2\nu_t^* \eta^2 \tag{2.65}$$

and $\sigma_k = 2$, $\sigma_\omega = \kappa^2 \Big/ \left[\sqrt{C_\mu(\beta-\gamma)}\right]$, $\kappa = 0.41$, $\gamma = 0.575$, $\beta = 0.83$, and $C_\mu = 0.895$ .Note that for two-dimensional incompressible flows $P = 2\nu_t^* \eta^2$ is exact. In the current implementation, *P* in the *K* equation is limited to be less than 20 times the destruction term $f_{\beta^*} K\omega$. The function f_{β^*} from Wilcox [22] improves the performance of the *K*-ω model for two-dimensional shear layers, wakes, and jets and is given as follows.

When $\chi_k \le 0$:

$$f_{\beta^*} = 1 \tag{2.66}$$

When $\chi_k > 0$:

$$f_{\beta^*} = \frac{1+680\chi_k^2}{1+400\chi_k^2} \tag{2.67}$$

$$\chi_k = \frac{C_\mu^2}{\omega^3}\frac{\partial K}{\partial x_j}\frac{\partial \omega}{\partial x_j} \tag{2.68}$$

where the C_μ^2 term in the formula for χ_k is necessary because ω in the current model does not absorb C_μ as in Wilcox's model. The boundary conditions applied at solid walls are $K_\omega = 0$ and $\omega_\omega = 10(6\nu_\omega)/\left[\beta(\Delta n)^2\right]$, where Δn is the distance to the first cell center away from the wall. The boundary condition for ω_ω is from Menter. [23] This boundary condition simulates the analytical behavior of ω near solid walls without the need for specifying the solution at interior points.

2.7 Boundary Conditions

The free surface conditions, both dynamic and kinematic conditions are implemented in the scheme as follows. Since both the stress of air and surface tension of wave are neglected, the dynamic condition becomes no stress on the free surface. Due to the zero tangential stress condition, the viscous flux F_v vanishes on a free surface and the velocity boundary condition on a free surface can be approximated to be zero-gradient extrapolation. The condition for zero normal stress on a free surface gives the Dirichlet condition for pressure on a free surface as h/F_n^2 where h is a wave height and the atmospheric pressure is set to be zero.

The kinematic condition is used to update a free surface height. In the present scheme, the condition with use of the wave damping method, is formulated based on the mass conservation considerations [15] as

$$\frac{\Delta\zeta}{\Delta t} = \frac{S_{FS} \bullet u_{FS}}{S_{FS} \bullet n_{FS}} - W(x.y)h \tag{2.69}$$

where S_{FS} is an area vector of a cell interface, u_{FS} is a fluid velocity and n_{FS} is a unit vector whose direction is along a grid line in the girth direction on a free-surface. Here $W(x, y)$ is a weight function defined as

$$W(x,y) = A \times max(W_x(x), W_y(y))$$

$$W_x(x) = \begin{cases} \left(\frac{x - x_d}{x_0 - x_d}\right)^2 & x_d \le x \le x_0 \\ otherwise' \\ 0 \end{cases}$$

$$Wy(y) = \begin{cases} \left(\frac{y - y_d}{y_0 - y_d}\right)^2 & y_d \le y \le y_0 \\ otherwise \\ 0 \end{cases}$$

where x_d , y_d is the coordinate from which the damping region starts and x_0 , y_0 is the location of outflow and side boundary. A is the parameter which controls the intensity of damping, with a typical value of 100. Equation (2.69) is discretized by a finite-volume method at the grid node point with the first order accurate backward Euler formula in time and the third order accurate upwind differencing for other terms. Temporal discretization of

equation (2.69) is conducted in a similar way as the flow equations and also the same multi-grid strategy is used for convergence acceleration. After the wave height is computed, the computational grid is re-generated from the reference grid by the spline interpolation along the grid line in the girth direction at each time step.

The discrete boundary conditions are summarized in Table. 2.1. Note that the outflow and outer (side) boundary conditions for a wave height is to give the value of zero and a wave height in the region close to a body and symmetry plane, is extrapolated from the outside in order to avoid the singularity at the contact line between a free- surface and a solid body.

Table 2.1 Boundary conditions.

boundary	(u, v, w, ν_t)	p	h
inflow	(1, 0, 0, 0)	zero gradient	0
outflow	zero gradient	0	0
outer	zero gradient	zero gradient	0
symmetry plane	symmetry	symmetry	zero gradient
body	(0, 0, 0, 0)	zero gradient	zero gradient
free-surface	zero gradient	$h = Fr^2$	-

Chapter 3

Experimental and computational visualization of total resistance and flow field around Box-shaped Ships

3.1. Ship Models and Flow Conditions

As mentioned earlier, box-shaped ships is used for the present study, as an extreme case of ULBS. Ohashi et al.[16] conducted a series of model tests to investigate resistance characteristics of floating boxes like box-shaped caissons or pontoons. From the results of this systematic experiment, the effects of *L/B*, *B/d*, initial trim and size of round corners and so forth upon the resistance of the floating boxes have been clarified.

Table 3.1 Principal particulars of box Shapes

Box	A				B			
L_{PP}(m)	5				5			
B(m)	1.05				1.05			
d(m)	0.35				0.1868			
∇(m)	1.8375				0.9807			
L_{PP}/B	4.76				4.76			
B/d	3				5.62			
Fr(∇-based)	0.1	0.25	0.3	0.35	0.1	0.25	0.3	0.35
Fr(L_{PP}-based)	0.0495	0.1237	0.1485	0.1732	0.0892	0.1114	0.1337	0.1560
Rex10^6	1.53	3.82	4.59	5.35	2.85	3.56	4.27	4.98
Velocity(U)	0.3465	0.8661	1.0394	1.2126	0.6241	0.7801	0.9361	1.0921

From the various test cases, the principal particulars of box shape A and B with different *B/d* ratio are selected based on the similarity of particulars of ULBS. The principal

particulars and flow conditions are listed in Table 3.1. The box shapes A and B have the same length and breadth, while the draft of Box A is approximately twice of that of Box B. The effect of breadth-draft ratios *B/d* upon resistance and flow field is investigated by means of numerical simulations.

In order to compare the computational results, the following non-dimensional form is adopted for total resistance,

$$C_t = \frac{R_T}{1/2\,\rho \nabla^{2/3} U^2} \tag{3.1}$$

where

R_T: total resistance (kg)

ρ: density of water (kg.sec^2.m^{-4})

∇: displacement (m^3)

U: flow velocity (m.sec^{-1})

The Froude number range is set based on the values of displacement-based F_∇ which is defined as

$$F_\nabla = \frac{U}{\sqrt{g\nabla^{1/3}}} \tag{3.2}$$

Whereas the length-based Froude number, F_r is defined as

$$F_r = \frac{U}{\sqrt{gL_{pp}}} \tag{3.3}$$

Also Reynolds numbers are estimated based on water temperature of the experimental data as follows in order to compare results in the same condition as the experiment.

$$Re = \frac{UL_{pp}}{\nu} \tag{3.4}$$

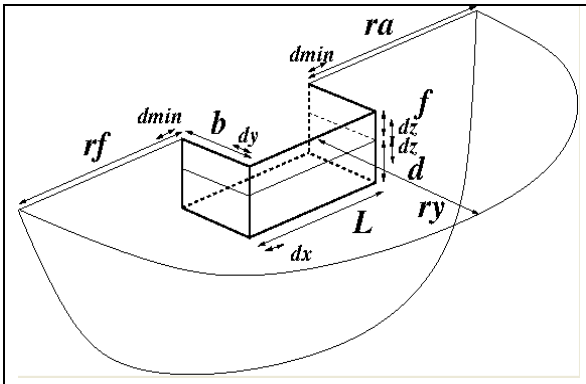

L=length

b= half breath

d=draft

f=freeboard

r_f=distance from bow to inflow

r_a=distance from bow to outflow

r_y=distance from side wall

to outer boundary

Figure 3.1 Grid parameters

The computational grids are generated based on the block-structured topology. Parameters for grids are shown in Figure 3.1. The outer grid block is O-O topology and the inner block is H-O topology. The outer block which contains the side wall of the box has O-O topology with (*nx*) x (*nz*) x (*ndivr)* cells. The inner block which contains the front and black walls together with the bottom wall of the box has H-O topology with (*nx*) x (2*nz*) x (*ndivr*) cells. Where the *nx, ny, nz* are number of cells on the box walls in *x, y* and *z* directions, and *ndivr* is cell number from wall to outer boundary, respectively. The number of cells for ship A and B are listed in Table 3.2. Note that only the half domain is discretized due to symmetry of geometry. Partial views of computational grids for each case are shown in Figure 3.2.

Table 3.2 Number of grid cells

	O-O Topology			H-O Topology			
	nx	nz	ndivr	nx	2xnz	ndivr	Cells
Box A	80	96	128	80	2x96	128	1,679,360
Box B	80	56	128	80	2x56	128	1,064,960

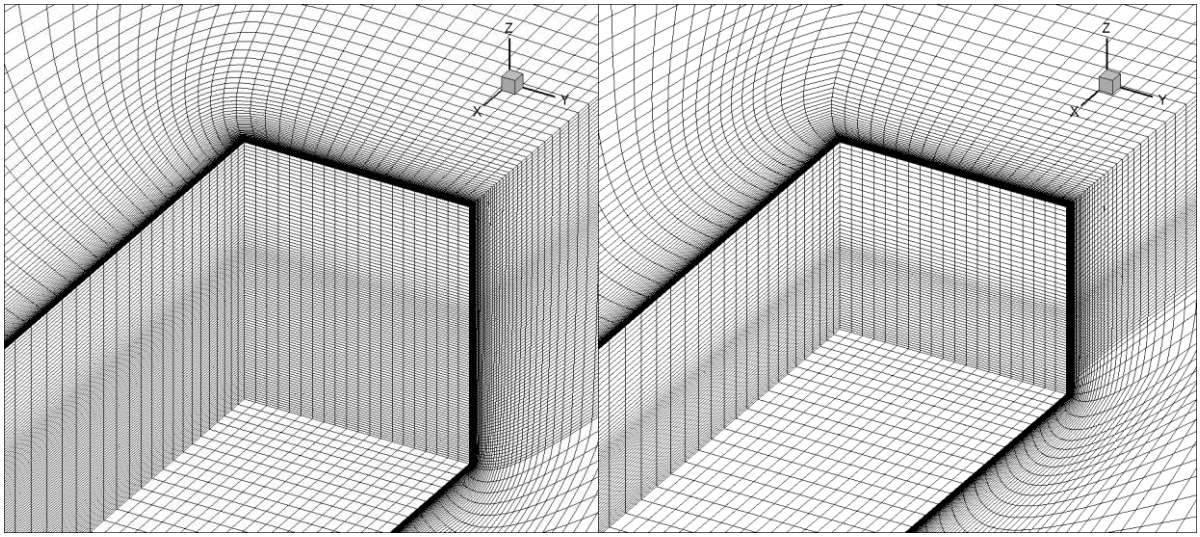

Figure 3. 2 Partial View of unstructured grids around the stern of the Box Shape. Box A (Left) and Box B (Right).

3.2 Verification and validation

The verification and validation procedure for the present results are also performed in this study. In order to validate the computational method against experimental results, the uncertainty related to the computational method is estimated. When the numerical uncertainty is known, the validation can be conducted by means of comparison with experimental data.

Verification is defined as the process of a determining that a model implementation accurately represents the developer's conceptual description of the model and the solution to the model [11].The simulation error $\boldsymbol{\delta}_S$ is defined as the difference between a simulation results S and the truth T and is composed of additive modeling $\boldsymbol{\delta}_{\mathrm{SM}}$ and numerical $\boldsymbol{\delta}_{\mathrm{SN}}$ error. For certain conditions, both the sign and magnitude of the numerical error can be estimated as $\delta_{SN} = \delta_{SN}^{*} + \varepsilon_{SN}$ where δ_{SN}^{*} is an estimate of the sign and magnitude of δ_{SN}; and ε_{SN} is the error in that estimate. The simulation value is corrected to provide a numerical benchmark SC, which is defined as [12]:

$$S_C = S - \delta_{SN}^{*} \tag{3.5}$$

For the uncorrected simulation approach, numerical error is decomposed into contributions from iteration number δ_I, grid size δ_G, time step δ_T and other parameters δ_P, which gives the following expression for simulation numerical uncertainty:

$$U_{SN}^2 = U_I^2 + U_G^2 + U_T^2 + U_P^2 \tag{3.6}$$

For the corrected simulation approach, the solution is corrected to produce a numerical benchmark S_C and the estimated simulation numerical error δ_{SN}^* and corrected uncertainty $U_{S_C N}$ are given by:

$$\delta_{SN}^* = \delta_I^* + \delta_G^* + \delta_T^* + \delta_P^* \tag{3.7}$$

$$U_{S_C N}^2 = U_{I_C}^2 + U_{G_C}^2 + U_{T_C}^2 + U_{P_C}^2 \tag{3.8}$$

Iterative and parameter convergence studies are conducted using multiple solutions with systematic parameter refinement by varying the i^{th} input parameter $\boldsymbol{\Delta}_{\mathrm{xi}}$ while holding all other parameters constant. Convergence study requires a minimum of m = 3 solution to evaluate convergence with respect to input parameter.

The grid uncertainty, U_G, is estimated based on three symmetrically refined grids. The procedure is in accordance with the Recommendation of ITTC [11), 12)].

The changes in solution between coarse and medium grids, $\varepsilon_{G_{32}} = S_3 - S_2$ and between medium and fine grids, $\varepsilon_{G_{21}} = S_2 - S_1$ are used to calculate the convergence ratio $R_G = \varepsilon_{G_{21}} / \varepsilon_{G_{32}}$, where S_1, S_2, S_3 are solutions of fine, medium and coarse grid. Depending on the value of R_G three conditions can occur:

(i) $0 < R_G < 1$, monotonic convergence,

(ii) $R_G < 0$, oscillatory convergence,

(iii) $1 < R_G$, grid divergence.

In condition (iii) no uncertainty can be estimated. In condition (ii) the uncertainty is estimated by

$$U_G = \left| \tfrac{1}{2} (S_U - S_L) \right| \tag{3.9}$$

where S_U and S_L are the maximum and minimum of the solutions from the considered grids. In condition (i) grid convergence occurs and generalized Richardson extrapolation (RE) is used to estimate the grid error $\delta^{*(1)}_{RE_{G1}}$ and the order of accuracy P_G, which are given as

$$\delta^{*(1)}_{RE_{G1}} = \frac{\varepsilon_{G_{21}}}{r_G^{P_G} - 1} \tag{3.10}$$

and

$$P_G = \frac{ln(\varepsilon_{G_{21}} / \varepsilon_{G_{32}})}{ln(r_G)} \tag{3.11}$$

$r_G = \Delta x_{G2} / \Delta x_{G1} = \Delta x_{G3} / \Delta x_{G2}$ is the refinement factor, which defines the relation between the considered grids. When $\delta^{*(1)}_{RE_{G1}}$ and P_G are known it is possible to estimate the grid uncertainty. There are two ways to do this depending on whether the solutions are close to the asymptotic range or not. If the correction factor defined by

$$C_G = \frac{r_G^{P_G} - 1}{r_G^{P_{Gest}} - 1} \tag{3.12}$$

where P_{Gest} is the limiting or theoretical accuracy of the applied numerical method, is close to unity, the solution are closed to the asymptotic range. The numerical error, δ^*_{SN} , benchmark, S_C and uncertainty , U_{GC} can be calculated from

$$\delta^*_{SN} = C_G \delta^{*(1)}_{RE_{G1}} \tag{3.13}$$

$$S_C = S - \delta^*_{SN} \tag{3.14}$$

$$U_{G_C} = \left|1 - C_G\right| \left|\delta^{*(1)}_{RE_{G1}}\right| \tag{3.15}$$

If the correction factor is away from unity only the numerical uncertainty is calculated

$$U_G = (2\left|1 - C_G\right| + 1) \left|\delta^{*(1)}_{RE_{G1}}\right| \tag{3.16}$$

3.3 Validation

Validation is defined as a process for assessing simulation modeling uncertainty U_{SM} by using benchmark experimental data and when conditions permit, estimating the sign and

magnitude of the modeling error $\boldsymbol{\delta}_{\mathrm{SM}}$ itself. The comparison error E is given by the difference in the data D and simulation S values [12]:

$$E = D - S = \delta_D - (\delta_{SM} + \delta_{SN}) \tag{3.17}$$

Modeling errors $\boldsymbol{\delta}_{SM}$ can be decomposed into modeling assumptions and use of previous data. To determine if validation has been achieved, E is compared to the validation uncertainty U_V given by:

$$U_V^2 = U_D^2 + U_{SN}^2 \tag{3.18}$$

If $|E| < U_V$, the combination of all errors in D and S is smaller than U_V and validation is achieved at the U_V level. If $U_V \langle\langle |E|$, the sign and magnitude of $E \approx \delta_{SM}$ can be used to make modeling improvements. For the corrected simulation, equations equivalent to (3.17), (3.18) are:

$$E = D - S_C = \delta_D - (\delta_{SM} + \varepsilon_{SN}) \tag{3.19}$$

$$U_{V_C}^2 = U_{E_C}^2 - U_{SM}^2 = U_D^2 + U_{S_C N}^2 \tag{3.20}$$

When the numerical uncertainty is known, the validation can be conducted by means of comparison with experimental data. In order to determine if validation is obtained the comparison error $E=D-S$ (D and S are experimental and computed values, respectively) and the validation uncertainty $U_V^2 = U_D^2 + U_{SN}^2$ (U_D is the data uncertainty), must be determined. In unsteady cases, the numerical uncertainty is evaluated by $U_{SN}^2 = U_I^2 + U_G^2$. When these quantities are known, validation at the U_V level is achieved if the combination of the errors in D and S is smaller than the validation uncertainty, i.e. when $|E| < U_V$.

Table 3.2 shows the total resistance coefficients C_t obtained with the three systematically refined grids of the Box A. Table 3.3 shows similar data of the Box B. The results of verification are shown in Table 3.4. The refinement ratio used for the grid convergence is $r_G = \sqrt{2}$ as stated above. For the Box A, R_G is estimated to -0.193 which shows the oscillatory convergence, while R_G=0.171 in the Box B shows the monotonic convergence.

In case of the box A, the grid uncertainty U_G is estimated from Equation (3.16) as 1.06% of S_1 (the fine grid solution). In case of the Box B, the further analysis is possible as shown in Table 3.5 and the grid uncertainty is estimated as 0.747% of S_1. Since the correction factor is 4.86 and away from unity, only the grid uncertainty U_G is estimated from Equation (3.9).

In order to conduct the validation, the experimental uncertainty U_D is required. However, since U_D is not available for the present case, only the comparison error are estimated as -5.62%D for Box A and 1.48%D for Box B.

Table 3.3 Grid convergence study of total resistance Ct (x10^{-2}) for Box A, F_{∇} =0.25

Box A	Coarse 3	Medium 2	Fine 1	Experiment
Cell No.	209,920	636,416	1,679,360	-
C_t	1.483	1.4524	1.4577	1.38
ε		+1.71%	-0.41%	

% of finer grid value

Table 3.4 Grid convergence study of total resistance Ct (x10^{-2}) for Box B, F_{∇} =0.25

Box B	Coarse 3	Medium 2	Fine 1	Experiment
Cell No.	133,120	388,608	1,064,960	-
C_t	0.8647	0.8442	0.8407	0.888
ε		+2.85%	+0.42%	

% of finer grid value

Table 3.5 Verification of total resistance C_t for Box A and Box B, F_{∇} =0.25

Box	R_G	P_G	C_G	U_G %S_1	δ_G^* %S_1	U_{G_C} %S_1	S_C
A	-0.193	-	-	1.06	-	-	-
B	0.171	5.10	4.86	0.73	0.41	0.65	8.37E-03

Table 3.6 Validation of total resistance C_t for Box A and Box B, F_{∇} =0.25

		E%=(D-S)x100/D
C_t	Box A	5.62
	Box B	4.89

3.4 Comparison of total resistance coefficient

Figure 3.3 shows the comparison of total resistance coefficient between CFD and experimental results. The resistance coefficient of Box A is higher than that of Box B due to the larger draft. From a quantitative point of view the calculated resistance is over-predicted with 5.62% (average of all speeds) in Box A and under-predicted with 4.89 % in Box B which is the same tendency of the comparison errors at F_{∇} =0.25. Although the reason for over-prediction in Box A and under-prediction in Box B is not known, it may be related to modeling uncertainty associated with turbulence modeling. However, the tendency of the slope of the resistance curves is well reproduced by the computations. The error bars show the grid uncertainty of 1.06% in Box A and 0.747% in Box B.

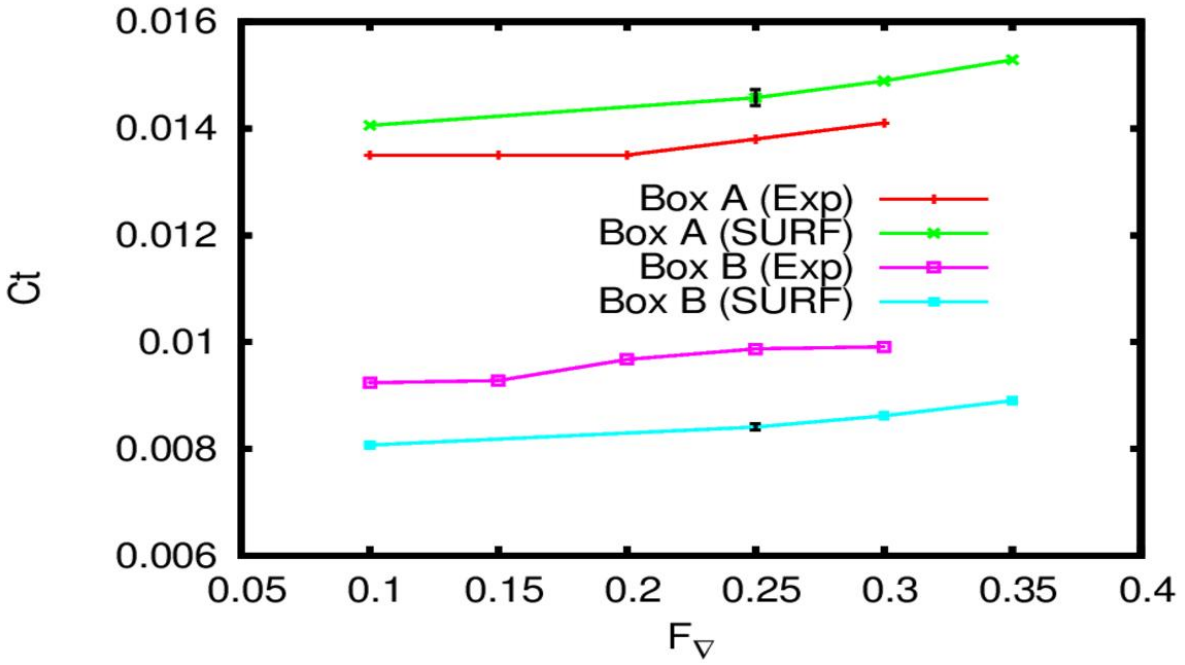

Figure 3.3 Comparisons of total resistance coefficients between CFD and Experimental results for Box A and Box B.

Figure 3.4 shows the comparison of wave profiles along the center plane and the side wall of Box A and Box B. The bow wave exhibit the peak on the front face followed by the trough at the fore corner. The trough appears again in the aft corner and stern wave is generated behind the box. This tendency is common for all Froude numbers, although the maximum wave height at the bow is only 0.5% of the draft and no significant waves are observed at F_∇ =0.1. The maximum and minimum amplitudes of waves become larger with increasing Froude number. Also, the wave amplitudes in Box B are lower than in Box A because the draft of Box B is about half of Box A.

In Figure 3.5, pressure distributions on the center plane and the side wall of the boxes are shown. With respect to the pressure field, high pressure regions near the bow due to stagnation are observed. It seems the extent of the high pressure regions afore of the front face is larger in Box A which has the deeper draft than Box B. In the side wall aft of the corner, pressure decreases which corresponds to the wave trough in Figure 3.4. Further downstream, pressure becomes almost constant since the side wall is flat there. The pressure distributions do not show large differences for the same box shape regardless of the Froude numbers.

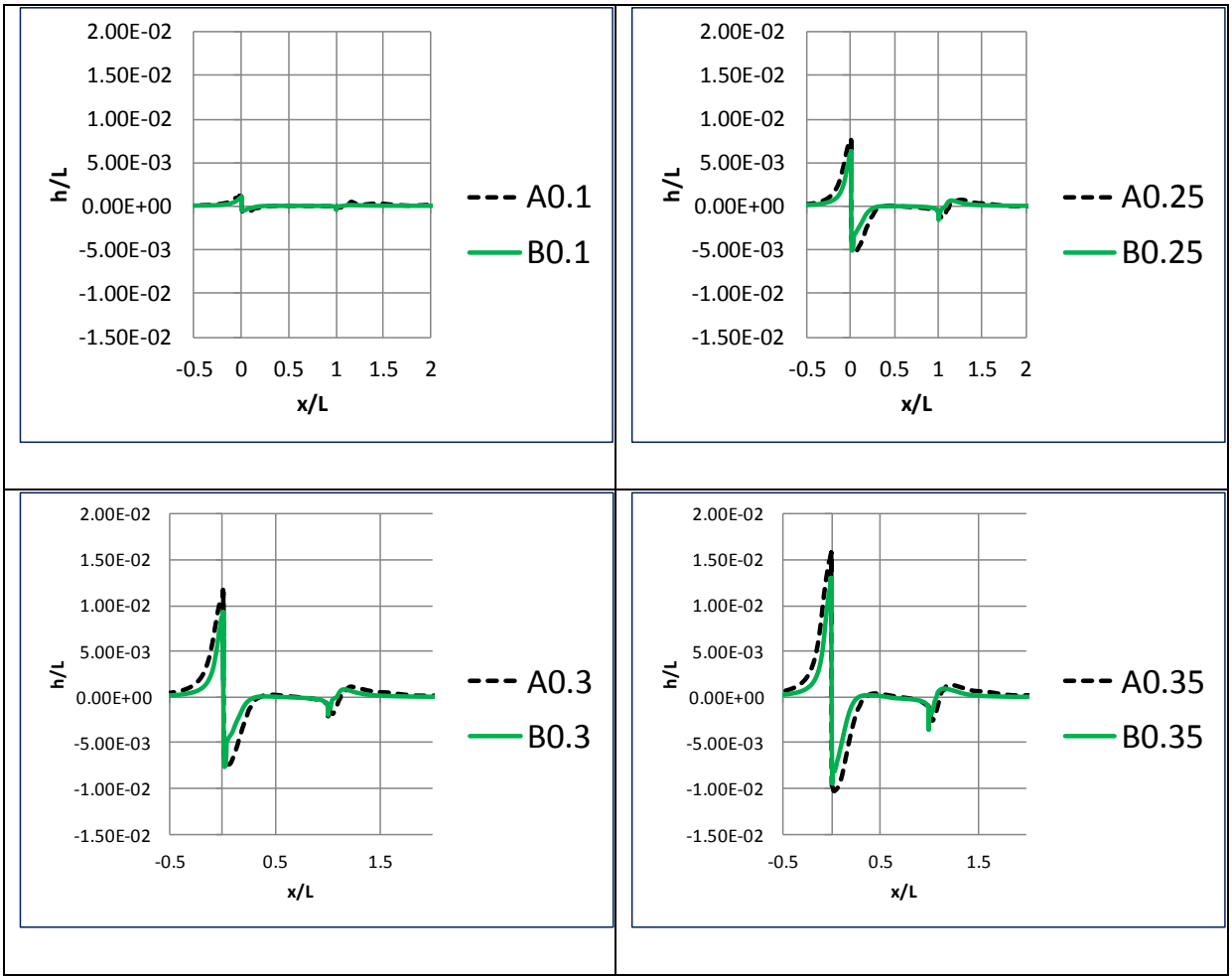

Figure 3.4 Comparison of wave profiles between Box A and Box B at the same Froude numbers F_∇ =0.1, 0.25, 0.3 and 0.35 (from top left to right bottom).

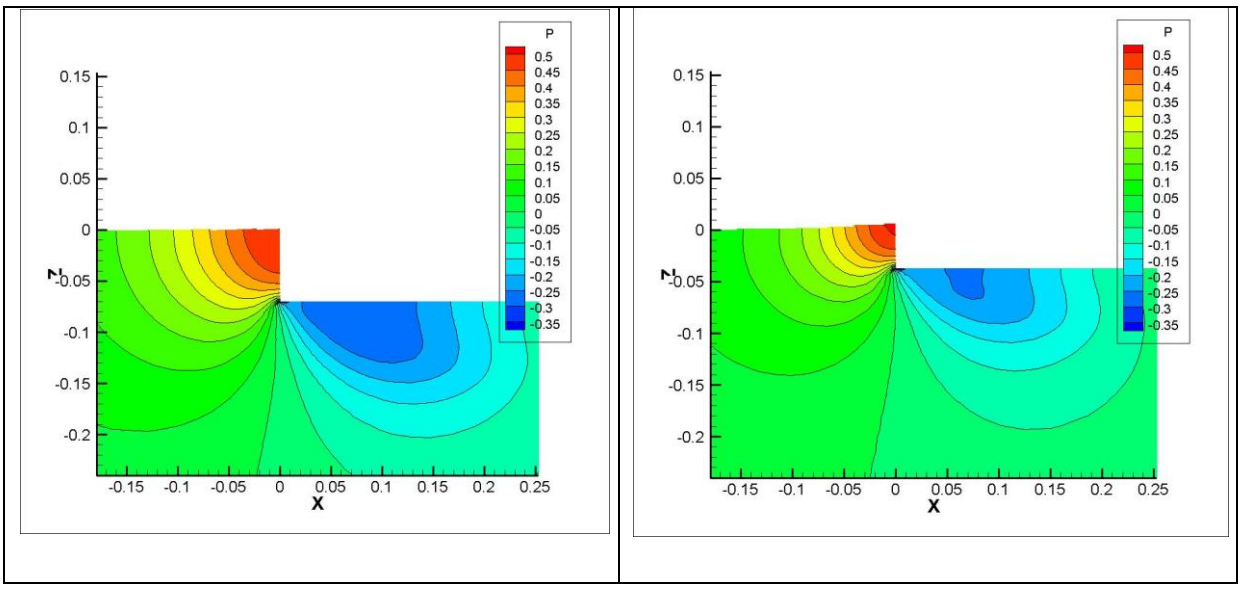

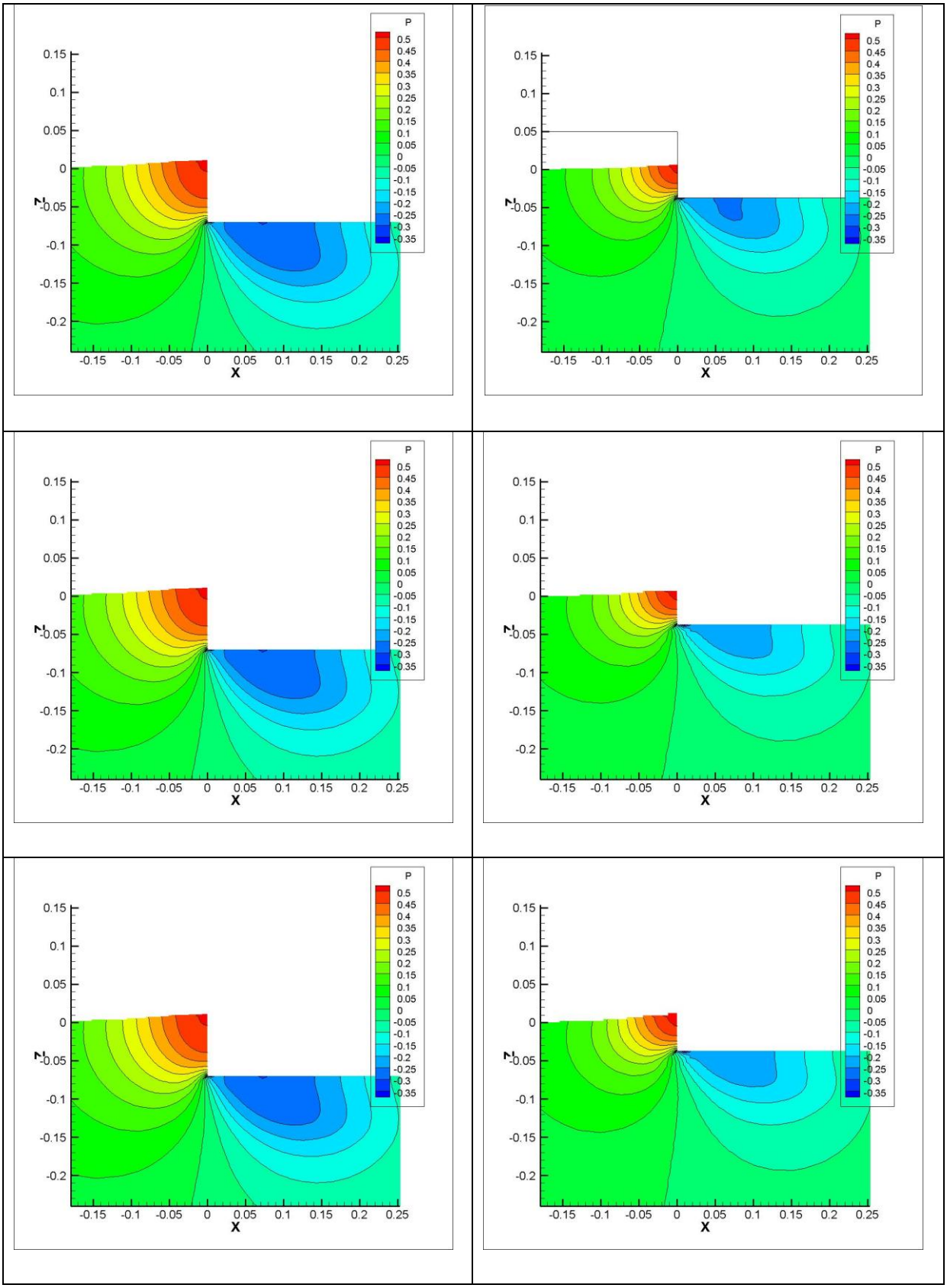

Figure 3.5 Pressure distributions and velocity contour line at the center plane near the bottom of the Box A (Left) and Box B (Right), (From top to bottom, F_{∇} =0.1, F_{∇} =0.25, F_{∇} =0.3 and F_{∇} =0.35).

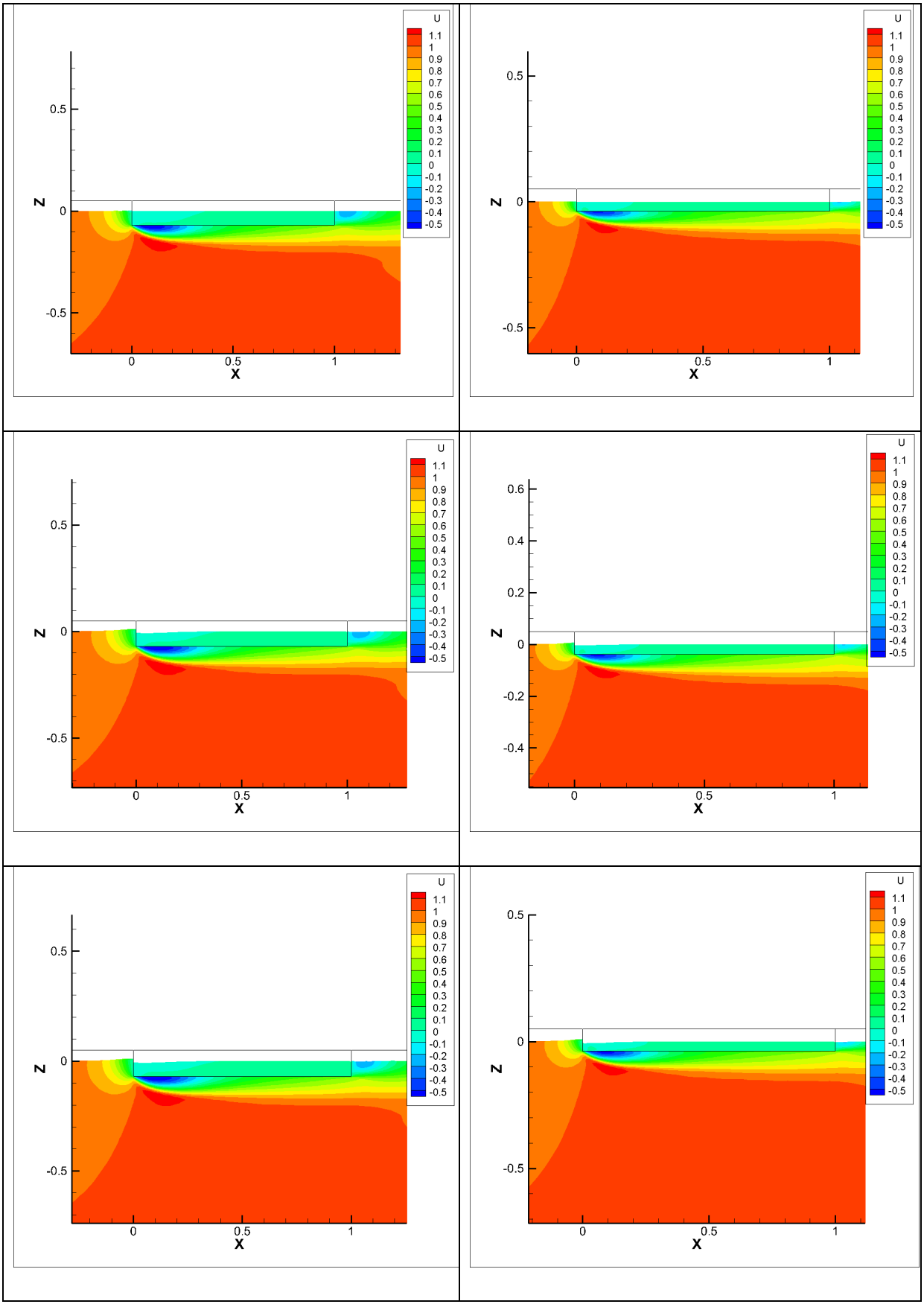
U
1.1
1
0.9
0.8
0.7
0.6
0.5
0.4
0.3
0.2
0.1
0
-0.1
-0.2
-0.3
-0.4
-0.5
Z
X
0
0.5
1
-0.5
0.6
0.4
0.2
-0.2
-0.4

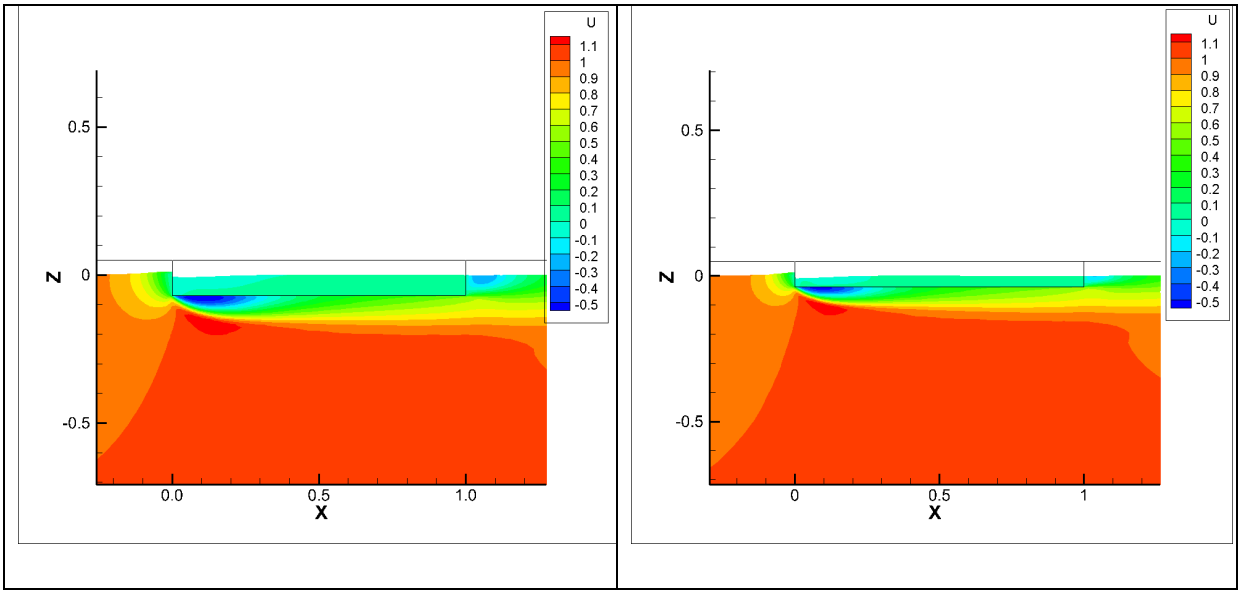

Figure 3.6 Velocity distributions and streamlines on the free surface of the Box A (Left) and Box B (Right), (From top to bottom, F_{∇} =0.1, F_{∇} =0.25, F_{∇} =0.3 and F_{∇} =0.35).

Figure 3.6 shows *u*, velocity distributions in the *x*- direction, at the center plane and the side wall of the boxes. The velocity *u* on the side wall of the boxes is zero because of no slip condition. The separation occurs under the bottom of the bow due to the sharp corner of the boxes. The velocity distributions in the bottom of Box A and Box B show similar tendency and the separation on the bottom is followed by the boundary layer evolution and these are not dependent on Froude numbers or draft of the boxes. On the other hand, flow fields behind the stern end show differences between Boxes A and B. It seems the separation is stronger in Box A than in Box B and again it may be attributed to the difference of the draft.

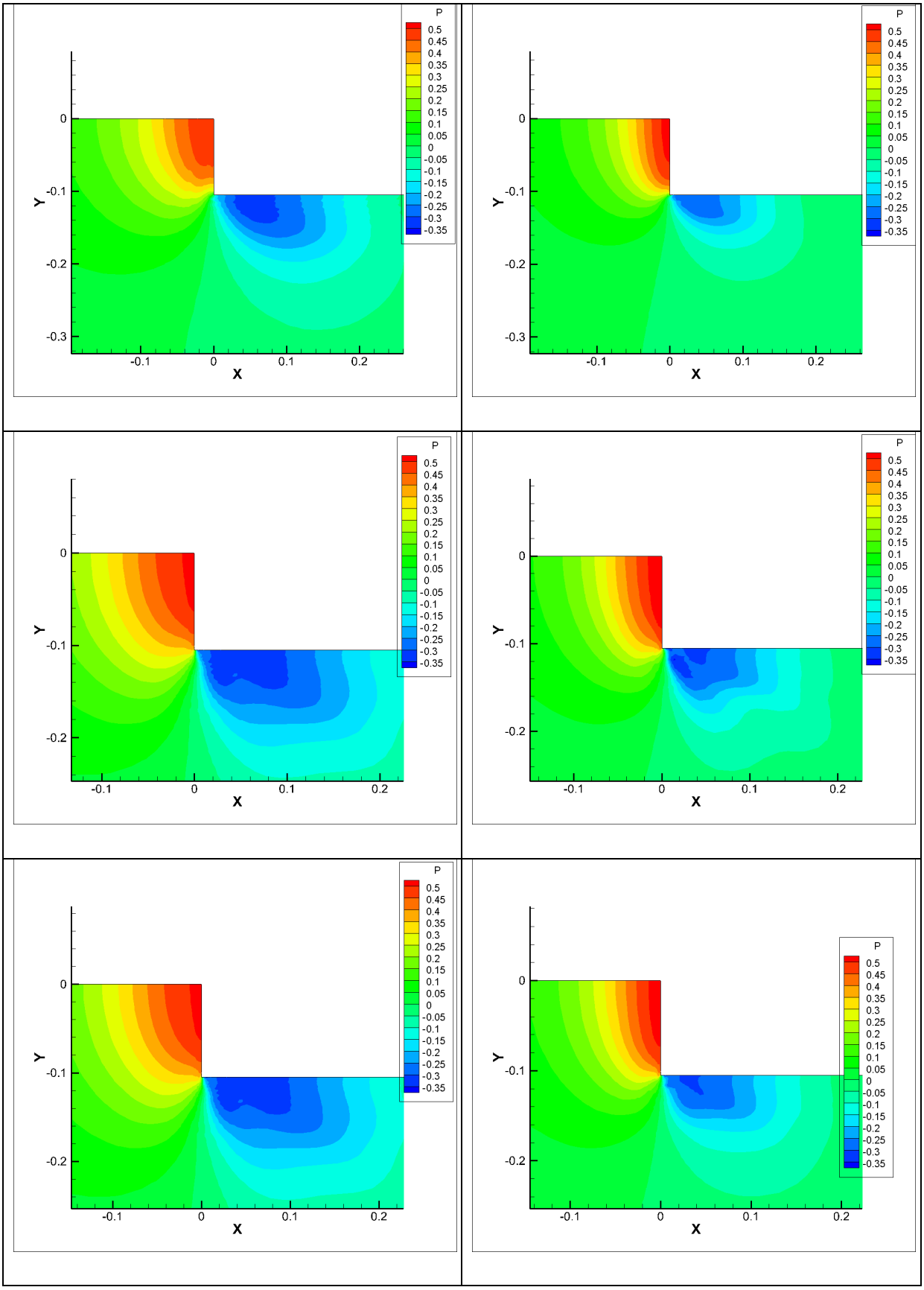
P
0.5
0.45
0.4
0.35
0.3
0.25
0.2
0.15
0.1
0.05
0
-0.05
-0.1
-0.15
-0.2
-0.25
-0.3
-0.35
Y
X
0
-0.1
-0.2
-0.3
-0.1
0
0.1
0.2

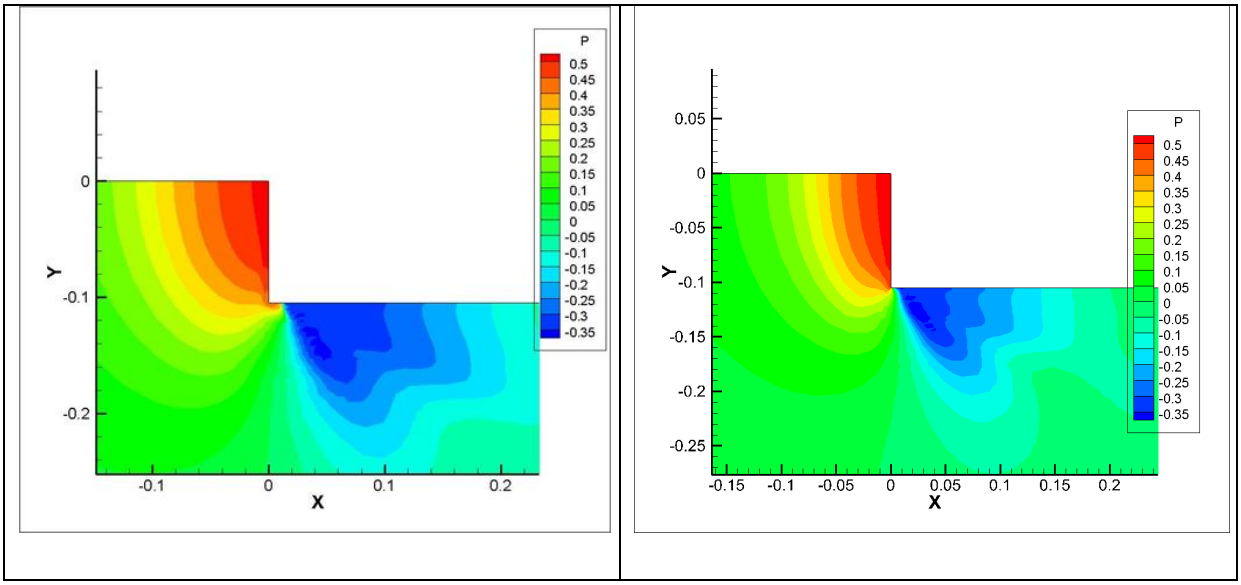

Figure 3.7 Wave height near the bow of the Box A (Left) and Box B (Right), (From top to bottom, F_{∇} =0.1, F_{∇} =0.25, F_{∇} =0.3 and F_{∇} =0.35).

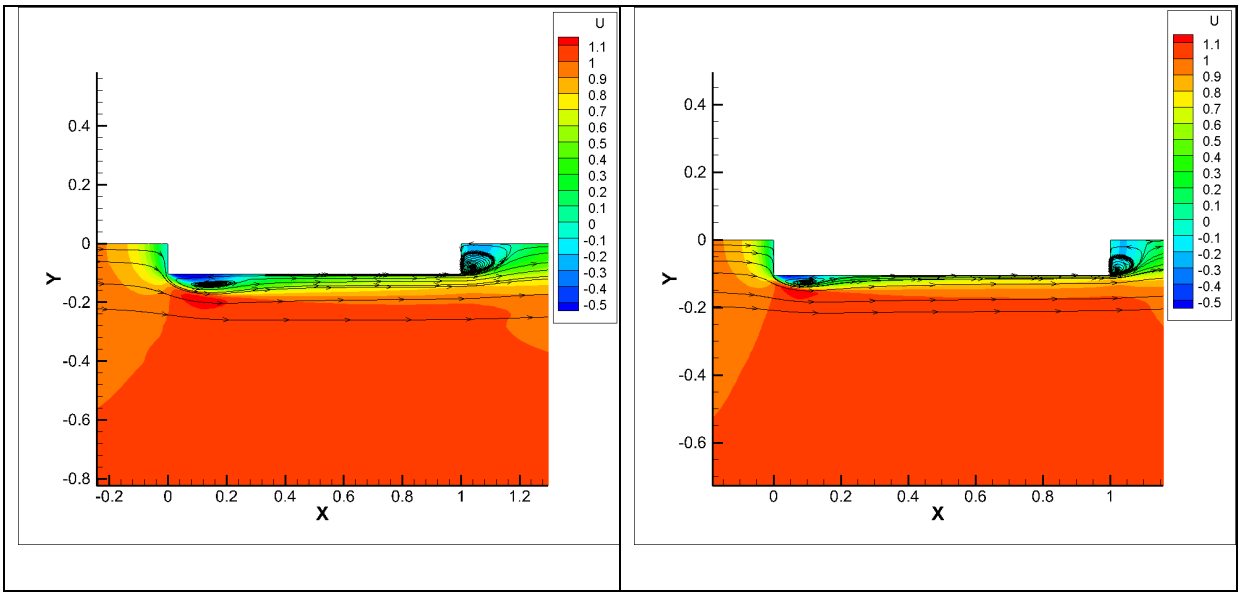

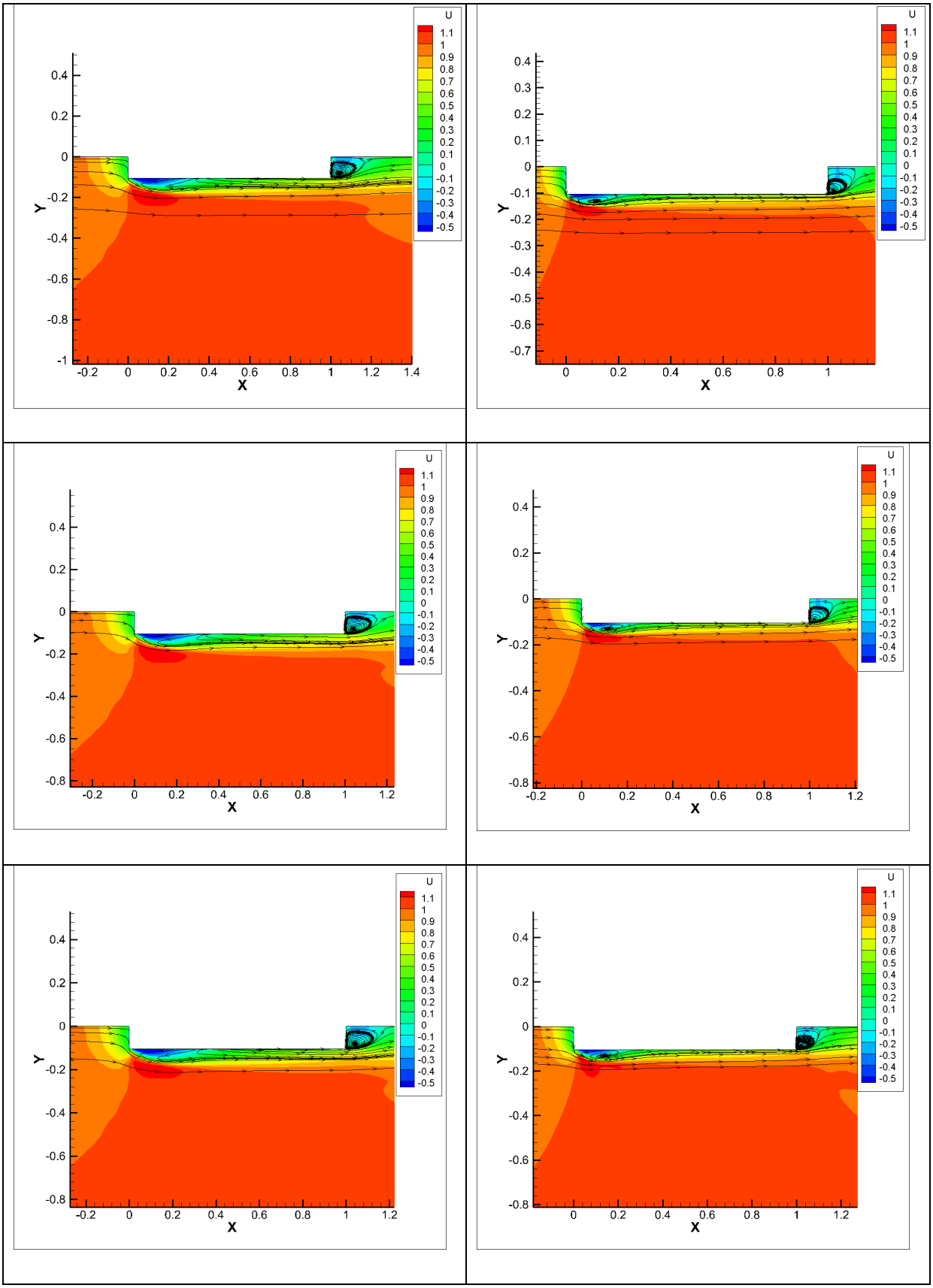

Figure 3.8 Velocity distributions and streamlines on the free surface of the Box A (Left) and Box B (Right), (From top to bottom, F_{∇} =0.1, F_{∇} =0.25, F_{∇} =0.3 and F_{∇} =0.35).

Figure 3.8 shows velocity distributions and streamlines on the free surface around the boxes. The flow separations can be seen behind the fore corners on the side of the boxes and its length is longer in Box A than in Box B, which corresponds to the extents of low pressure zone in Figure 3.6. The separation regions behind the stern are stronger in Box A than in Box B. It is the same tendency as the velocity in the center plane in Figure 3.7.

Figure 3.9 shows streamlines plot of Box A for F_{∇}=0.3. It is clear that the streamlines around the bow of the bluff body are really complicated. Therefore the modify advance turbulence model should be used to capture the complicated flow features.

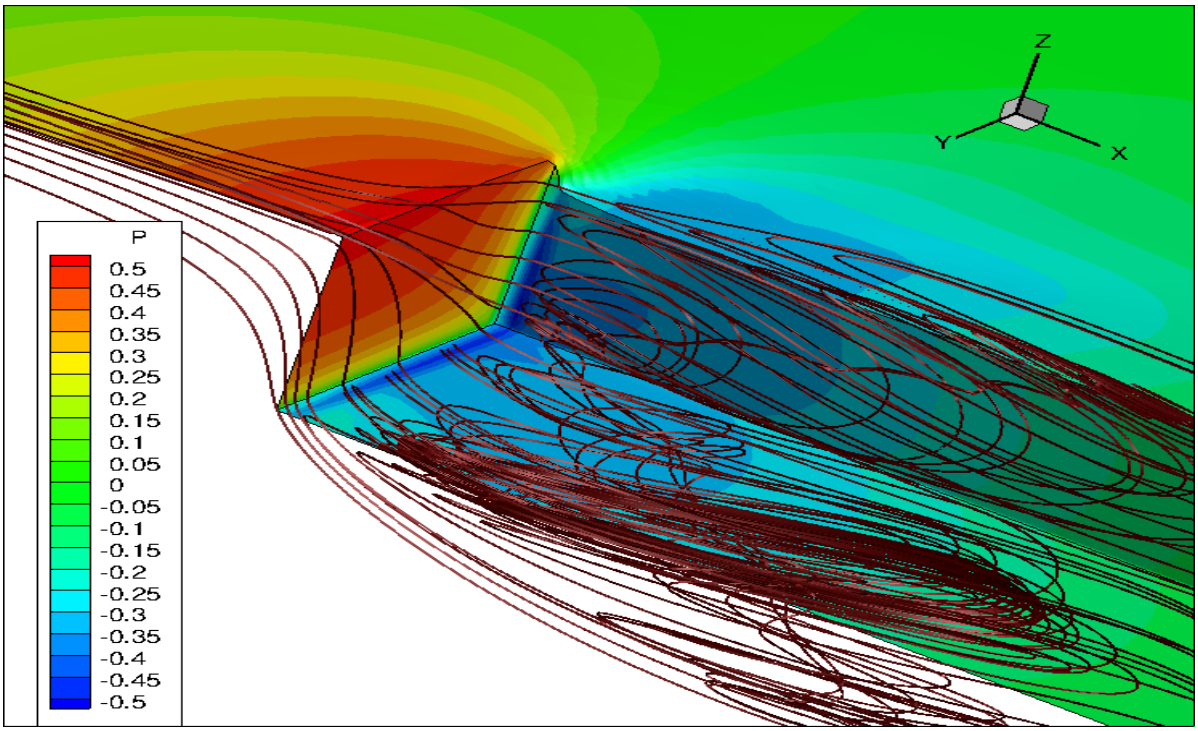

Figure 3.9 Streamlines plot of Box A for F_{∇}=0.3.

Chapter 4

Experimental and computational visualization of total resistance and flow field around ULBS

4.1. Model tests of ULBS

A schematic plan of ULBS suggested in Yokohama National University is shown in Figure 4.1. For the practical goal of ULBS, various new ideas should be introduced to reduce fluid resistance and to improve propulsive performance as shown in Figure 4.1. In this paper, as one of the investigations for ULBS, the verification of total resistance and the comparison of flow fields around ULBS with and without a stern tunnel are discussed.

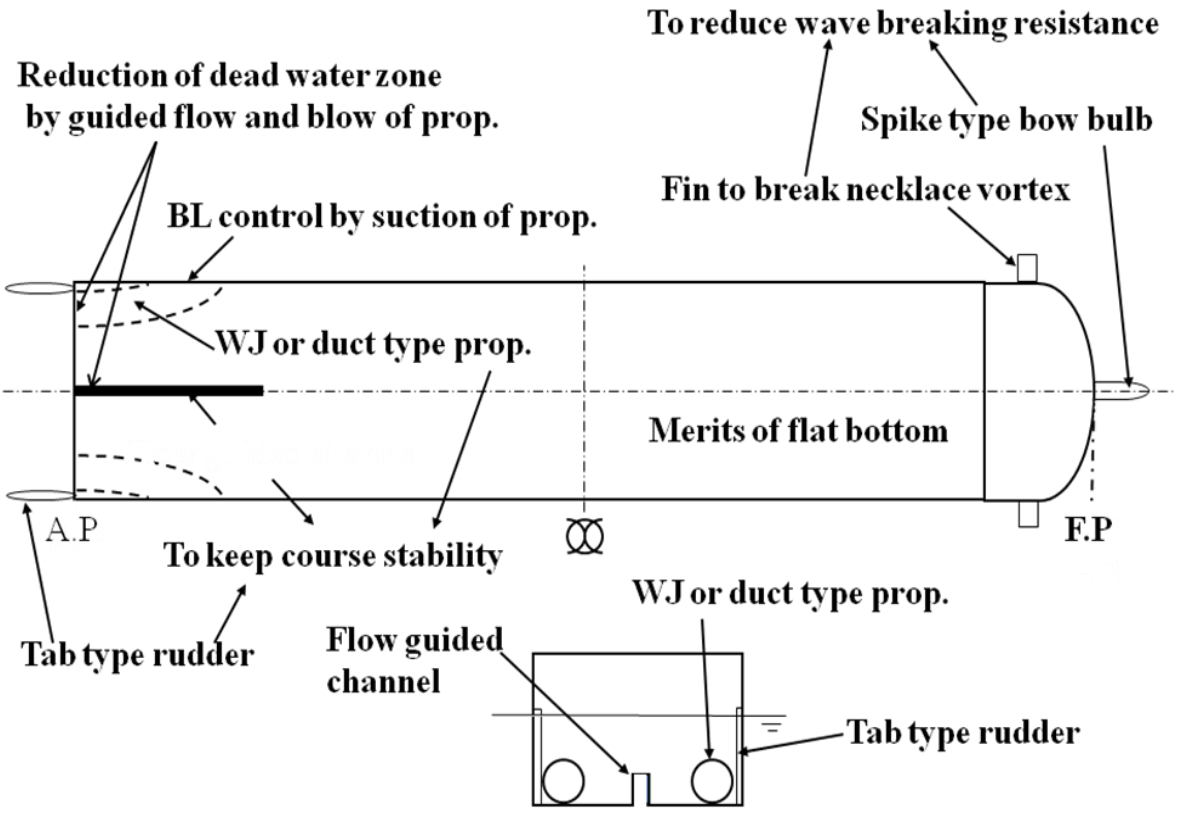

Figure 4. 1 Schematic plan of ULBS.

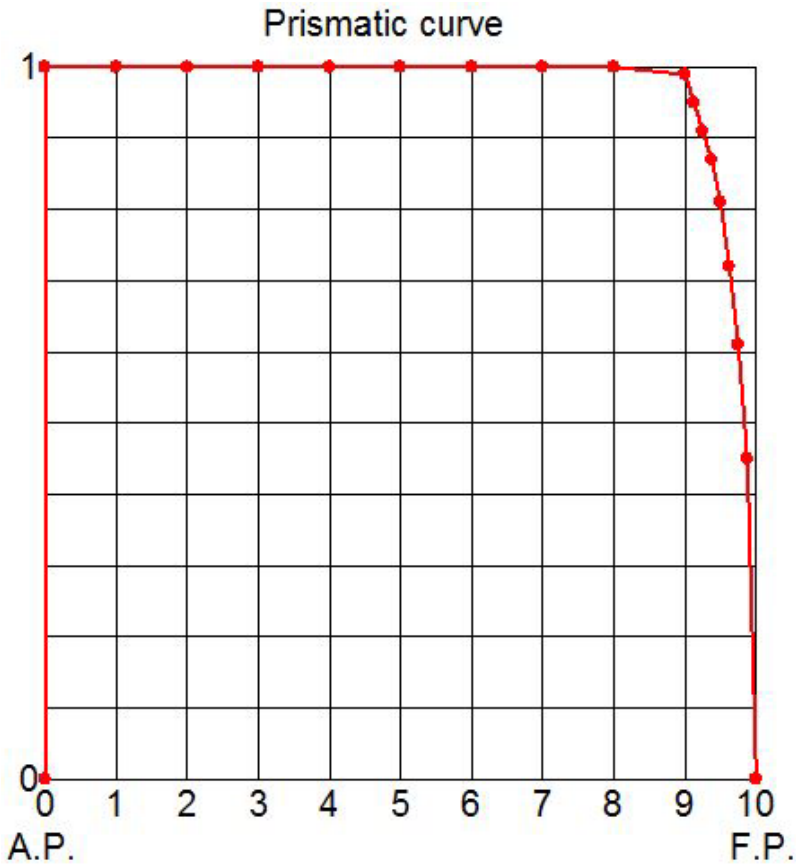

Figure 4. 2 Prismatic curve of ULBS.

4.2 Formulation for model ship

To correlate the experimental and computational results, the formulations of ULBS models are defined as follows. Symbols used in these formulations are given in Figure 4.3. The model ship is formulated by using the following procedure.

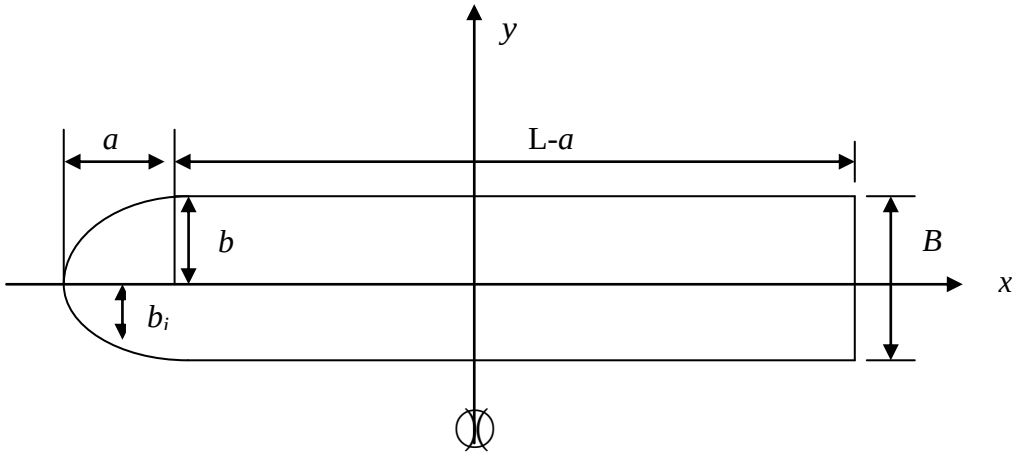

Figure 4. 3 Water plane of tested model ship

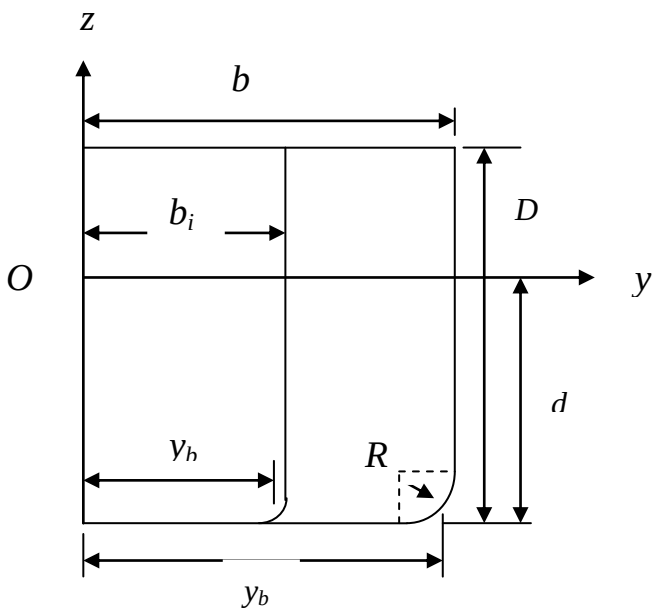

Figure 4. 4 Cross section of tested model ship

The Midship section coefficient,

$$\begin{aligned} C_M &= \frac{b(d-R)+R(b-R)+\pi R^2/4}{bd} \\ &= \frac{4bd+R^2(\pi-4)}{4bd} \\ &= 1+\frac{R^2(\pi-4)}{4bd} \end{aligned} \tag{4.1}$$

Displacement of model,

$$\begin{aligned} \nabla &= V_{parallelbody}+V_{ellipticalbow} \\ &= (L-a)BdC_M+\frac{\pi aBdC_M}{4} \\ &= LBdC_M+\frac{aBdC_M(\pi-4)}{4} \end{aligned} \tag{4.2}$$

Block coefficient of the model,

$$\begin{aligned} C_b &= \frac{\nabla}{LBd} \\ &= C_M+a\frac{C_M(\pi-4)}{4L} \end{aligned} \tag{4.3}$$

From equation (4.3), the length of elliptic section for the model ship,

$$a = \frac{4L(C_M-C_b)}{C_M(4-\pi)} \tag{4.4}$$

The maximum half breadth in the elliptic section of the hull,

$$b_i = b\cdot\sqrt{1-\frac{1}{a^2}\left(x-\frac{L}{2}+a\right)^2} \tag{4.5}$$

The half breadth at Midship, $y_b = b-R+R\sin\theta$

$$= b-R(1-\sin\theta) \tag{4.6}$$

And the half breadth at the elliptic section,

$$y_{bi} = \frac{b_i}{b} y_b \tag{4.7}$$

4.3 Experiment and Computational Conditions

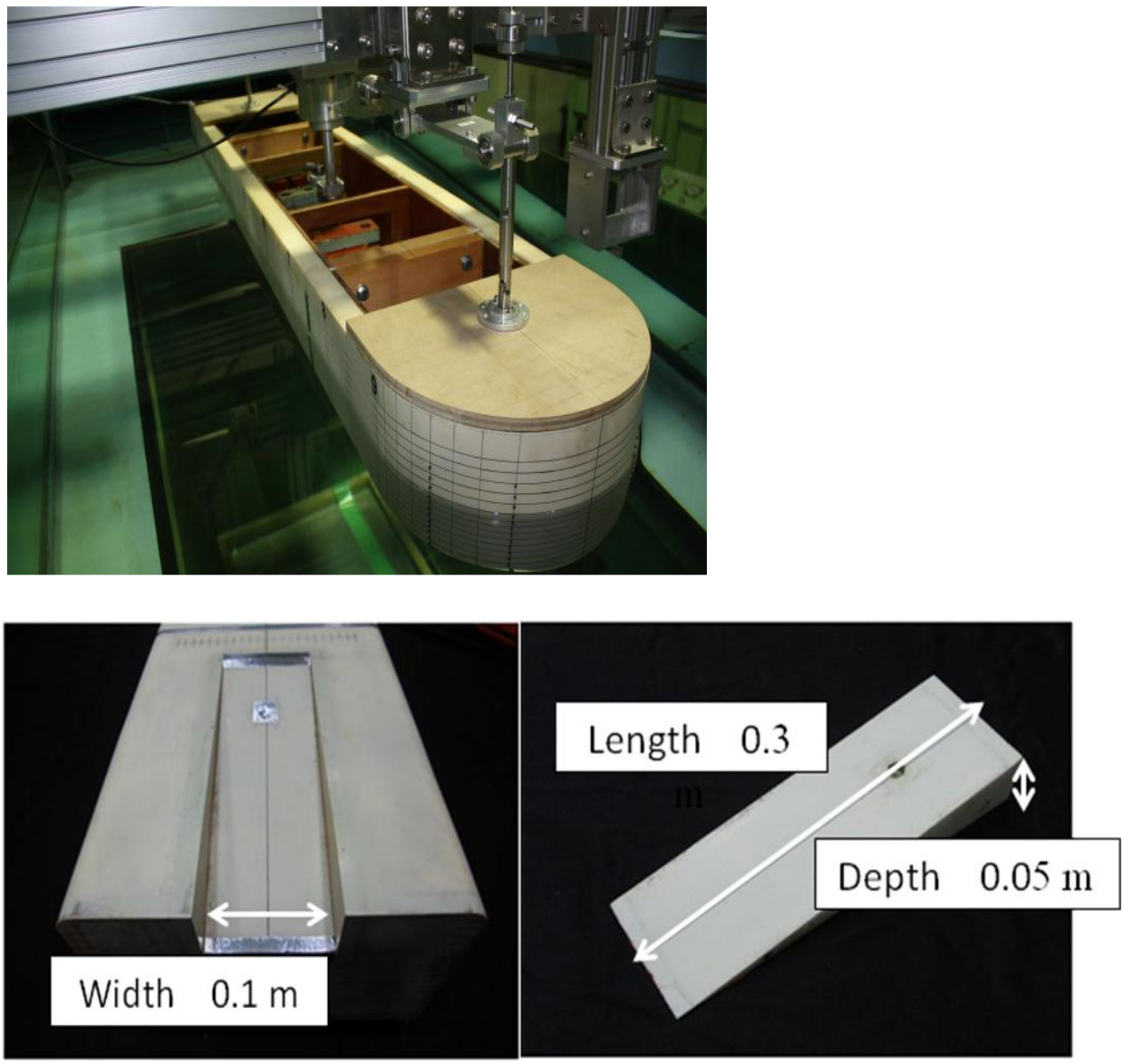

Figure 4. 5 Model ship (top) and Stern tunnel shape (bottom) (Experimental Conditions)

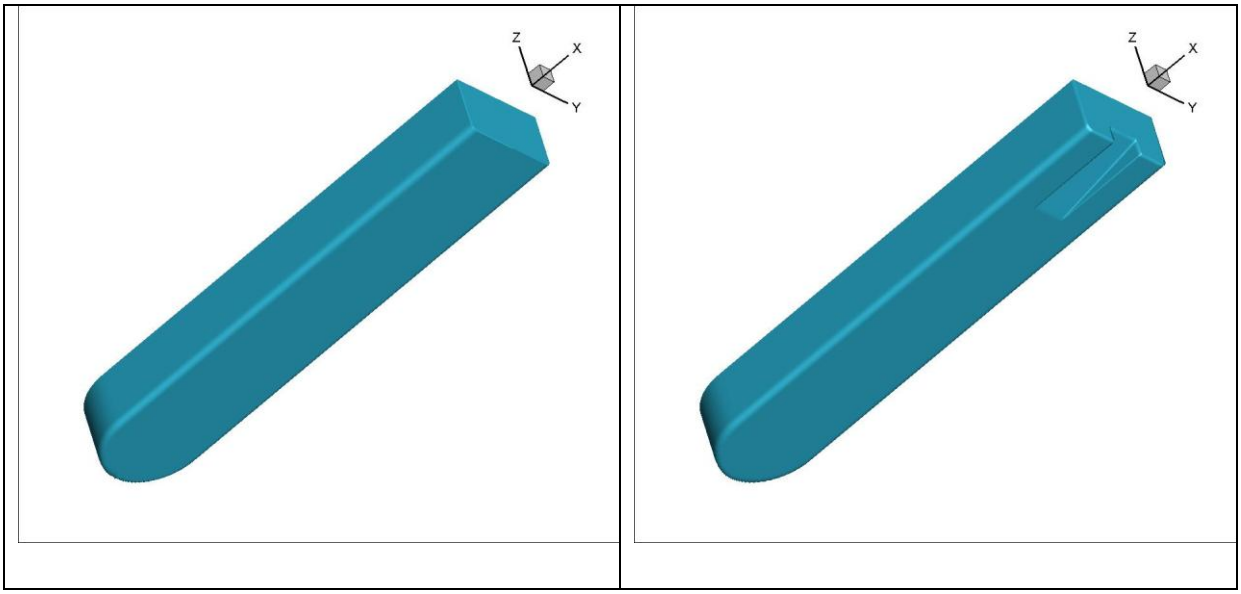

Figure 4.6 Model ship, “Bare Hull” (left) and “Stern Tunnel” (right)

For the study of the verification of total resistance and the comparison of velocity profiles, the bare hull (C_b=0.956) and the hull with stern tunnel (C_b=0.972) are considered for which the experiment was carried out by Matsunaga.

Ship hull forms used in this study are conceived as a typical ULBS (Ultra Large Block coefficient Ship) hull using mathematical formulations. Two ship models are considered. One is called “Bare Hull” hereafter and its waterline at bow is expressed as a semi-ellipse followed by the parallel part which continues to the aft-end. Frame lines are wall-sided with a bilge circle at the bottom. The other is called “Stern Tunnel” which is based on “Bare Hull” and a stern tunnel is attached in the aft part. The width and the depth of a tunnel is 1/3 of breadth *B* and 1/2 of the draft *d*. Tunnel has a wedge-shape with its length of 1/5 of *Lpp*. “Bare Hull” and “Stern Tunnel” shapes are shown in Figure 4.5 and Figure 4.6. The principal particulars are tabulated in Table 4.1.

Table4. 1 Principal Particulars of model ships

	Bare Hull	Stern Tunnel
Breadth (B/L_{pp})	0.2	
Draft (d/L_{pp})	0.067	
Reynolds number Re	8.4×10^5	
Froude number Fr	0.15	
Wetted surface area S/(L_{pp} x L_{pp})	0.318	0.3244
Block coefficient C_b	0.972	0.956
Turbulence Model	EARSM (Explicit Algebraic Reynolds Stress Model) Unsteady	
Flow Solver	SURF(Solution algorithm for Unstructured RANS with FVM)	

In order to compare the computational results, the following non-dimensional form is adopted of total resistance based on the length of ship L_{pp},

$$C_t = \frac{R_T}{1/2\,\rho U^2 L_{PP}{}^2} \tag{4.8}$$

where,

R_t: total resistance (kg)

ρ: density of water (kg.sec^2.m^{-4})

L_{pp}: ship length (m)

U: flow velocity (m.sec^{-1})

The Froude number is set based on the values of length-based F_r which is defined as

$$F_r = \frac{U}{\sqrt{gL_{PP}}} \tag{4.9}$$

Also Reynolds numbers are estimated based on water temperature of the experimental data in order to compare results in the same condition as the experiment.

$$Re = \frac{UL_{PP}}{\nu} \tag{4.10}$$

Experiments were carried out in the circulating water channel (its measuring section is 2.5m (length) x 1.2m (width) x 0.6m (water depth)) of Yokohama National University with ship models of *Lpp*=1.5m. Reynolds number *Re* and Froude number *Fr* of the computations are set to be the same as in the experimental condition, which are *Re* = 8.4 x10^5 and *Fr* = 0.15.

The computational grids are generated using the commercial grid generation software Gridgen (*Pointwise*, Inc.), which creates non-overlapping patched multi-block boundaries. Grids for "Bare Hull" and "Stern Tunnel" are designed to have the same properties as much as possible in order to minimize the effects of grid differences. Computational domain is similar to a quarter of an ellipsoid with $-2 \leq x/Lpp \leq 2.6$, $-2 \leq y/Lpp$ and $-2 \leq z/Lpp \leq 0.05$, while a ship is located $-0.5 \leq x/Lpp \leq 0{:}5$. Only the port side is discretized due to symmetry. Each grid consists of 8 structured grid blocks and a total number of cells are 4,579,328. Figure 4.7 and Figure 4.8 shows the partial views of the computational grids of "Bare Hull" and "Stern Tunnel". Note that the bow grids are identical for both models.

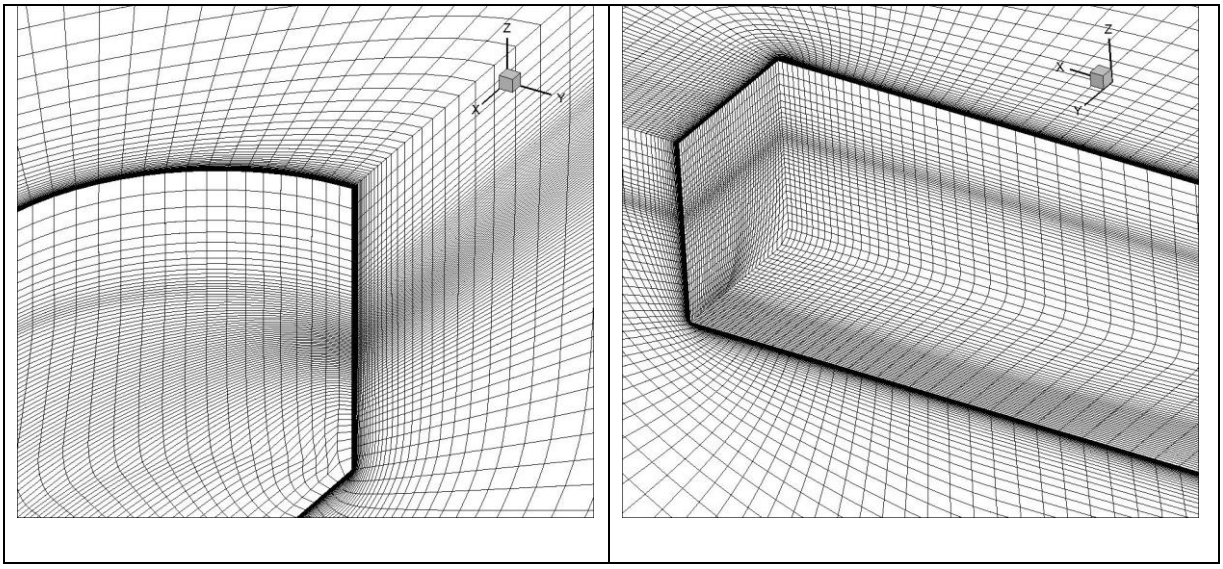

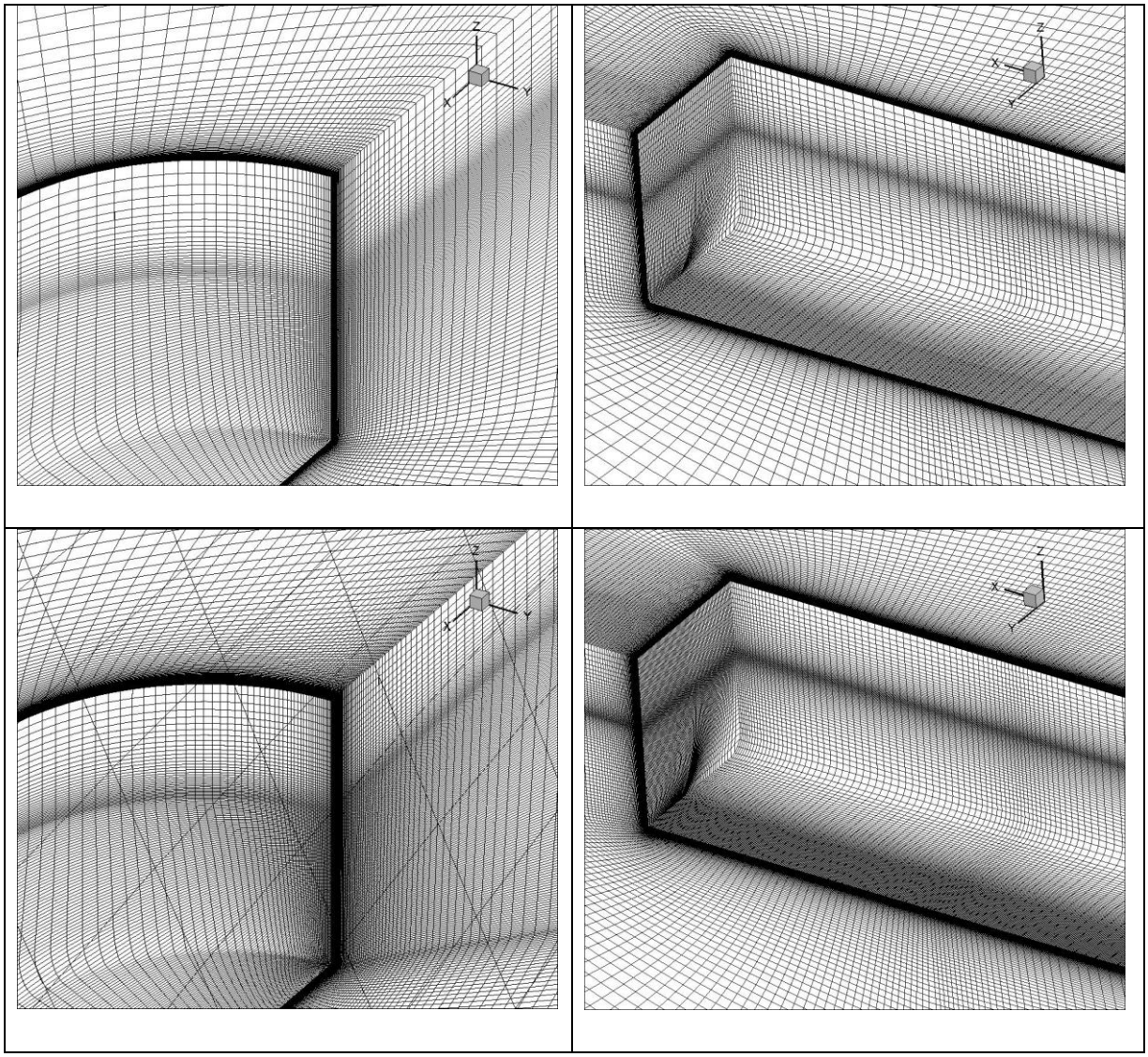

Figure 4. 7 Partial View of unstructured grids around Bare Hull, Bow mesh (Left) and stern mesh (Right), Coarse, Medium, and Fine (From top to bottom).

Computational are performed using the unsteady flow mode of the solver with the dual time stepping and non-dimensional time step *deltat*=0.002 is used for the physical time marching.

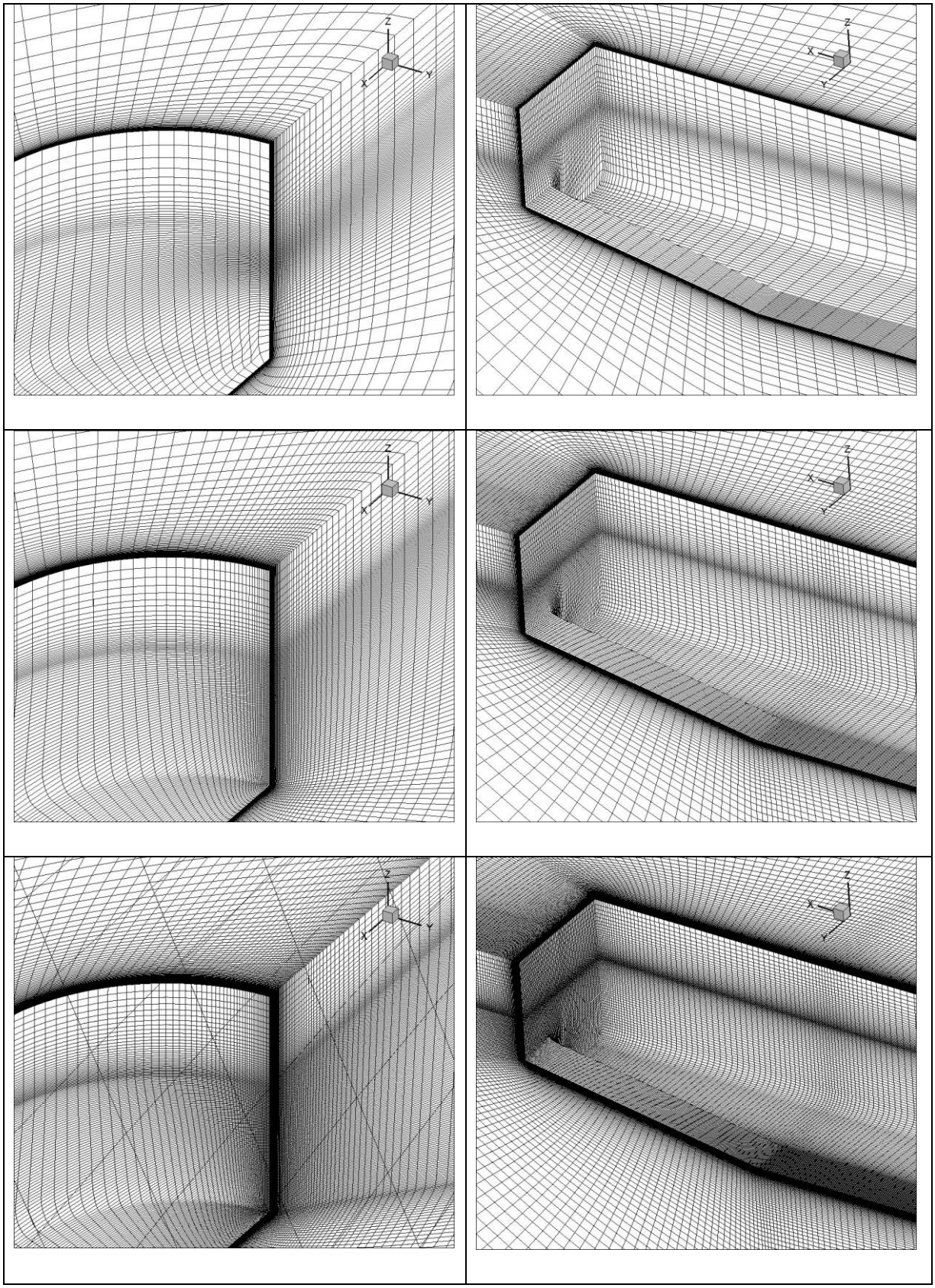

Figure 4. 8 Partial View of unstructured grids around Stern Tunnel, Bow mesh (Left) and stern mesh (Right), Coarse, Medium, and Fine (From top to bottom).

The six boundaries of the computational domain are the following: the inlet boundary: the outlet boundary; the external boundary is a circular or elliptical cylinder with the axis at the water line and $2L_{pp}$ radius; the remaining boundaries are the ship surface, the symmetric plane of the ship and the undisturbed water surface.

The grid is clustered near the ship hull, the free-surface and the symmetry plane. The origin *0* is located at mid-ship on the undisturbed water surface. The *x*-axis is positive towards the stern, the *y*-axis is positive towards the starboard side and the *z*-axis is positive upwards. The ship is moving at constant forward speed in calm water and the hull is held fixed in space. The computation was done in unsteady mode to ensure the stability in solution procedure.

Although the averaged minimum spacing near the ship hull is 1.0×10^{-5} and sufficiently small for resolving the boundary layer on a hull surface. The turbulence model used is EARSM model and flow fields are assumed to be fully turbulent. The computational grid was generated using the commercial code GRIDGEN (*Pointwise*, Inc.), which creates non-overlapping patched multi-block boundaries. Two grids are prepared; one for the bare hull and the other is a hull stern tunnel. Both grids are based on multi-block structured grids covering only the port side of a domain assuming *y*-symmetry.

The computational grids are generated based on the block-structured topology. Firstly the hull with stern tunnel is produced. The bare hull grid was produced by removing the stern tunnel block. The total grid system consists of 8 blocks. The total number of grid points and the total resistance coefficients C_t obtained with the three systematically refined grids of the bare hull and hull with stern tunnel are given in Table 4.8. Note that only the half domain is discretized due to symmetry of geometry. Three grids (Fine, medium and coarse) are used for Fr =0.15 case to help estimating the discretization errors with refinement factor of $\sqrt{2}$. The generated grids are converted to a structured and computed by using SURF.

4.4 Verification of Numerical Results

In order to verify the computational method against experimental results, the uncertainty related to the computational method is estimated. The grid uncertainty, U_G, for the total resistance coefficient $C_t = \frac{R_T}{1/2\,\rho U^2 L_{PP}{}^2}$ where R_t is the total resistance is estimated using three systematically refined grids. The procedures estimated based on three symmetrically refined grids. The procedure is in accordance with the Recommendation of ITTC [11), 12)] as in Box Ship.

The computed results of time-averaged resistance values of C_t using three grids are shown in Table 4.2 and resulting grid uncertainty is shown in Table 4.3.

The grid refinement ratio used for the grid convergence is $r_G = \sqrt{2}$ as stated early. Thus, the cell numbers are 4,579,328 for the fine grids shown in Figure 4.7 and Figure 4.8, and 1,642,004 for the medium grids and 572,416 for the coarse grids. For the bare hull, R_G is estimated to 0.166 which shows the monotonic convergence, while R_G=-0.134 in the stern tunnel case shows the oscillatory convergence.

Table4. 2 Grid convergence study of total resistance C_t (x10^{-3}) for Stern Tunnel, *Fr*=0.15

		Coarse S_3	Medium S_2	Fine S_1	Experiment
	Cell No.	572,416	1,642,004	4,579,328	-
Bare Hull	C_t	5.5863	5.2069	5.1455	5.93
	ε		-6.84%	-1.17%	
Stern Tunnel	C_t	5.7226	5.4782	5.5109	5.87
	ε		-4.27%	0.60%	

% of finer grid value

Table4. 3 Verification of total resistance C_t for two model ship, Fr =0.15

Ship	R_G	P_G	C_G	U_G %S_1	δ_G^* %S_1	U_{G_C} %S_1	S_C 10^{-3}
Bare hull	0.166	5.18	5.01	2.20	1.25	0.997	5.08
Tunnel	-0.134	-	-	2.22	-	-	5.54

Table4. 4 Validation of total resistance C_t for two model ship, Fr =0.15

Ship		$E\%$=(D-S)x100/D
C_t	Bare hull	13.0
	Stern Tunnel	6.12

In case of the stern tunnel, the grid uncertainty U_G is estimated as 2.22% of S_1 (the fine grid solution). In case of the Bare Hull, the further analysis is possible as shown in Table 3, and the grid uncertainty is estimated as 2.25% of S_1. Since the correction factor is 5.01 and away from unity, only the grid uncertainty U_G is estimated. In Table 3, the corrected grid uncertainty and related quantities are also shown for reference.

Although the uncertainty levels are reasonably low, *Ct* of "Stern Tunnel" is larger than "Bare Hull" and this trend is opposite to that of the measurement shown in Table 4.2. Although the uncertainty levels are reasonably low for both cases, *Ct* of "Stern Tunnel" is larger than "Bare Hull" and this trend is opposite to that of the measurement shown in Table 2. In the experiment, the models with 1.5m *Lpp* are used in the circulating water channel at Yokohama National University. The resistance is measured with the load cell with the capacity of 20 N and its accuracy is given as 0.2% of full scale. Since the uncertainty of the measurement is not available, the validation of the results is not performed.

The validation of total resistance C_t for two model ship is shown in Table 4.4. In order to conduct the validation, the experimental uncertainty U_D is required. However, since U_D is not available for the present case, only the comparison errors are estimated as 13.0%*D* for Bare Hull and 6.12 %*D* for Stern Tunnel.

4.5 Comparison of total resistance coefficients

Table4. 5 Computed resistance components (x10^{-3}, L_{pp}^2 - base)

Ship	Total resistance coefficient C_t	Pressure resistance coefficient C_p	Frictional resistance coefficient C_f
Bare Hull	5.14	4.22	0.93
Stern Tunnel	5.51	4.56	0.95

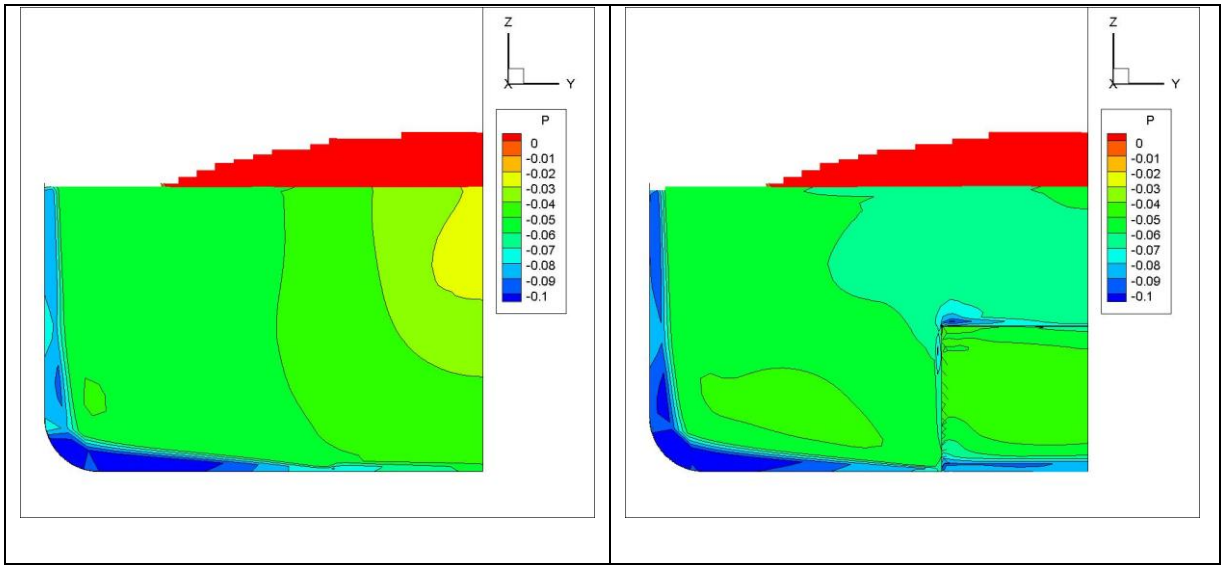

Figure 4. 9 Computed hull surface pressure distributions at the stern, “Bare Hull” (left) and “Stern Tunnel” (right).

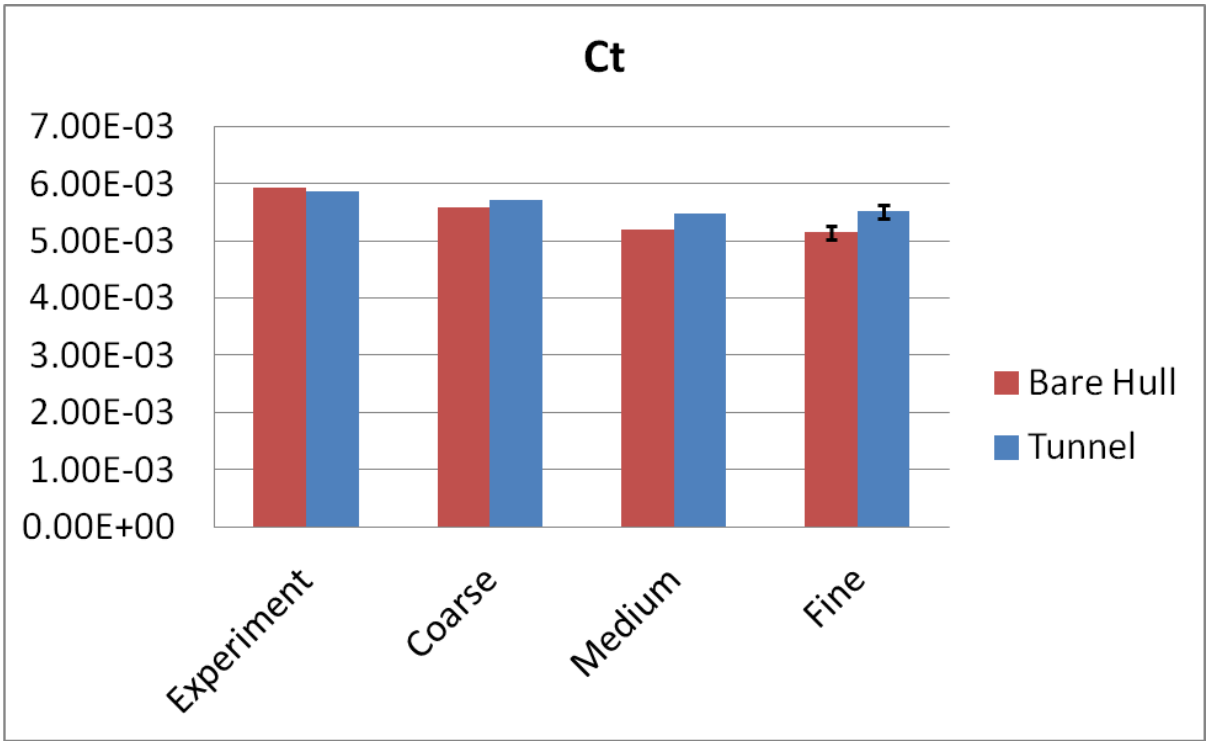

Figure 4. 10 Comparison of total resistance coefficients between CFD and experimental results for Bare Hull and Stern Tunnel.

Figure 4.10 shows the comparison of total resistance coefficient between CFD and experiment results. In experiment, the total resistance coefficient of stern tunnel is smaller than the bare hull, but in computational cases, the total resistance of the stern tunnel is higher than bare hull. In computational case, the stern tunnel cannot reduce total resistance coefficient as in Experiment. It may be related to modeling uncertainty associated with turbulence modeling or insufficient grid numbers. From a quantitative point of view the calculated resistance is under-predicted with 13% (average of all speeds) in Bare Hull and under-predicted with 6.12% in Stern Tunnel which is the same tendency of the comparison errors above. However, the tendency of the slope of the resistance curves is well reproduced by the computations. The error bars show the grid uncertainty of 2.25% in bare hull cases and 1.06% in stern tunnel cases.

The computed resistance components are shown in Table 4.5. The main difference comes from pressure resistance. Increase of pressure resistance in “Stern Tunnel” can be verified by the hull surface pressure distributions in the stern shown in Figure 4.9, since the

fore part of the hulls are identical for both hulls. With the presence of a stern tunnel, flow inside the tunnel is accelerated as discussed in the following section and thus pressure decreases. Thus, the relatively higher pressure zone near the center on “Bare Hull” disappears in “Stern Tunnel”. Thus, larger resistance in “Stern Tunnel” seems to be consistent with flow fields. A possible reason for this opposite prediction of resistance trend is numerical modeling errors of the current turbulence models for massively separated flows. Further investigations are required both in simulations and measurements to clarify the reasons of this discrepancy.

Chapter 5

Visualization of Flow Field around ULBS

5.1 Effect of turbulence model

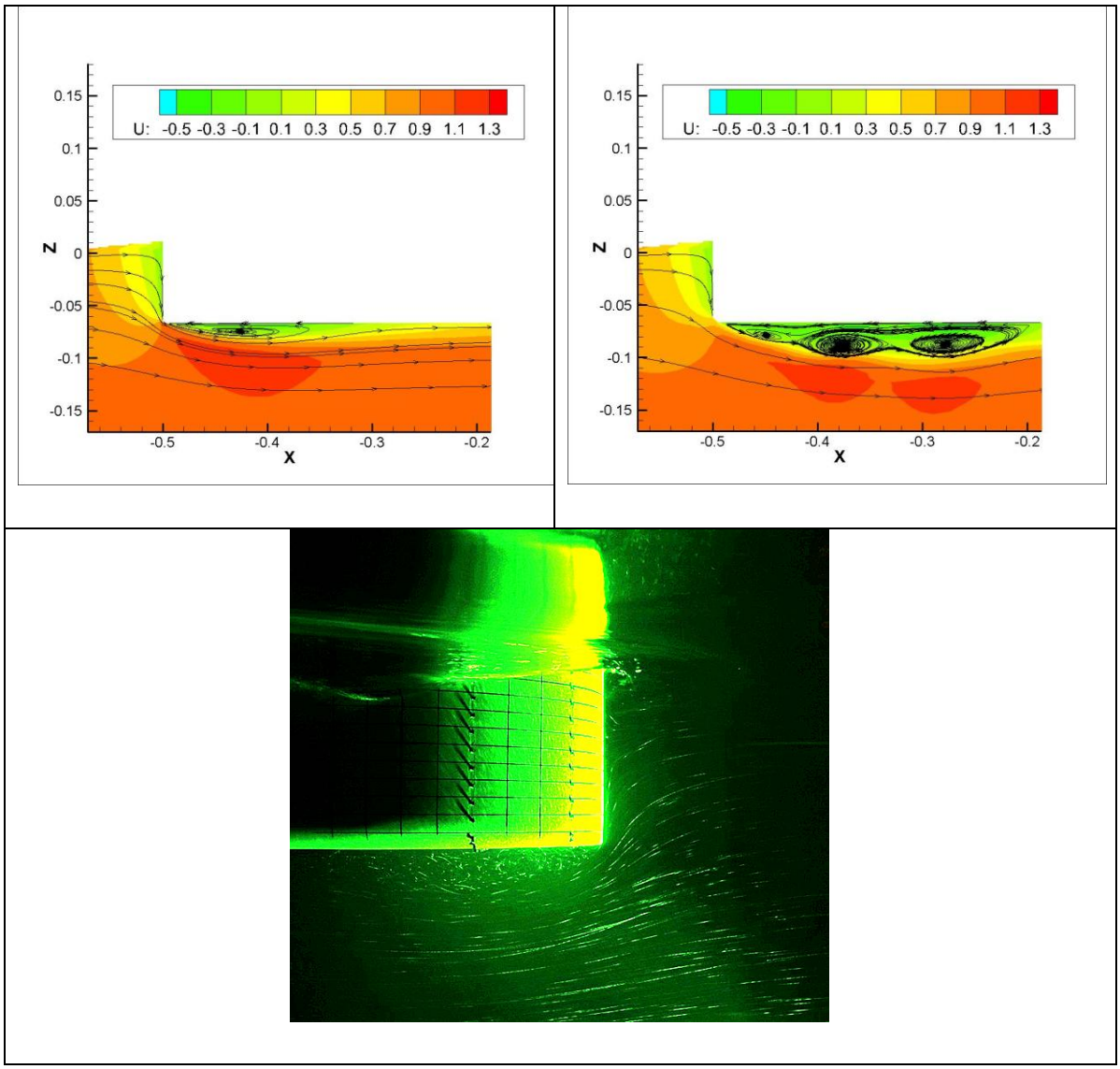

Figure 5. 1 Streamlines with *u* velocity contours around the bow bottom on the vertical center plane: *k* -ω SST (top left), EARSM (top right) and visualization in the experiment (bottom).

In order to examine the effect of turbulence models on flow fields, comparison are made between the results with EARSM and the conventional eddy viscosity model (k-ω SST model11)). Figure 5.1 shows the streamlines with contours of u (velocity in x-direction) on the center plane around the bow bottom together with the visualization of the flow field in the experiment. In $k-\omega$ case, only one vortex is observed under the bottom, while in EARSM case multiple vortexes with small scale are captured, which is closer to the visualization result in the experiment. It is evident that EARSM turbulence model can reproduce detailed flow features compared with the $k-\omega$ SST model. Therefore EARSM model will be used in this study with the anticipation that separated flows in stern regions can be predicted better.

5.2 Isosurfaces of second invariant of the velocity gradient, Q

The Q-criterion [14)] is used to identify the coherent vortical structures. The rate of strain tensor S_{ij} and the vorticity tensors W_{ij} are defined as

$$S_{ij} = \left[\left(\partial u_i / \partial x_j\right) + \left(\partial u_j / \partial x_i\right)\right] / 2 \tag{5.1}$$

$$W_{ij} = \left[\left(\partial u_i / \partial x_j\right) - \left(\partial u_j / \partial x_i\right)\right] / 2 \tag{5.2}$$

The 2nd-invariant of the rate of deformation tensor Q is defined by Equations 5.1 and 5.2 as

$$Q = \frac{1}{2}\left(\left|W_{ij}\right|^2 - \left|S_{ij}\right|^2\right) \tag{5.3}$$

If Q is positive, the Euclidean norm of vorticity tensor dominates the rate of strain which evidences the rotation of the flow. It has been found that technique of isosurfaces of second invariant of velocity gradient tensor Q defined in Equations 5.3 is superior for identifying coherent structures to the technique of isosurface of vorticity. If Q is positive, the Euclidean norm of vorticity tensor dominates the rate of strain which evidences the rotation of the flow.

The isosurface vorticity of Q=5 which are coloured with velocity magnitudes are shown in the following figures. And streamlines are used to visualize separations and re-attachments around the bow and behind the stern.

5.3 Flow field around the bow

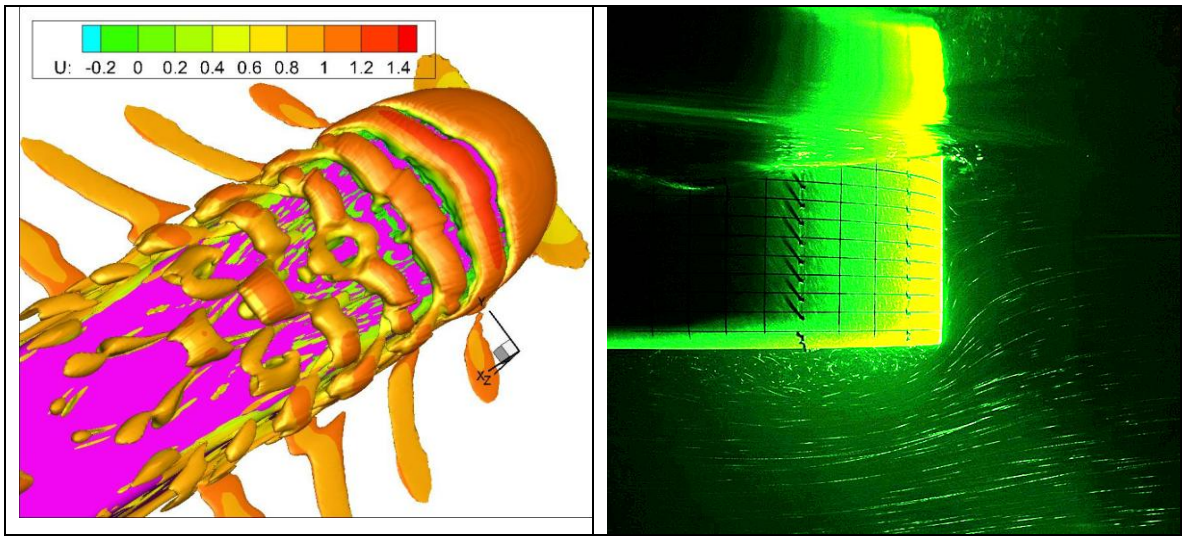

Figure 5. 2 Isosurfaces of second invariant of velocity gradient tensor Q=5 with velocity contour around the bow (Bottom view) (Left), and Flow field the bow at the center plane (Experiment) (Right).

Figure 5.2 shows the magnified view of the bow part of “Stern Tunnel”, where a series of vortex structures shedding from the bow are observed and this is consistent with streamlines shown in Experiment. This feature in the bow is common between two hulls because of the same grid of the block of bow. The separation near the bottom of the bow is followed by the boundary layer evolution.

5.4 Flow field overview around the hull

Figure 5.3 shows the bottom views of the vortical flow fields for “Bare Hull” and “Stern Tunnel”. In the plot, iso-surfaces of the second invariant of the velocity gradient Q = 5 are shown. The flow fields around the bow of “Bare Hull” and “Stern Tunnel” are essentially identical because of the same geometry of the fore part. Small discrepancies come from the fact that flows are unsteady and fluctuating slightly.

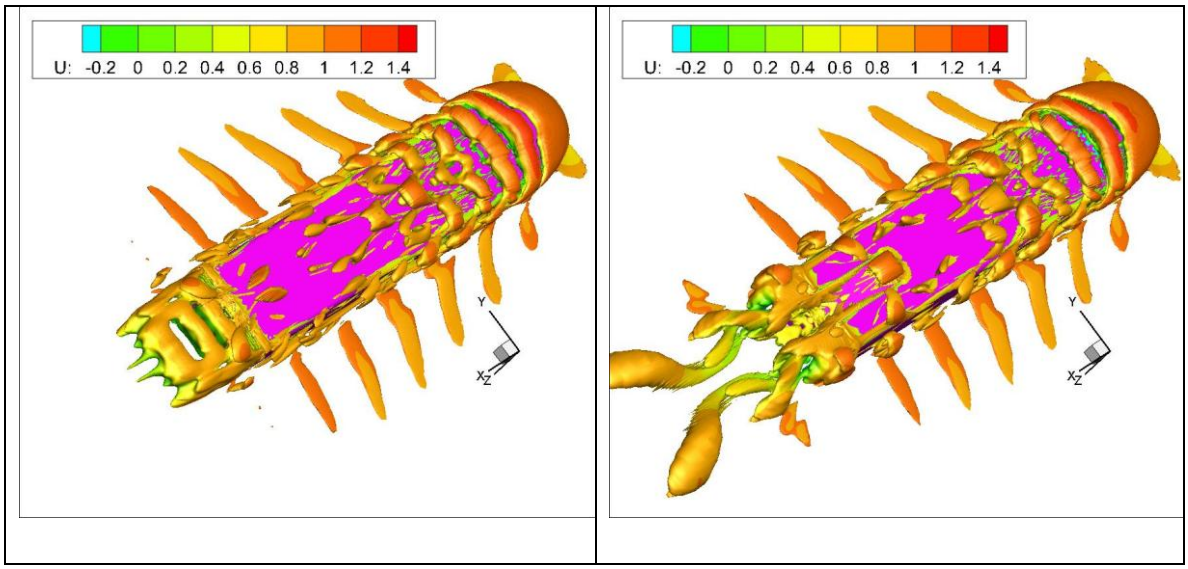

Figure 5. 3 Overview of Isosurfaces of second variant of velocity Q=5 with velocity contour around the hull, “Bare Hull” (Left) and “Stern Tunnel” (Right).

Figure 5.4 shows u, velocity distributions in the x- directions at the center plane near the bottom of the bow and the end of the stern. A series of vortexes occurs near the bottom of the bow after passing through the corner of the bow. The velocity distributions in the bottom of “Bare Hull” and “Stern Tunnel” show similar tendency because of the same block of the bow, and the separation on the bottom of the bow is followed by the boundary layer evolution. The separations occur after passing the bluff body of the stern. The separation near the stern end is stronger in the “Bare Hull” case than “Stern Tunnel” case. It seems the separation near the stern end depends on the shape of the stern, and the presence of “Stern Tunnel” can reduce the flow separations.

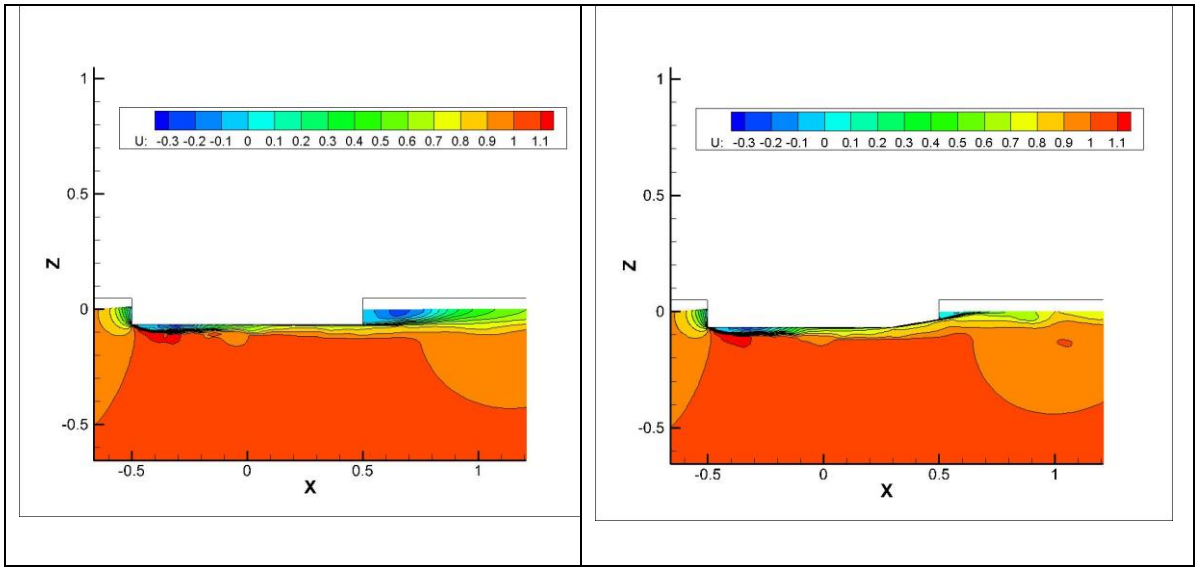

Figure 5. 4 Overview of velocity contour around the hull, "Bare Hull" (Left) and "Stern Tunnel" (Right).

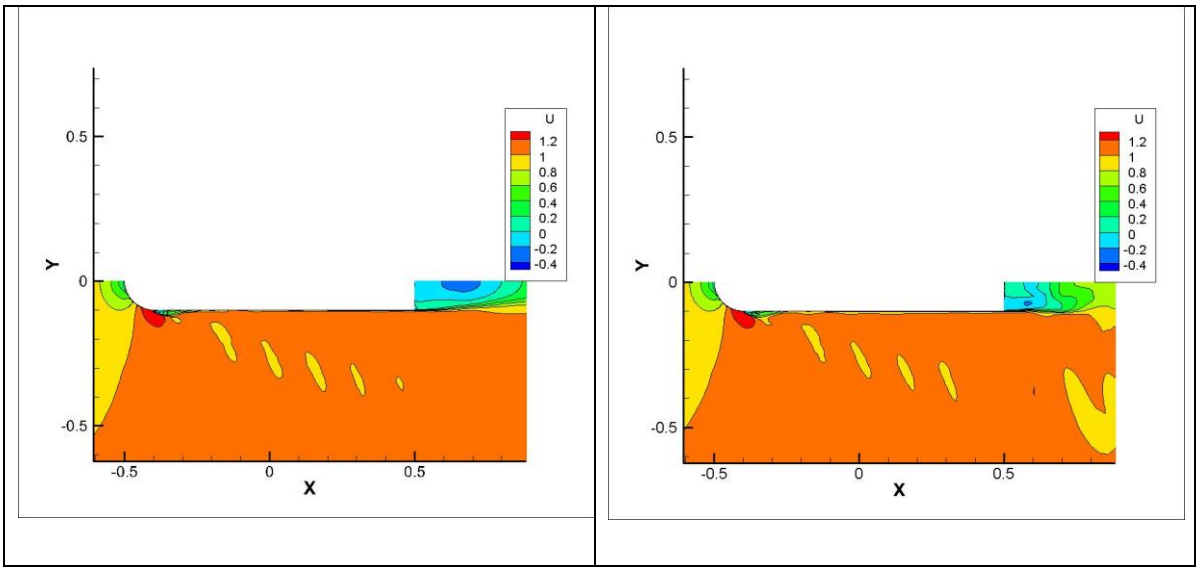

Figure 5. 5 Velocity distributions on the free surface of ULBS, "Bare Hull" (Left) and "Stern Tunnel" (Right).

Figure 5.5 illustrates the velocity distributions, *u*, on the free surface. After passing through the bow, the velocity becomes higher because of the smooth flow around the curve shape of the bow. After passing through the bluff body of the stern the velocity becomes drops and a central recirculation region occurs at the center plane of the bare hull. In "Stern Tunnel" cases, a corner recirculation region occurs behind the end corner of "Stern Tunnel".

5.5 Flow structures behind the stern

Figure 5.6 shows iso-surfaces of second variant of velocity *Q*=5 with velocity contour around the stern. The flow fields in the stern show significant differences between two hulls and “Stern Tunnel” hull generates more complicated flows than “Bare Hull”. Stern of “Bare Hull” has a simple shape with continuing parallel part and the vortices shed at the edges of the stern. On the other hand, in case of “Stern Tunnel”, vortices are generated on the walls of the tunnel in addition to the stern edges of the hull.

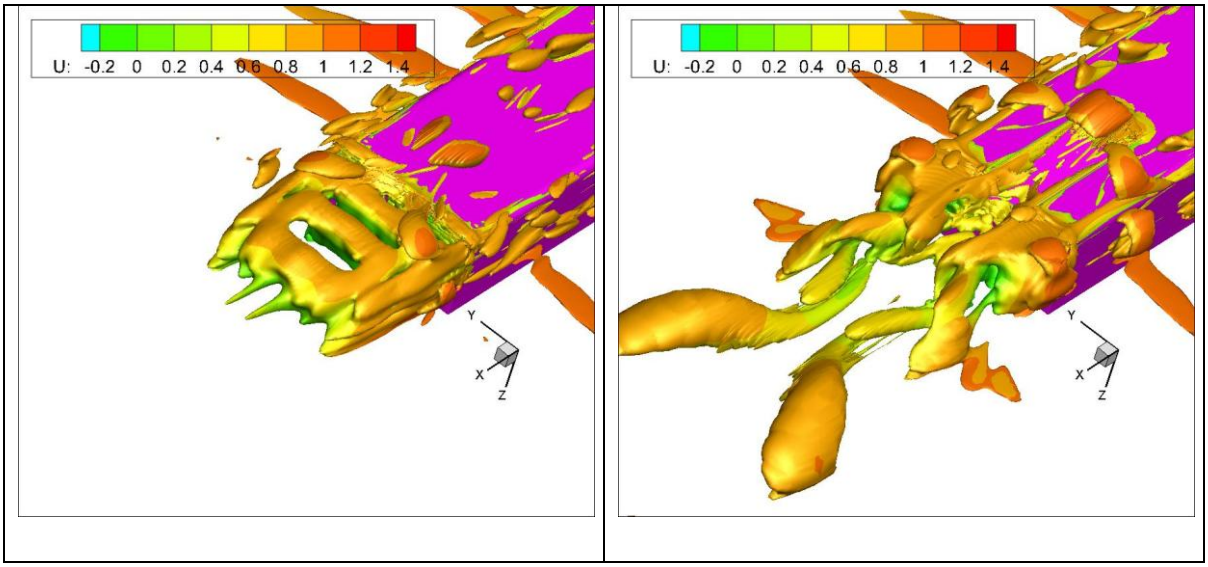

Figure 5. 6 Isosurfaces of second variant of velocity *Q*=5 with velocity contour around the stern (From bottom view), “Bare Hull” (Left) and “Stern Tunnel” (Right).

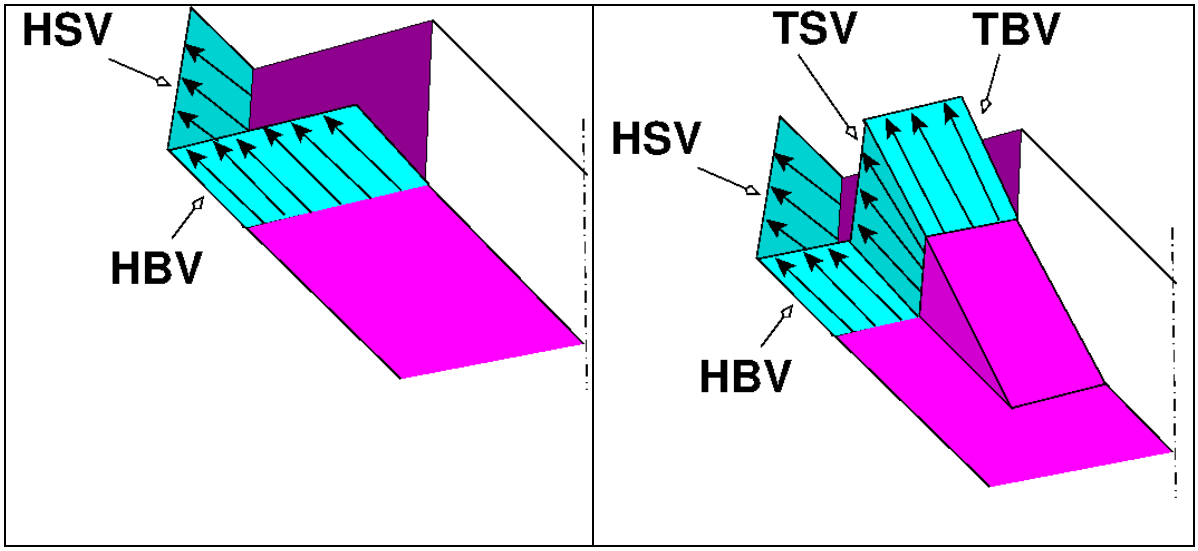

Figure 5. 7 Sketches of the flow structures behind the stern, “Bare Hull” (Left) and “Stern Tunnel” (Right).

Sketches of the flow structures behind the stern are shown in Figure 5.7. The following terms are defined to discuss the flow structures behind the stern:

HSV	Vortex generated at the side
(Hull Side Vortex)	edge of a main hull
HBV	Vortex generated at the bottom
(Hull Bottom Vortex)	edge of a main hull
TSV	Vortex generated at the side
(Tunnel Side Vortex)	edge of a tunnel
TBV	Vortex generated at the bottom
(Tunnel Bottom Vortex)	edge of a tunnel

In case of “Bare Hull”, two vortex structures, HSV and HBV, are dominant, while four structures, HSV, HBV, TSV and TBV, are present in “Stern Tunnel” and flow field becomes more complicated.

Figure 5.8 depicts the iso-surfaces of the vorticity magnitude =20 behind the stern. In "Bare Hull" case, it is visible that the vortex comes from the side of the transom stern (HSV) and the vortex comes from the bottom of transom stern (HBV). In "Stern Tunnel" case, the side vortex comes from main transom stern (HSV) and the vortex comes from the bottom of stern tunnel part (TBV) followed long vortex further downstream are visible. The intensity of vortex in "Bare Hull" HSV is higher than that of "Stern Tunnel". These iso-surfaces show the basic structures sketched in Figure 5.7, although (HBV) in "Stern Tunnel" is behind the (TSV) and can hardly be seen.

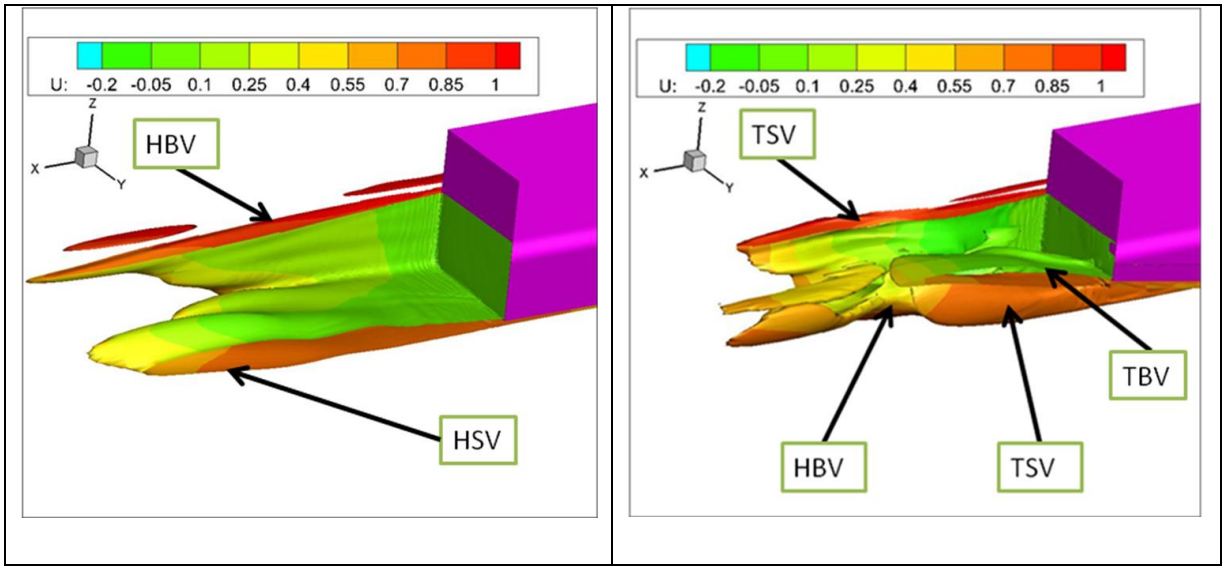

Figure 5. 8 Overview of Iso-surfaces of second variant of velocity *Q*=5 with velocity contour behind the stern from the top view, "Bare Hull" (Left) and "Stern Tunnel" (Right).

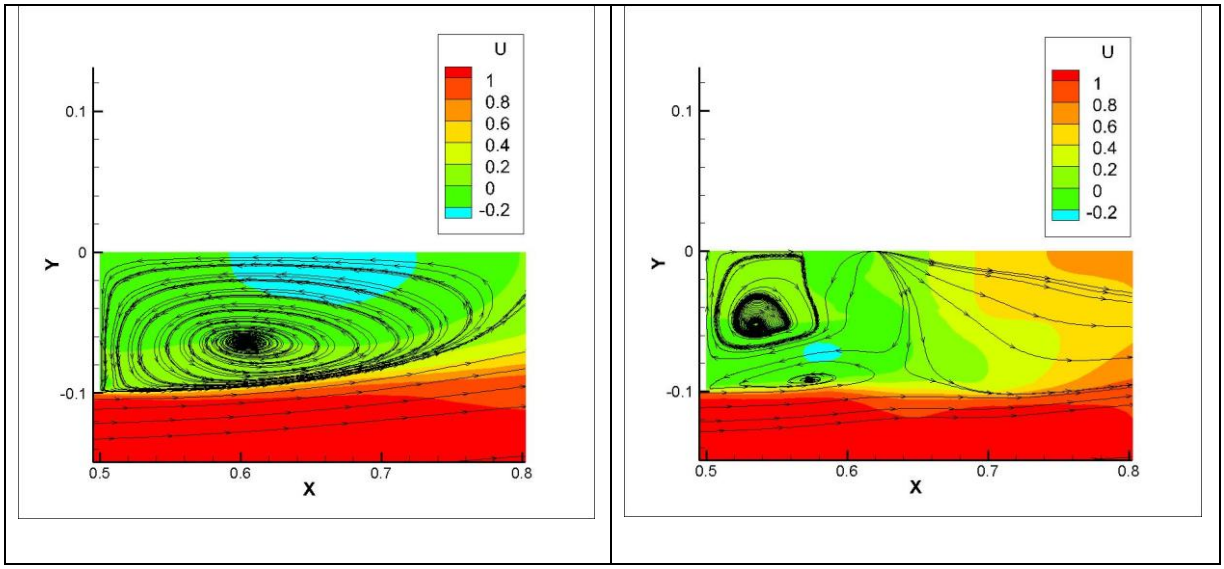

Figure 5. 9 Velocity distributions and streamline behind the stern on the free surface. "Bare Hull" (Left) and "Stern Tunnel" (Right)

Figure 5.9 shows velocity distributions and streamline behind the stern on the free surface. After passing through the bluff body of the stern the velocity becomes drops and the vortexes occur in accordance with the low velocity region which shows the recirculation. In "Bare Hull" case, vortex occurs behind the transom stern in accordance with the velocity region in Figure 5.10. In "Stern Tunnel" case, the figure illustrates clearly the mean flow structure, being characterized by corner vortex comes from main transom stern and a series of vortexes come from the stern tunnel part. Again the re-circulation region of "Bare Hull" is larger than "Stern Tunnel". One big swirling flow with counter-clockwise rotation is observed in "Bare Hull", while two main vortices are present in "Stern Tunnel". One in the outside is in the same direction with "Bare Hull" and these are related to HSV. The other vortex inside is in the opposite rotation and related to TSV.

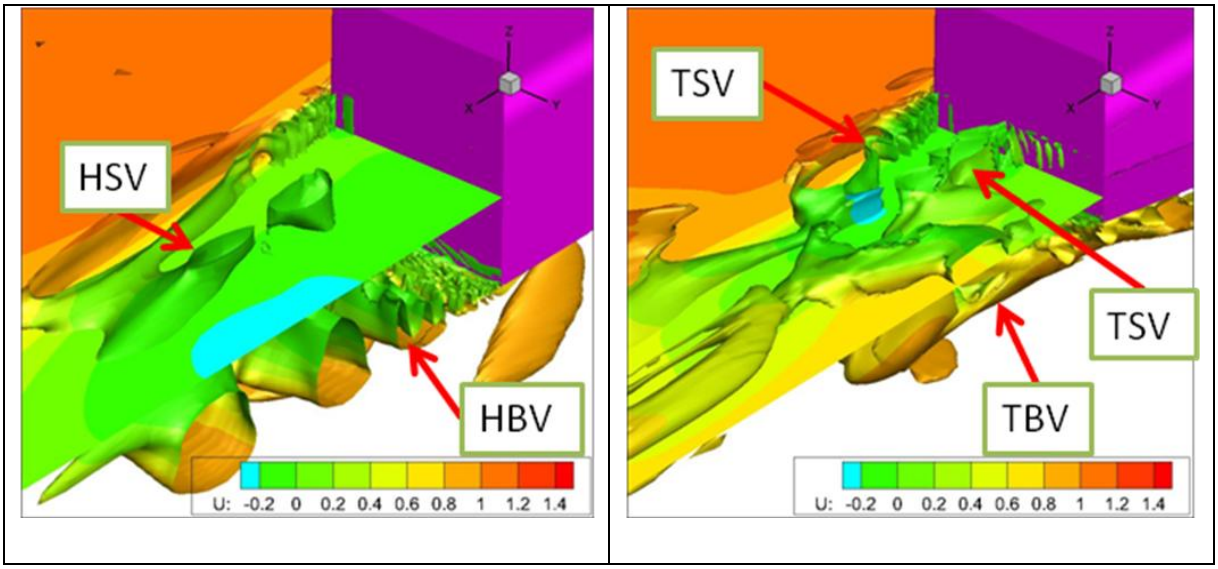

Figure 5. 10 Iso-surfaces of second variant of velocity Q=5 with velocity contour on the free surface z/L=-0.02, "Bare Hull" (Left) "Stern Tunnel" (Right).

Figure 5.10 shows iso-surfaces of second variant of velocity Q=5 with velocity contour on the free surface z/L=-0.02, "Bare Hull" (Left) "Stern Tunnel" (Right). After passing through the bluff body of the stern, the velocity becomes drops and the vortex occurs in accordance with the low velocity region which shows the recirculation. In comparison with the "Bare Hull" case, the low velocity region and intensity of vortex in "Stern Tunnel" case is smaller than that of the "Bare Hull". A very long vortex structures were observed in the wake region of the "Stern Tunnel" case, and it seems come from the end of tunnel parts, as shown in Figure 5.11. It is observed that a series of vortices comes from the bottom edge of the stern in "Bare Hull" case (HBV), and vortices with weaker intensity come from the bottom of stern tunnel in "Stern Tunnel" case (TBV). Also the vortices from the side of the hulls (HSV) are larger in "Bare Hull" than in "Stern Tunnel".

Figure 5.11 shows iso-surfaces of second variant of velocity Q=5 with velocity contour behind the stern from the bottom view, "Bare Hull" (Left) and "Stern tunnel" (Right). In "Bare Hull" case, it is visible that the vortex comes from the side of the transom stern (HSV) and the vortex comes from the bottom of transom stern (HBV). In "Stern Tunnel" case, the side vortex comes from main transom stern (TSV) and the vortex comes from the bottom of stern tunnel part (TBV) followed long vortex further downstream are visible. The intensity of vortex in "Bare Hull" HSV is higher than that of the "Stern Tunnel" (TSV).

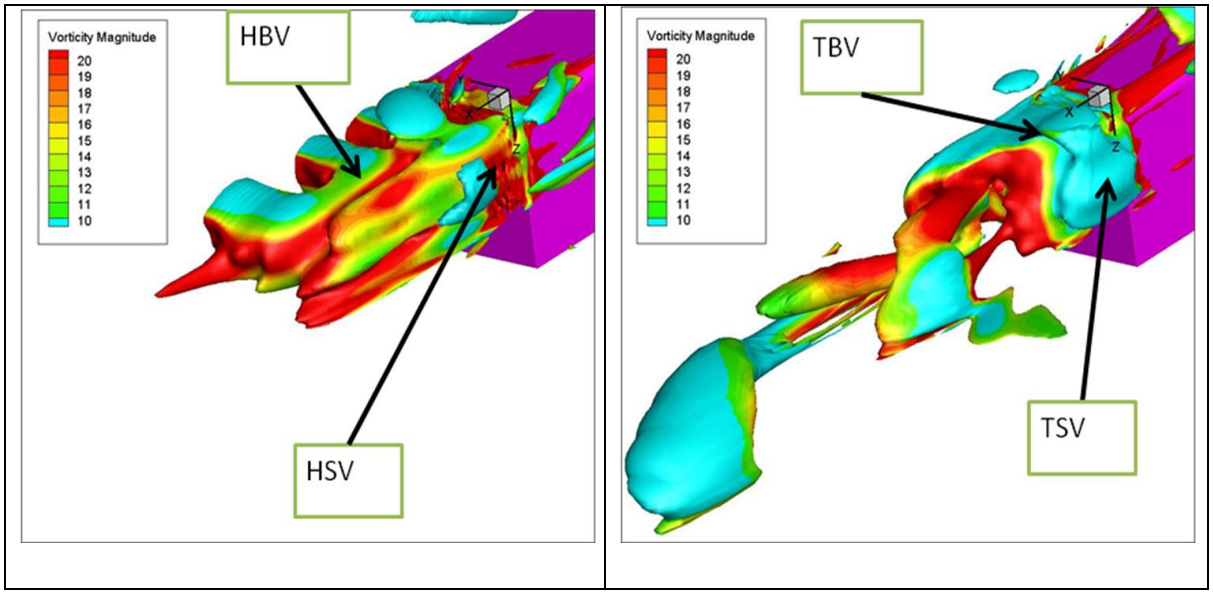

Figure 5. 11 Overview of Iso-surfaces of second variant of velocity *Q*=5 with velocity contour behind the stern from the bottom view, “Bare Hull” (Left) “Stern Tunnel” (Right).

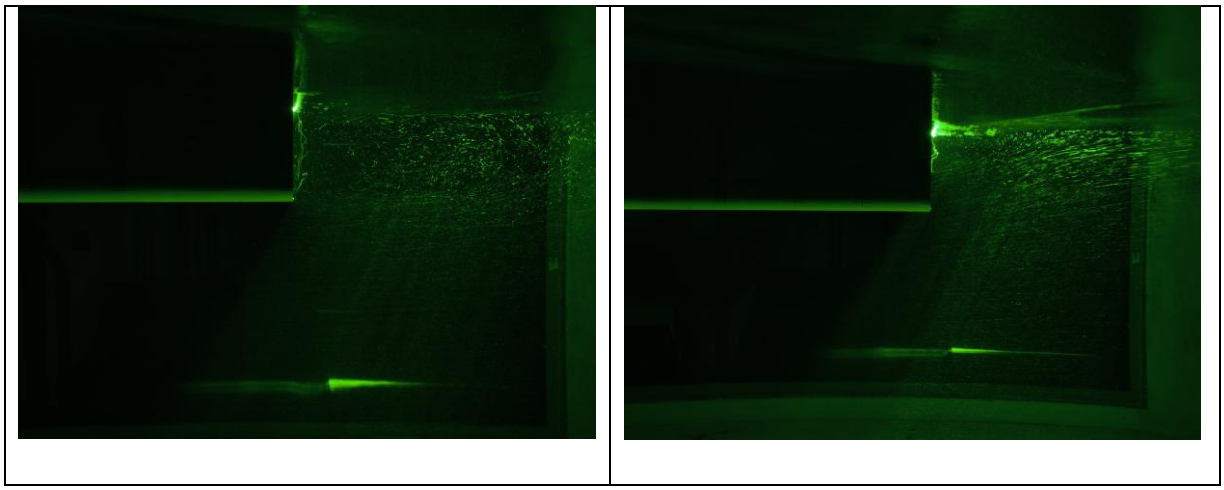

Figure 5.12 Flow field behind the stern (Experiment), “Bare Hull” (Left) “Stern Tunnel” (Right).

Figure 5.12 shows flow field behind the stern at the vertical center plane (Experiment), “Bare Hull” (Left) and “Stern Tunnel” (Right). In “Bare Hull” case, a large central vortex occurs behind the transom stern. In “Stern Tunnel” case, the flow goes up along the stern tunnel part and a weaker vortex occurs.

Figure 5.13 shows velocity distributions and streamline behind the stern at the vertical center plane y/L_{PP}=0.5, “Bare Hull” (Left) and “Stern Tunnel” (Right). The re-circulation region in “Bare Hull” is much larger than in “Stern Tunnel”. The multiple swirling can be observed in “Bare Hull” and this is related to the series of iso-surfaces of Q in HBV region in Figure 5.10. Flow directions behind the stern are close to horizontal in “Bare Hull” and upward in “Stern Tunnel” as expected. In “Bare Hull” case, two vortexes occur behind the bluff body of the stern. The node point in the shear layer of the vortex region behind the stern is also visible. In “Stern Tunnel” case, the flow goes up along the stern tunnel part and only one vortex occurs after passing through the bottom of the stern tunnel. In comparing with “Stern Tunnel” case, the vortexes moves further downstream in “Bare Hull” case. The region of lower velocity behind the stern end is clear in “Bare Hull” cases than in “Stern Tunnel” cases, and it is in accordance with the experimental data in Figure 5.12. It is obvious that the separation becomes weaker in “Stern Tunnel” cases than in “Bare Hull” cases.

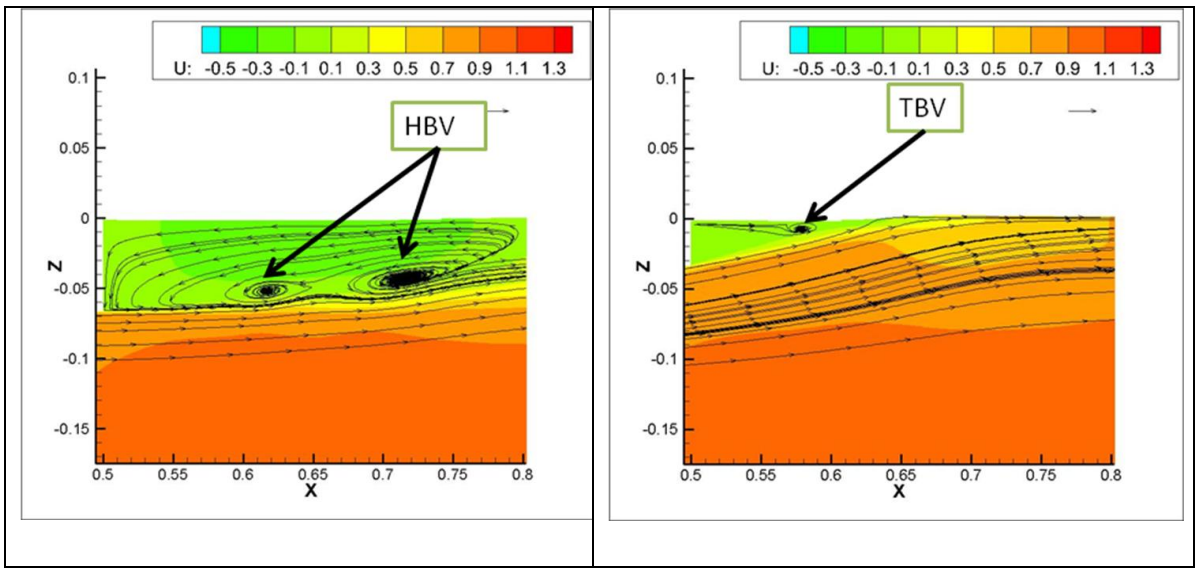

Figure 5.13 Velocity distributions and streamline behind the stern at the vertical center plane, “Bare Hull” (Left) “Stern Tunnel” (Right).

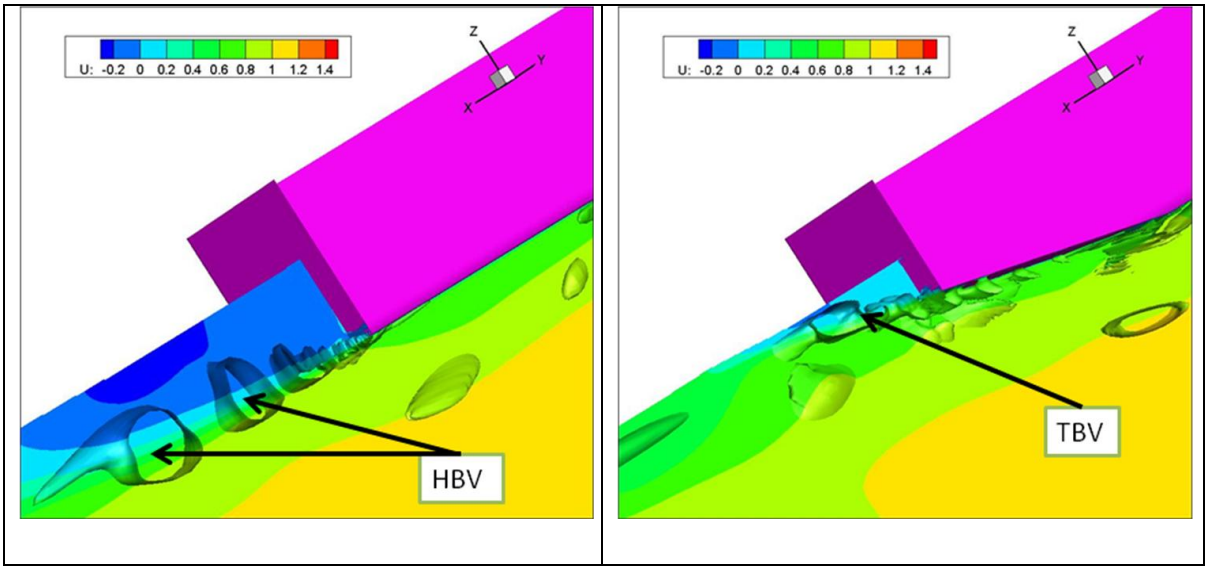

Figure 5. 14 Iso-surfaces of second invariant of the velocity gradient Q=5 colored with velocity contour at the center plane y=-0.02, "Bare Hull" (Left) "Stern Tunnel" (Right).

Figure 5.14 shows iso-surface of second invariant of the velocity gradient tensor Q=5 colored with velocity contour at the section plane y=-0.02. It is observed that a series of vortexes comes from the bottom of the transom stern in "Bare Hull" case (HBV), and weaker intensity of vortexes come from the bottom of stern tunnel part in "Stern Tunnel" case (TBV). The vortexes in both cases are in accordance with the streamlines in Figure 5.13.

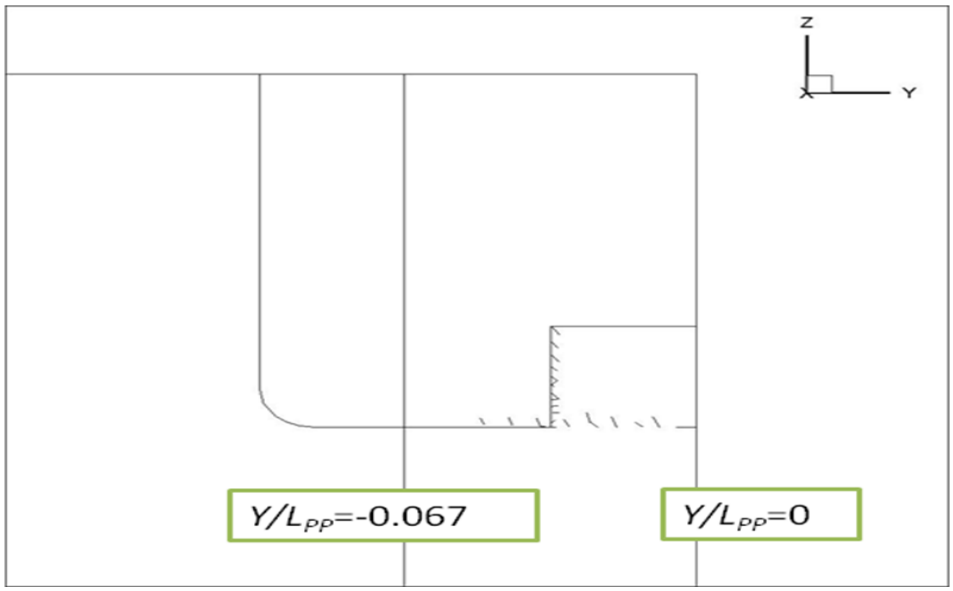

Figure 5.15 The vertical center plane y/L_{PP}=0 & y/L_{PP}=-0.067 behind the stern.

Figure 5.15 shows the position where the iso-surfaces of Q and intensity of velocity measured. Y/L_{PP}=0 is the center plane which is behind where the shape of the stern tunnel occurs. On the other hand, y/L_{PP}=-0.067 which corresponds to the middle of a half span of the main hull beside the stern tunnel.

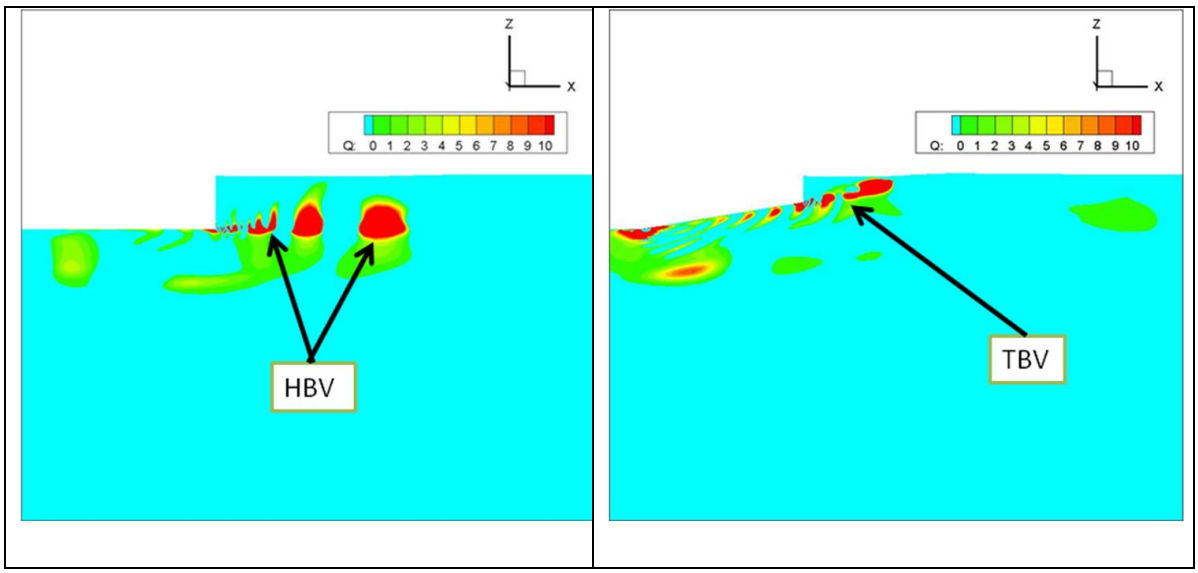

Figure 5. 16 Iso-surfaces of second invariant of the velocity gradient at the center plane y/L_{PP}=0, “Bare Hull” (Left) “Stern Tunnel” (Right).

Figure 5.16 illustrates iso-surfaces of second invariant of the velocity gradient at the center plane y/L_{PP}=0, “Bare Hull” (Left) and “Stern Tunnel” (Right). In “Bare Hull” case, a series of stronger vortexes (HBV) comes from the bottom of the main transom stern. In “Stern Tunnel” case, it is evident that the flow goes up along the stern tunnel part and a series of weaker vortexes (TBV) comes from the stern tunnel part. Figure 5.17 shows iso-surfaces of vorticity magnitude distribution at the center plane y/Lpp = 0. On the center plane, vorticity develops horizontally from the bottom edge of the stern in case of “Bare Hull” (HBV), while vorticity goes up with the same angle of the tunnel bottom in “Stern Tunnel” case (TBV). Also, the high vorticity region of HBV in “Bare Hull” is larger than TBV in “Stern Tunnel”, which shows separation behind the stern of “Bare Hull” is stronger than that of “Stern Tunnel”. It is clear that the intensity of (TBV) is weaker than (HBV) in accordance with the intensity of vortexes in Figure 5.16.

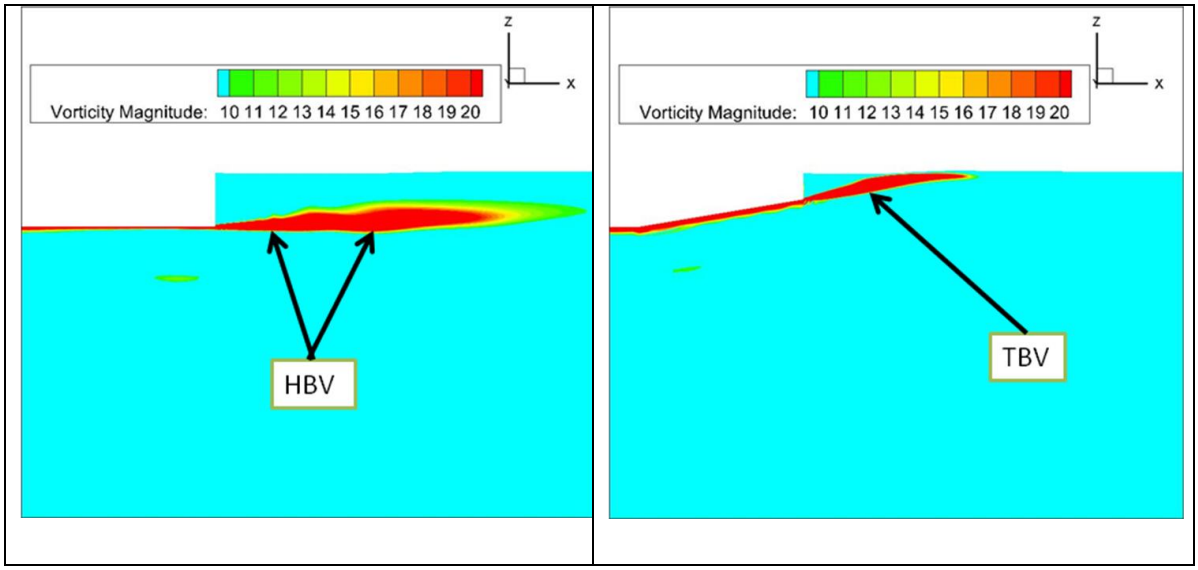

Figure 5.17 Iso-surfaces of vorticity magnitude at the center plane y/L_{PP}=0, "Bare Hull" (Left) "Stern Tunnel" (Right).

Similarly Figure 5.18 illustrates iso-surfaces of second invariant of the velocity gradient at the center plane, y/L_{PP}=-0.067 which corresponds to the middle of a half span of the main hull beside the stern tunnel, "Bare Hull" (Left) and "Stern Tunnel" (Right). In "Bare Hull" case, a series of vortexes (HBV) comes from the bottom of the main transom stern. In "Stern Tunnel" case, a series of vortexes (HBV) comes from the main transom stern. Figure 5.19 shows iso-surfaces of vorticity magnitude distributions on the section of y/Lpp = -0.067. On that plane, vorticity develops horizontally in both cases, since these vortices can be considered to be HBV. Again, the intensity of the vorticity is larger in "Bare Hull" than "Stern Tunnel" in accordance with the intensity of vortexes in Figure 5.19.

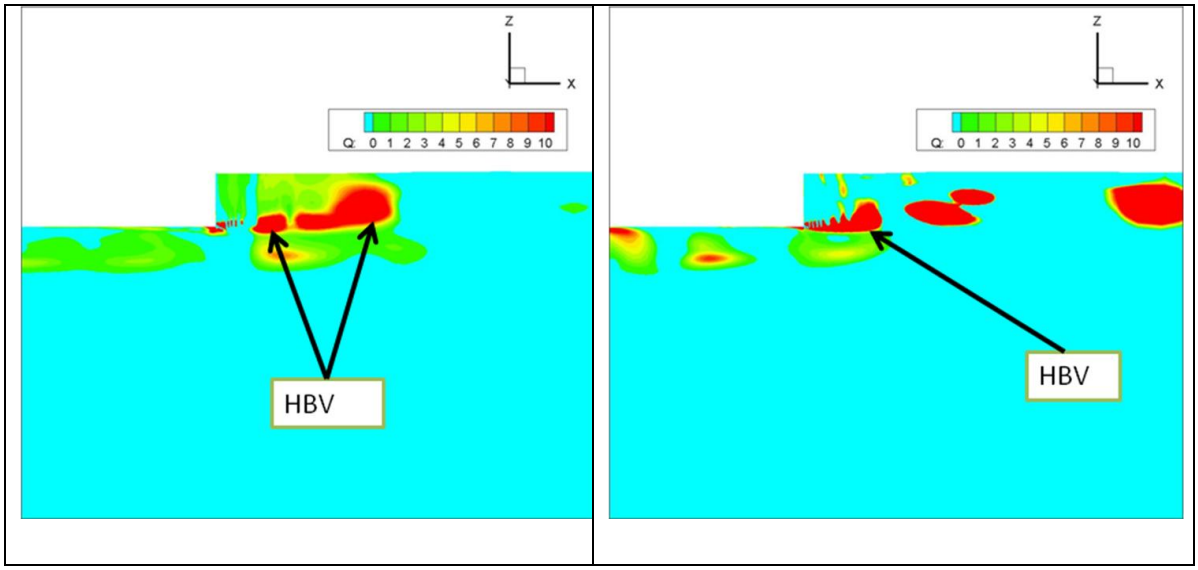

Figure 5.18 Iso-surfaces of second invariant of the velocity gradient at the center plane, y/L_{PP}=-0.067, "Bare Hull" (Left) "Stern Tunnel" (Right).

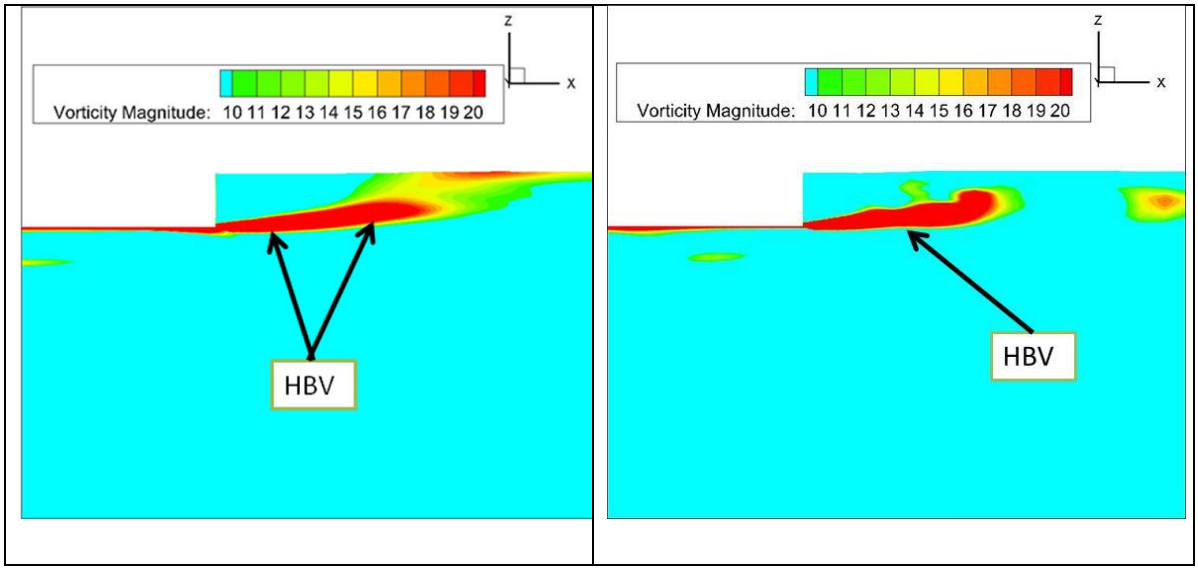

Figure 5. 19 Iso-surfaces of vorticity magnitude at the center plane, y/L_{PP}=-0.067, "Bare Hull" (Left) "Stern Tunnel" (Right).

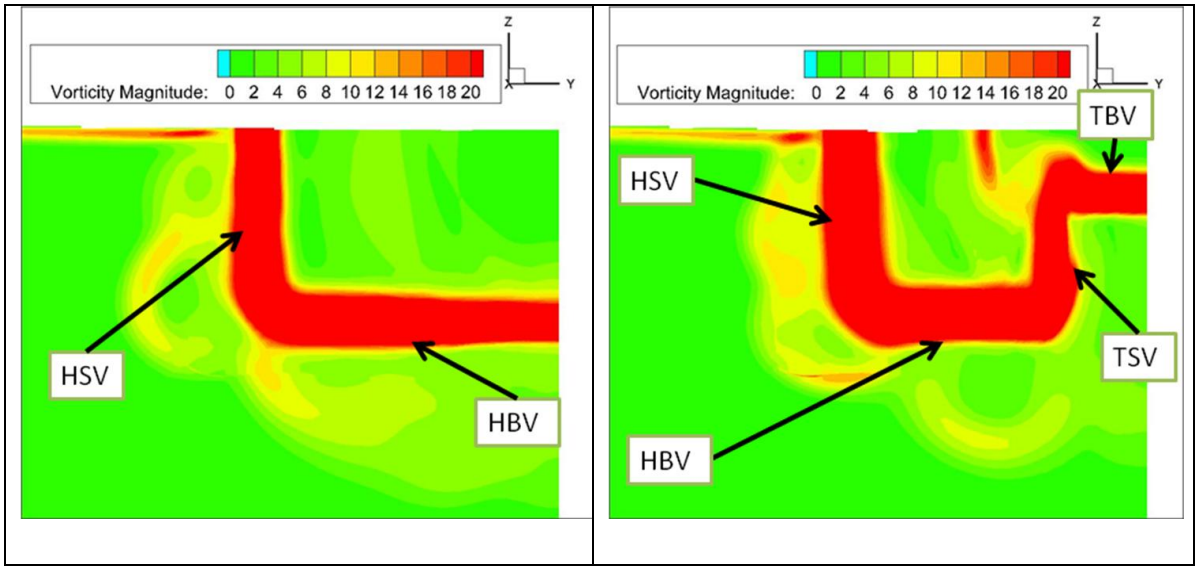

Figure 5.20 Vorticity behind the stern at x/L_{pp}=0.5533, "Bare Hull" (Left) and "Stern Tunnel" (Right).

Figure 5.20 exhibits vorticity distribution behind the stern at the section of x/L_{pp}=0.5533. These distributions clearly show HSV and HBV in "Bare Hull" and HSV, HBV, TSV and TBV in "Stern Tunnel". In both cases, it is evident that the high intensity of vorticity appears along the shape of the main transom stern and the shape of the stern tunnel. It seems the intensity of vortex becomes high after passing through the shape of the bluff bodies.

5.6 Velocity field behind the stern

Figure 5.21 and 5.22 show the velocity distributions at the section of *x*/*Lpp* = 0:5533, 5.33% *Lpp* behind the stern end. "Bare Hull" has a simple wake with the minimum velocity in the center line and near the free surface. On the other hand, the dominant wake of "Stern Tunnel" is behind the main hull part and the wake of a tunnel is higher velocity due to acceleration in a tunnel. In the cross-flow vector plots in Figure 5.22, the velocity directions are completely different between two hulls, which reflect the variation of re-circulation structures due to the stern tunnel. In "Stern Tunnel", upward velocities are observed near the center plane, which also shows the acceleration due to the stern tunnel.

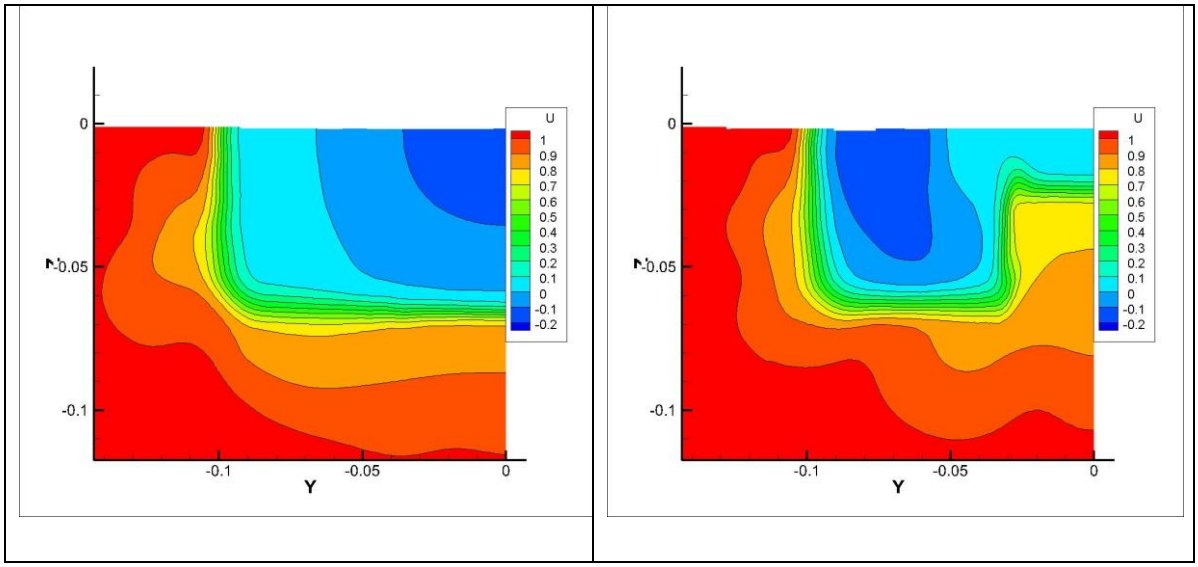

Figure 5. 21 Comparison of velocity contours *u* at the nominal wake plane at x/L_{PP}=0.5533 of ULBS, "Bare Hull" (Left) "Stern Tunnel" (Right).

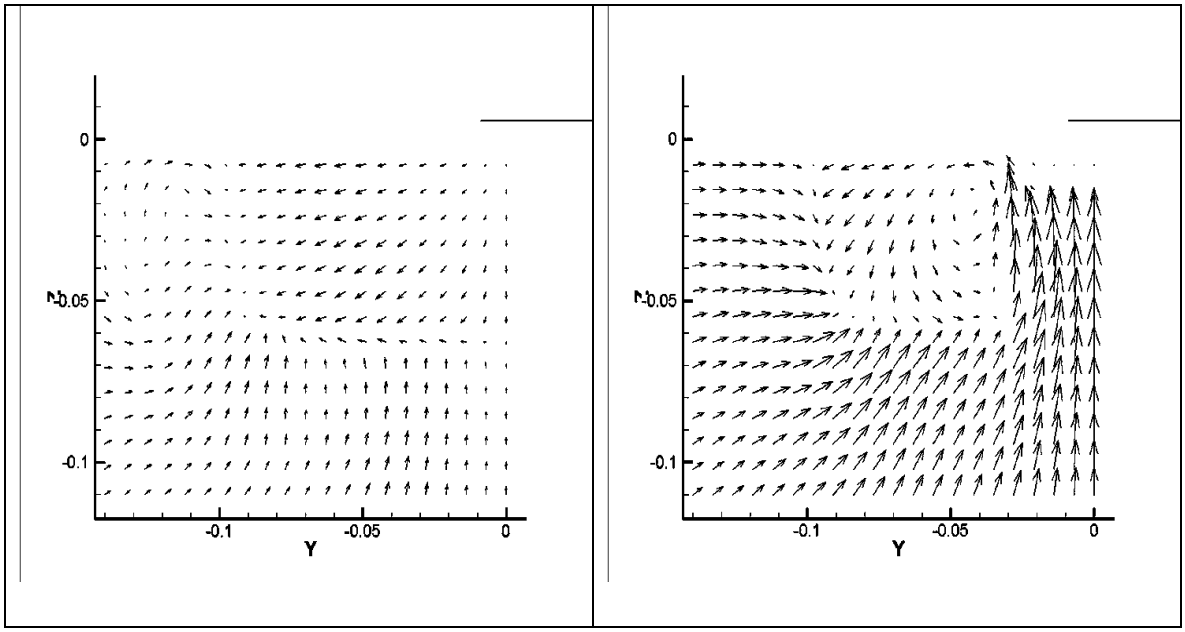

Figure 5. 22 Comparison of velocity vectors at the nominal wake plane at x/L_{PP}=0.5533 of ULBS, "Bare Hull" (Left) "Stern Tunnel" (Right).

The increasing extends of the primary vortex and the strengthening of the secondary and tertiary vortices are observed. It should be noted here that, even on this relatively coarse grid, the EARSM demonstrates its commendable performance of in predicting the strength and extent of the vortices. It is proved that, for separated/vortical flows, the EARSM

produces the best possible solution based on the RANS method. It seems that in unsteady simulation, the variations of velocity become change from time to time.

Figure 5.23 shows the comparison of computed and measured velocity profiles at z/L_{PP}=-0.033 behind the stern in "Bare Hull" cases. It is clear that the computation can capture well as in the experiment. Since ULBS is a blunt ship, longitudinal vortices behind the ship are strong and most of the estimated axial wake patterns agree well with the experiment. The patterns of computed cross flow factors are also generally in good accordance with the experiment.

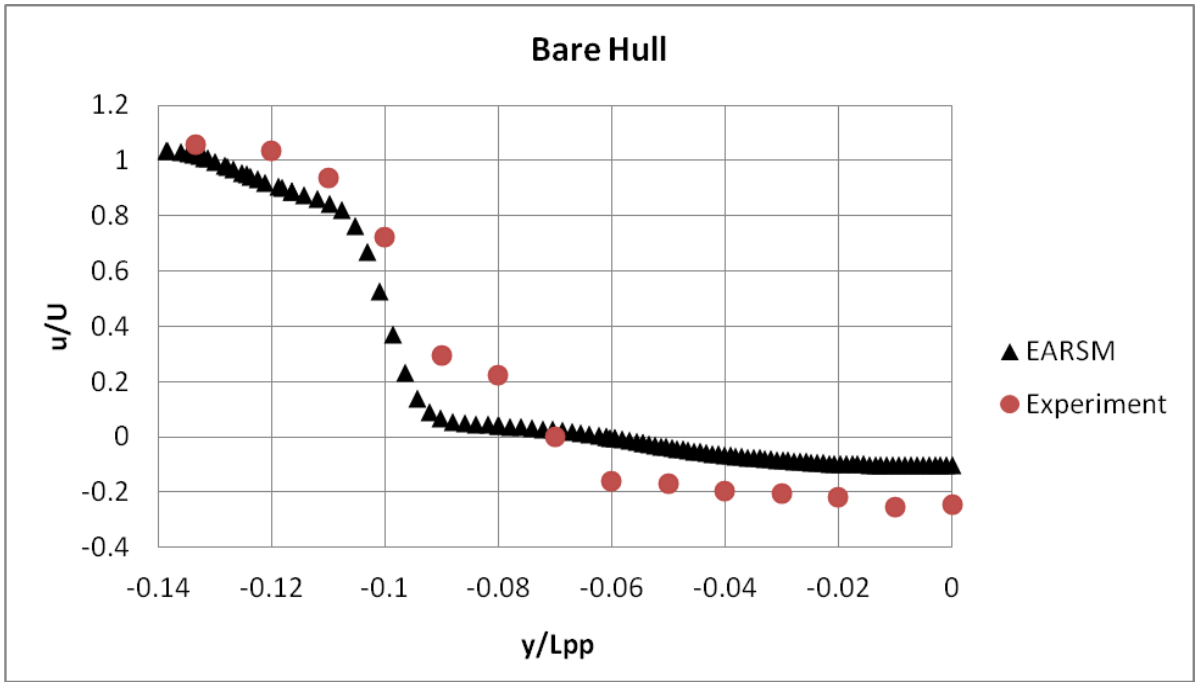

Figure 5. 23 Comparison of *u* velocity profiles between computation and measurement at (x/L_{PP}=0.553 at z/L_{PP}=-0.033) in "Bare Hull".

Figure 5.24 shows the comparison of computed and measured *u* velocity profiles at x/L_{pp}=0.5533 and z/L_{PP}=-0.033 behind the stern in "Stern Tunnel" cases. The patterns of computed cross flow factors are also generally in good accordance with the experiment. Flow at this position is strongly influenced by the stern tunnel. General trends are well reproduced by the computations, although the measured profiles exhibit slightly

narrower wake zones than computed ones for both cases. Small discrepancies may be related to modeling uncertainty associated with turbulence modeling or insufficient grid numbers.

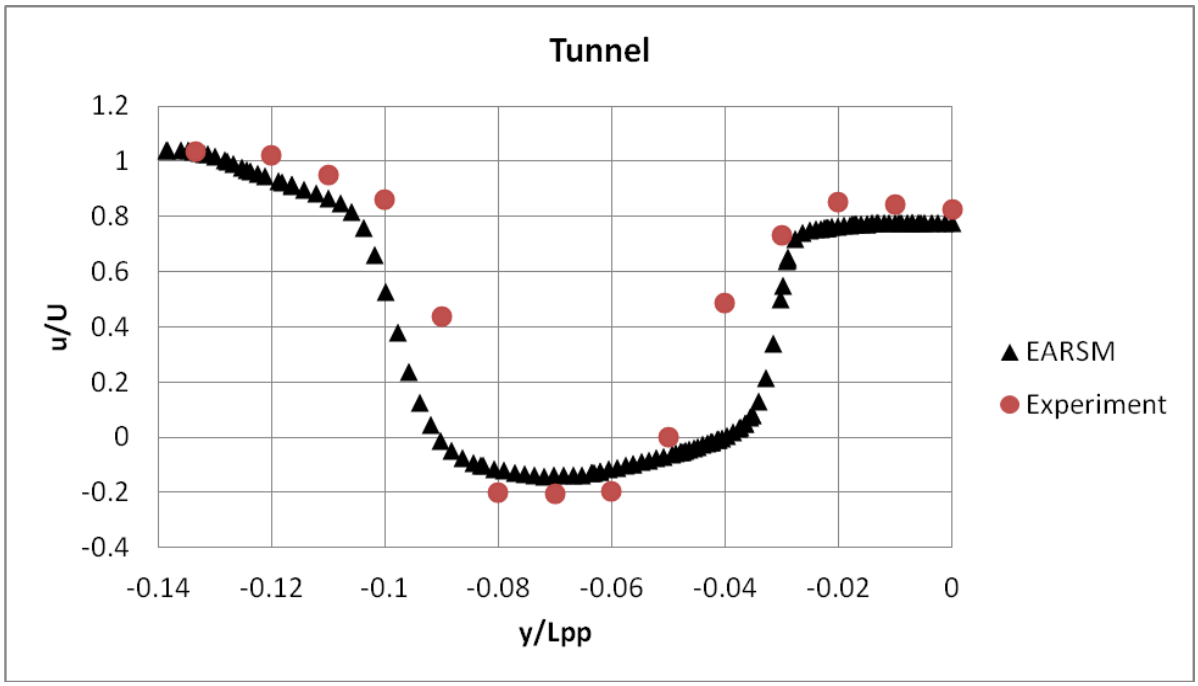

Figure 5. 24 Comparison of *u* velocity profiles between computation and measurement at (x/L_{PP}=0.553 at z/L_{PP}=-0.033) in "Stern Tunnel".

5.7 Wave fields around the hull on the free surface

The computation can also capture the free surface elevation, wave profiles and pressure distribution around the hull. Although the detail of wave fields around a hull is out of scope of the present study, Figure 5.25 displays comparison of the free-surface elevation contours around "Bare Hull" and "Stern Tunnel". The large bow waves in front of a bow are dominant and they are followed by the diverging wave system with Kelvin pattern. These features are common between two hulls. On the other hand, stern waves show different patterns. "Stern Tunnel" generates larger stern waves than "Bare Hull", since the stern tunnel accelerates the flow significantly as seen in the previous sections. Also the steep, nearly breaking, wave near the bow and stern wave pattern are clearly observed.

Figure 5.26 shows the comparison of wave profiles along the center plane and the side wall of "**B**are Hull" with that of "Stern Tunnel". The wave profiles around the bow shows similar tendencies in both cases due to the same grid of the bow block. The wave profile exhibit the peak on the front face of the bow followed by the trough at the fore corner. The trough appears again in the aft corner and stern wave is generated behind the stern. The wave profile exhibit the peak around x/L_{PP}=-0.5, which is the crest of the bow wave developing from the face of the bow followed by the trough at the fore corner. The wave profile shows the lowest trough after passing the front of the bow. After the end of the stern, the wave high becomes drop in the bare hull case, and around x/L_{PP}=-0.75, the wave high becomes higher in "Stern Tunnel" than "**B**are Hull" case. In "Stern Tunnel" case, the flow goes up along the part of the stern tunnel and the stern wave becomes higher. It is in accordance with the stern wave height in figure 5.25.

In Figure 5.27, the wave breaking is observed near the side of the bow, the computational results agree well with the experimental ones. In computing with SURF, the wave breaking in front of the bow cannot be captured as in the experiment.

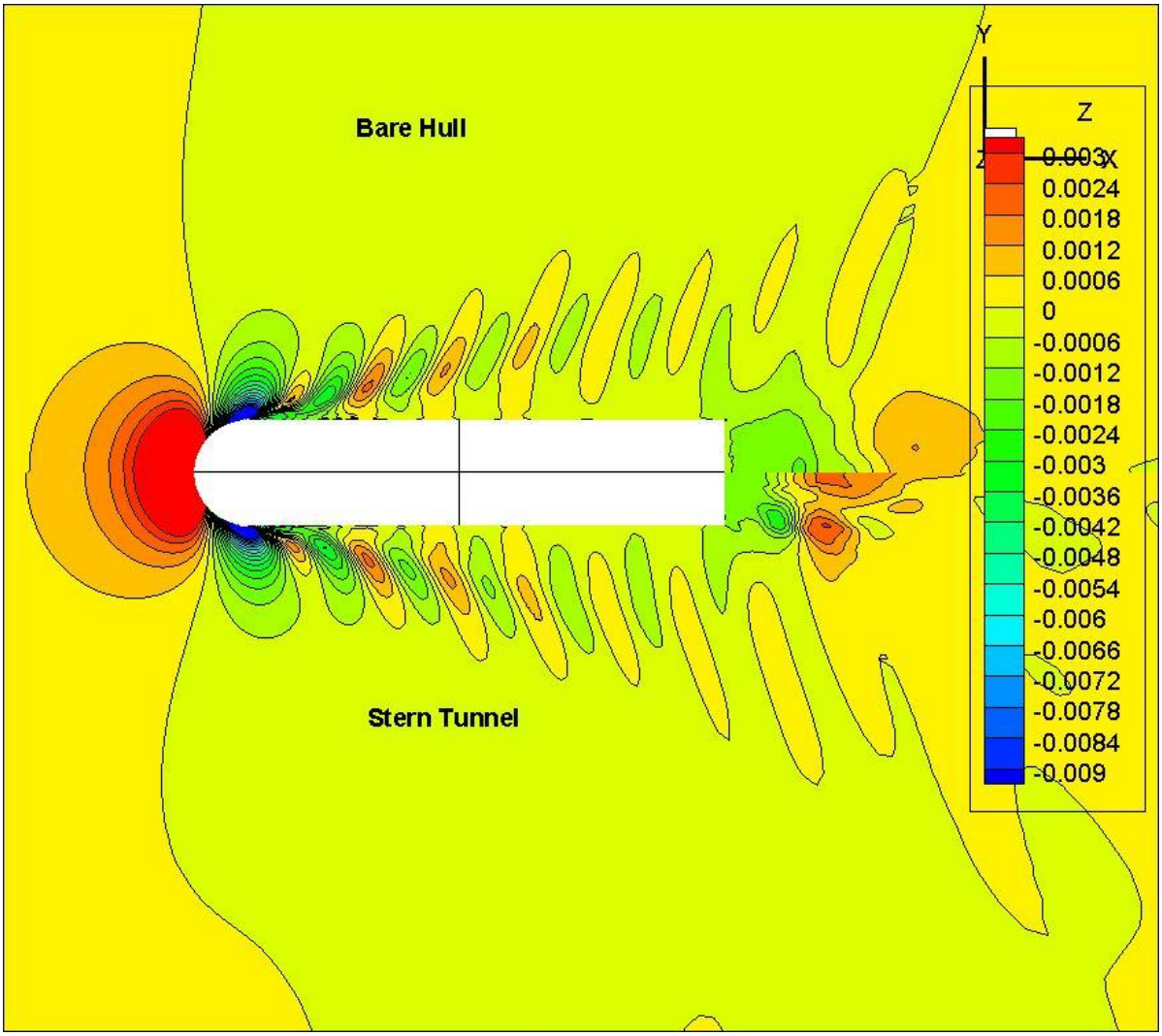

Figure 5. 25 Comparison of free-surface elevation contours around the hull of ULBS, "Bare Hull" (top) "Stern Tunnel" (bottom).

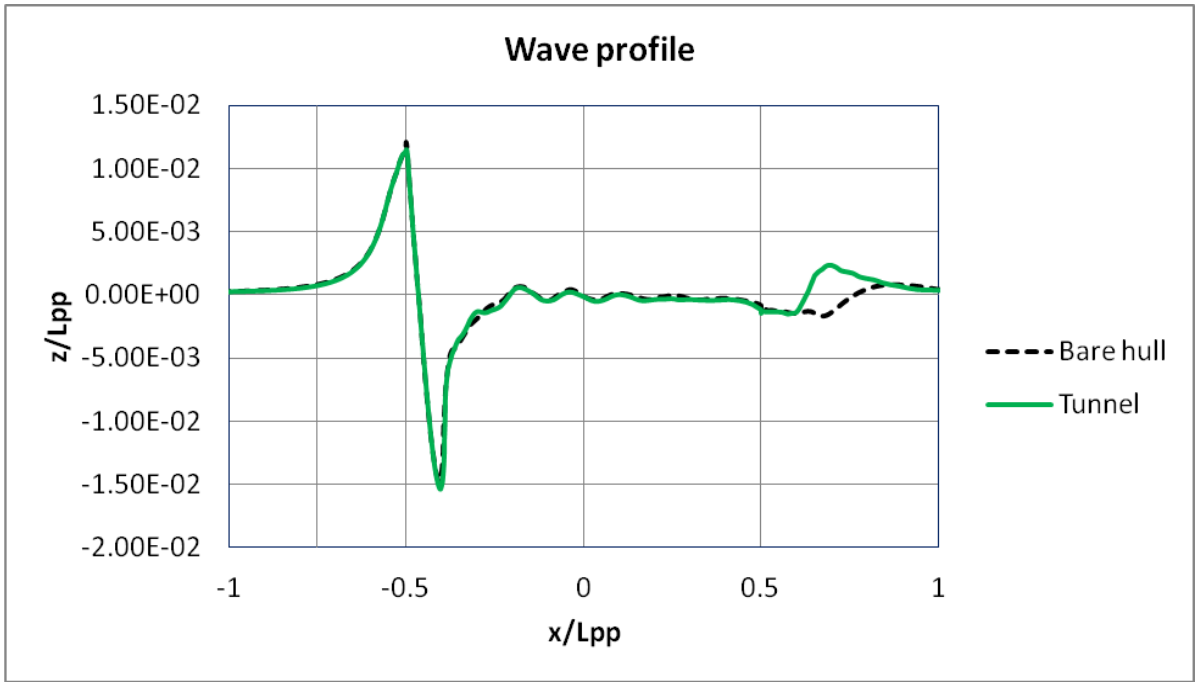

Figure 5. 26 Comparison of wave profiles between "Bare Hull" and "Stern Tunnel".

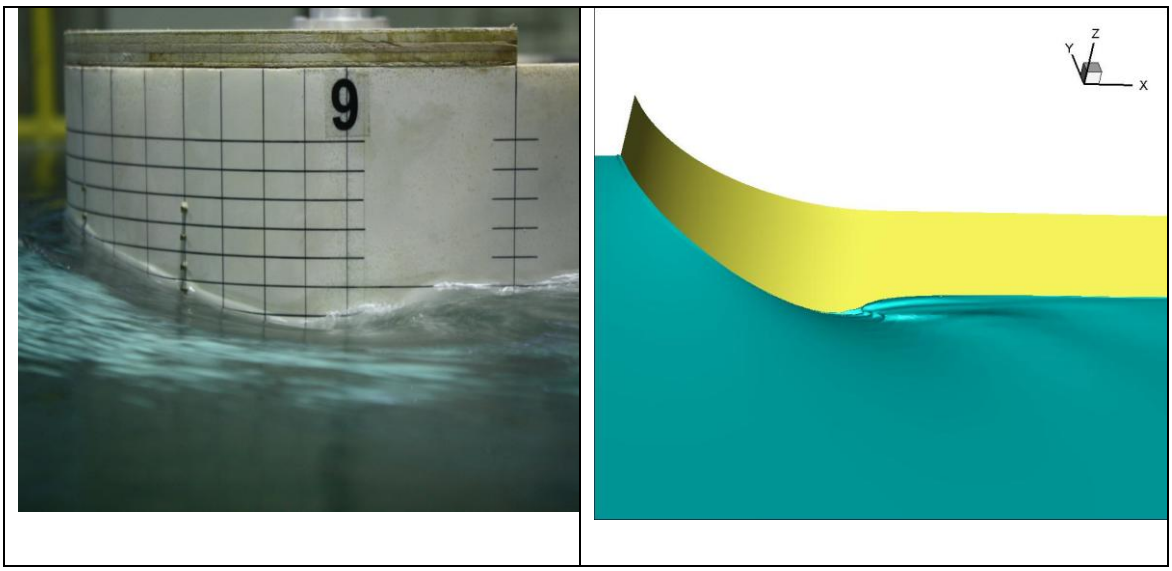

Figure 5. 27 Wave Breaking around the Bow on the Free Surface, Experiment (Left) and EARSM (Right).

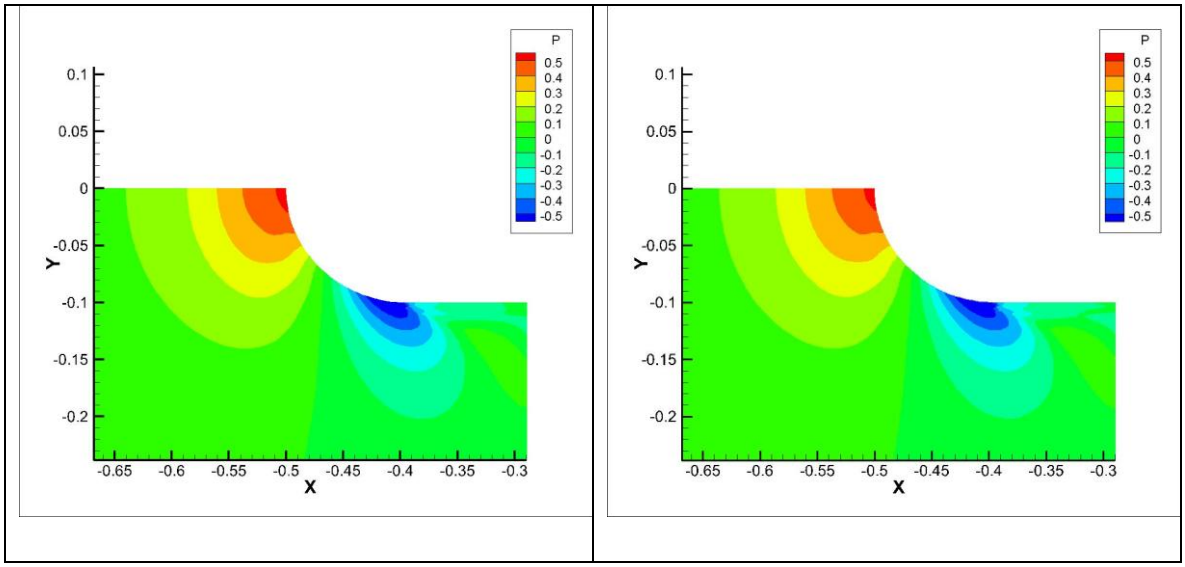

Figure 5. 28 Comparison of wave height around the bow, "Bare Hull" (Left) "Stern Tunnel" (Right).

Figure 5.28 shows comparison of pressure field around the bow on the free surface of "Bare Hull" (Left) "Stern Tunnel" (Right). With respect to the pressure field, high pressure regions near the bow due to stagnation are observed. In the side wall aft of the curve corner, pressure decreases which corresponds to the wave trough in Figure 5.26. Further downstream, pressure becomes almost constant since the side wall is flat there. The pressure distributions do not show large differences for the same block of the front part of the bow because of the same fore part.

Chapter 6

Conclusions

6.1 Conclusions for Box-shaped Ships

The free surface flows around the box shaped ships are calculated by the RANS code SURF. The verification of the results with respect to total resistance is carried out based on the series of three grid sequences, which show reasonable uncertainty levels of the present solutions. From a quantitative point of view the calculated resistance is over-predicted with 5.62% in Box A and under-predicted with 4.89 % in Box B compared with the experimental data.

The computed flow fields show separations in the corners of the boxes and behind the box and these separations interact with free surface and simulation results seem to capture these basic flow features.

The main differences between two box shapes are the variations of drafts. It seems the separations both at the side corners and behind the stern end depend on the draft of the box. The deeper the draft is, the stronger the separations. On the other hand, the separations on the bow bottom corners are not affected much by the variation of the draft.

The pressure (wave height) distributions ahead of the bow seem independent of the Froude number. The maximum and minimum wave amplitudes at the bow become larger with increasing Froude number and also with increasing draft.

The overall results seem satisfactory for our purposes to examine capabilities of CFD methods to the flow field structures around ULBS. Since the flow fields include large regions of separation and this may cause over- and under-predictions of resistance with different drafts, the effect of turbulence models should be investigated further in order to improve accuracy of the simulations. The flow simulations around actual ULBS forms will be carried out based on the knowledge learned in this study.

6.2 Conclusions for ULBS

In order to assess the capability of a CFD method currently used in practical ship flow computations with an advanced turbulence model for simulating strongly separated flows around an extremely blunt ship and to evaluate the effects of a stern tunnel, flow simulations are carried out for an extremely blunt ship with and without a stern tunnel. It is clear that the flow separations can be reduced effectively by fitting with the stern tunnel. Furthermore study to improve ULBS's design will be continued.

The verification of the computed total resistance based on three grid sequences shows reasonable uncertainty levels of the present solutions. However, the resistance decreases with a stern tunnel in the measurement is not reproduced by the simulations. Although the reason for this discrepancy is not clear, it may be due to the numerical modeling error associated with a turbulence model or due to the uncertainty of measurement. The overall flow fields look good and simulations seems to capture the basic flow features. From a quantitative point of view the calculated resistance is over-predicted with 13% in Bare Hull and with 6.12 % in Stern Tunnel.

By using the iso-surface of the second invariant of the velocity gradient tensor and the vorticity magnitude, flow structures behind the stern are analyzed. It is found that the two main vortex sheets one from the side edge of a hull and the other from the bottom edge of a hull are formulated in case of "Bare Hull". In "Stern Tunnel", on the other hand, two more vortex sheets are generated at the side wall and the bottom of a tunnel in addition to hull side and hull bottom vortices.

Also it is shown that the separation zone behind the stern is larger in "Bare Hull" than in "Stern Tunnel" by the examination of velocity fields and streamlines. Computed velocity profiles behind the hull reproduce the general trend which is similar to that of the measured data both in "Bare Hull" and "Stern Tunnel" cases. It appears that the performance of the turbulence models is not sufficient for quantitative comparisons with the measurement, although the uncertainty of the velocity measurement must be examined further.

Though further study of turbulence modeling effects is desirable for the improvement of numerical accuracy, the overall results in general seem satisfactory for our purposes of

examining capabilities of CFD methods for analysis of flow structures with and without a stern tunnel. The overall results show the difference of flow structures with and without a stern tunnel well.

Another future scope is a hull form optimization of ULBS. The large areas of flow separation are found in the bow bottom and the stern tunnel shape seems not optimal. The optimization of these parts as well as the use of other flow control devices is needed for better design of ULBS. Experimental and simulation of ULBS with bulbous bow & other appendages and optimization of ULBS hull form will be carried out.

Wave breaking is observed near the side of the bow, the computational results agree well with the experimental ones. However, in SURF computation, the wave breaking in front of the bow cannot be captured as in the experiment. The wave profiles around the hull are captured well. It is obvious that the appropriate Kelvin wave patterns are well reproduced and the near-hull features of the free surface are captured well.

At the vertical centre plane, a series of three vortexes occurs near the bottom of the bow. And low velocity regions are observed in accordance with the vortexes, and then the vortexes extend further downstream.

The computed flow fields show separations in the corner of the bow and behind the stern. These separations interact with free surface and simulation results seem to capture the basic flow features.

The region of lower velocity and intensity of vortex behind the stern end is smaller in the stern tunnel hull case than in the bare hull case, and in accordance with the vortex. The flow separation comes from the transom stern in bare hull case and it comes from the stern tunnel part in stern tunnel case. It is obvious that the separation becomes weaker in the stern tunnel cases than in the bare hull cases. It seems the separation near the stern end depends on the shape of the stern, and the presence of the stern tunnel can reduce the flow separations.

On the free surface, the streamlines seem still. The velocity becomes higher nearer the curve end of the bow. And the velocity becomes drop after passing the curve end of the bow.

The overall results seem satisfactory for our purposes to examine capabilities of CFD methods to the flow field structures around ULBS.

The flow simulations around actual ULBS forms will be carried out based on the knowledge learned in this study.

Also the velocity distributions, u, behind the stern can be captured as in the experiment. General trends are well reproduced by the computations, although the measured profiles exhibit slightly narrower wake zones than computed ones for both cases. Small discrepancies may be related to modeling uncertainty associated with turbulence modeling or insufficient grid numbers. But it seems EARSM model can capture correctly the flow phenomenology even in the complex flow configurations. It seems the simulation can be captured qualitatively.

Further experiment and simulation of ULBS with bulbous bow and other appendages will be studied. Optimization of ULBS hull form will also be studied.

Bibliography

1) CASE 9.4 Flow around a simplified car body (Armed body), 10th joint ERCOFTAC(SIG-15)-IAHR-QNET/CFD Workshop on Refined Turbulence Modeling,

   http://www.ercoftac.org/fileadmin/user_upload/bigfiles/sig15/database/9.4/ws_10.html, 2002.

2) Azcuera, R., Muzaferija, S., Peric, M.: Computation of breaking bow waves for a very full hull ship, Proc. 7th Int.Conf. Numer. Ship Hydrodynamics, 1999.

3) Hino, T.: Numerical Simulations of Breaking Waves around an Advancing Ship by an Unstructured NS Solver, Proceeding of 25th Symposium on Naval Hydrodynamics, 2004.

4) Nang Tin Tin Htwe and Hino, T.: Free Surface Flow Computations of Box-Shaped Ships by an Unstructured Navier-Stokes Solver: The 25th Computational Fluid Dynamics Symposium, Osaka, 2011.

5) Hino T.: Navier-Stokes Computations of Ship Flows on Unstructured Grids, Proceeding of the 22nd Symposium on Naval Hydrodynamics, 1998.

6) Hino, T.: A 3D Unstructured Grid Method for Incompressible Viscous Flows, Journal of the Society Naval Architect Japan, Vol.182, pp.9-15,1977.

7) Hino, T.: An Interface Capturing Method for Free Surface Flow Computations on Unstructured Grids, J. of the Society Naval Architect Japan, Vol.186, pp.177 – 183, 1999.

8) Roe, P.L.: Characteristic-Based Schemes for the Euler Equations, Anniversary Rev. Fluid Mechanics, Vol.18, pp.337 – 365, 1986.

9) Gatski, T.B., “Turbulent Flows: Model Equations and Solution Methodology,” Handbook of Computational Fluid Mechanics, edited by R. Peyret, Academic Press, London, 1996, pp.339-415.

10) Peng, D. et al.: A PDE-Based Fast Localized Level Set Method, J. Computational Physics, Vol.155, pp.410-438, 1999.

11) ITTC Recommended Procedures and Guidelines, "Uncertainty Analysis in CFD Verification and Validation Methodology and Procedures", 7.5-03-01-01.

12) ITTC Recommended Procedures and Guidelines, "CFD, Resistance and Flow Uncertainty Analysis in CFD Examples for Resistance and Flow," 7.5-0.3-02-01.

13) Deng, G.B, Guilmineau, E., Queuty, P. and Visonneau, M.: Ship flow simulations with the ISIS CFD code, CFD Workshop Tokyo, 2005.

14) Haller G.: An Objective Definition of a Vortex, Journal of Fluid Mechanics, Vol. 525, pp. 1-26, 2005.

15) J. Wackers.B, H.C. Raven, A.Vander Ploeg, A.R Staker, G.B.Deng, P.Queutey, M.Visonneau, T. Hino, K. Ohashi.: Free- Surface Viscous Flow Solution Method for Ship Hydrodynamics.Arch Computational Methods, pp.1-41, 2011.

16) Ohashi, S. and Ikebuchi, Y.: Resistance Test on Floating Boxes, Papers of the Shipbuilding Research Center of Japan, Vol.1, 1977.

17) Spalart, P.R. et al.: A One-Equation Turbulence Model for Aerodynamic Flows, La Recherche A´erospatiale, No.1, pp.5 – 21, 1994.

18) David C. Wilcox Turbulence Modeling for CFD, July, 1993.

19) N. HIRATA and T. HINO.: A comparative Study of Zero - and One - Equation Turbulence Models for Ship flows, J. Kansai Soc. N.A., Japan, No.234, pp. 17 – 24, September 2000.

20) Rumsey, C. L., Gatski, T. B.: Recent turbulence model advances applied to multi-element airfoil computations, Journal of aircraft, Vol. 38, no. 5, 2001.

21) Jongen, T., and Gatski, T. B.: A Unified Analysis of Planar Homogeneous Turbulence Using Single-Point Closure Equations, Journal of Fluid Mechanics, Vol. 399, pp. 117-150, 1999.

22) Wilcox, D. W.: *Turbulence Modeling for CFD*, 2nd ed., DCW Industries, La Canada, CA, 1998.

23) Menter, F. R.: Two-Equation Eddy-Viscosity Turbulence Model for Engineering Application, AIAA Journal, Vol.32, No.8, pp.1598- 1605, 1994.

Comments

Question (1):

Why is the resistance decreases with a stern tunnel in the measurement not reproduced by the simulations?

Answer (1):

The resistance decreases with a stern tunnel in the measurement is not reproduced by the simulations. But the verification of the computed total resistance based on three grid sequences show reasonable uncertainty levels of the present solutions. The overall flow fields look good and simulations seems to capture the basic flow features.

A possible reason for this opposite prediction of resistance trend is numerical modeling errors of the current turbulence models for large scale separated flows or insufficient grid numbers. Further investigations are required both in simulations and measurements to clarify the reasons of this discrepancy.

The ship model is only 1.5 meters and is simulating in the small oscillating water channel. The measured flow velocity is also very low. On the other hand, the accuracy of the resistance measurement must be examined as well.

Question (2):

What is the meaning of order of accuracy *p*?

Answer (2):

Order of accuracy is the rate of decrease of discretization error with mesh refinement. The *observed order of accuracy* is the measure that is used to assess the confidence in a discretization error estimate. When the observed order of accuracy matches the formal order, then one can have high confidence that the error estimate is accurate and therefore use the error estimate to correct the solution. However, the much more common case is when the formal order does not match the observed order. In this case, the error estimate is much less reliable and should generally be converted into a numerical uncertainty. While the difference between the discrete solution and the (unknown) exact solution to the mathematical model is still truly an error, the lack of knowledge of the true value of this error will be forced to represent it as an epistemic uncertainty. Epistemic uncertainties are distinct from aleatory (or

random) uncertainties in that they are due to a lack of knowledge. They can be reduced by providing more information, in this case, additional computations on more refined meshes.

When the exact solution is not known, three numerical solutions on systematically-refined meshes are required to calculate the observed order of accuracy. Consider a p^{th}-order accurate scheme with numerical solutions on a fine mesh (h_1), a medium mesh (h_2), and a coarse mesh (h_3). For the case of a constant grid refinement factor, i.e.,

$$r = \frac{h_2}{h_1} = \frac{h_3}{h_2} > 1$$

$$h_1 = h, h_2 = rh, h_3 = r^2 h$$

Using the discretization error expansion, we can now write for the three discrete solutions:

$$f_1 = f + g_p h^p + g_{p+1} h^{p+1} + O\left(h^{p+2}\right)$$

$$f_2 = f + g_p (rh)^p + g_{p+1} (rh)^{p+1} + O\left(h^{p+2}\right)$$

$$f_3 = f + g_p \left(r^2 h\right)^p + g_{p+1} \left(r^2 h\right)^{p+1} + O\left(h^{p+2}\right)$$

Neglecting terms of order h_{p+1} and higher allows us to recast these three equations in terms of a locally-observed order of accuracy $\hat{p}$:

$$f_1 = f + g_p h^{\hat{p}}$$

$$f_2 = f + g_p (rh)^{\hat{p}}$$

$$f_3 = f + g_p \left(r^2 h\right)^{\hat{p}}$$

which will only match the formal order of accuracy if the higher order terms are indeed small. Subtracting f_2 from f_3 and f_1 from f_2 yields:

$$f_3 - f_2 = g_p \left(r^2 h\right)^{\hat{p}} - g_p (rh)^{\hat{p}} = g_p r^{\hat{p}} h^{\hat{p}} \left(r^{\hat{p}} - 1\right)$$

$$f_2 - f_1 = g_p \left(r\ h\right)^{\hat{p}} - g_p h^{\hat{p}} = g_p\ h^{\hat{p}} \left(r^{\hat{p}} - 1\right)$$

$$\frac{f_3 - f_2}{f_2 - f_1} = r^{\hat{p}}$$

Taking the natural log of both sides and solving for the observed order of accuracy $\hat{p}$ gives:

$$\hat{p} = \frac{\ln\left(\frac{f_3 - f_2}{f_2 - f_1}\right)}{\ln(r)}$$

Correction factor

$$C = \frac{r^p - 1}{r^{pth} - 1}$$

where p^{th} is "theoretical " order of accuracy of the applied numerical method. If the correction factor is close to unity, the solutions are close to the asymptotic range. p^{th} is second order accuracy and p here is 5^{th} order accuracy. Because the higher order terms are neglected, and the error become large. To reduce error, very fine grids are essential to generate. In this case the grid is about five million and it seems fine. But the error is still large.